



저작자표시-비영리-변경금지 2.0 대한민국

이용자는 아래의 조건을 따르는 경우에 한하여 자유롭게

- 이 저작물을 복제, 배포, 전송, 전시, 공연 및 방송할 수 있습니다.

다음과 같은 조건을 따라야 합니다:



저작자표시. 귀하는 원저작자를 표시하여야 합니다.



비영리. 귀하는 이 저작물을 영리 목적으로 이용할 수 없습니다.



변경금지. 귀하는 이 저작물을 개작, 변형 또는 가공할 수 없습니다.

- 귀하는, 이 저작물의 재이용이나 배포의 경우, 이 저작물에 적용된 이용허락조건을 명확하게 나타내어야 합니다.
- 저작권자로부터 별도의 허가를 받으면 이러한 조건들은 적용되지 않습니다.

저작권법에 따른 이용자의 권리는 위의 내용에 의하여 영향을 받지 않습니다.

이것은 [이용허락규약\(Legal Code\)](#)을 이해하기 쉽게 요약한 것입니다.

[Disclaimer](#)

Doctoral Thesis

Synthesis and Mechanical Characterization of
Metallic Glasses with High Elastic Deformation for
Stretchable Encapsulation Films

Sun-Young Park

Department of Materials Science and Engineering

Graduate School of UNIST

2019

Synthesis and Mechanical Characterization of
Metallic Glasses with High Elastic Deformation
for Stretchable Encapsulation Films

Sun-Young Park

Department of Materials Science and Engineering

Graduate School of UNIST

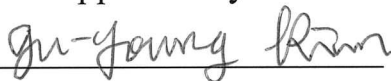
Synthesis and Mechanical Characterization of
Metallic Glasses with High Elastic Deformation
for Stretchable Encapsulation Films

A thesis/dissertation
submitted to the Graduate School of UNIST
in partial fulfillment of the
requirements for the degree of
Doctor of Philosophy

Sun-Young Park

6. 10. 2019

Approved by



Advisor

Ju-Young Kim


Synthesis and Mechanical Characterization of
Metallic Glasses with High Elastic Deformation
for Stretchable Encapsulation Films

Sun-Young Park

This certifies that the thesis/dissertation of Sun-Young Park is
approved.

6/10/2019

signature



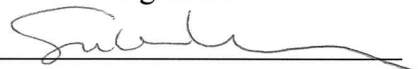
Advisor: Prof. Ju-Young Kim

signature



Prof. Han Gi Chae

signature



Prof. Sukbin Lee

signature



Prof. Eun-chae Jeon

signature



Prof. Young-Cheon Kim

Abstract

Metallic glasses have been researched extensively due to their remarkable properties such as excellent corrosion resistance, large elastic limit and strength, unique soft magnetic properties, wear resistance etc. One of the most attractive aspect of metallic glasses is impressive suite of mechanical properties. Compared to crystalline material with similar composition, metallic glasses exhibit significantly high elastic limit and tensile strength. On the other hand, they have a lack of tensile ductility that results in sudden and catastrophic failure due to intrinsic properties of atomic arrangement, disordered structure. Considerable work has been aimed at improving the tensile ductility of metallic glasses, and the development of glass-matrix composites with high toughness and tensile ductility is being explored. Two basic techniques are employed to attain high tensile ductility: introducing a softer secondary phase in the metallic glass matrix to induce generation of local shear banding around the secondary phase and reducing its external dimensions to suppress a propagation of shear bands or occur homogeneous flow instead, leading to enhanced strength and ductility. Since there are limited structural applications for monolithic metallic glass with dimensions of the order of 100 nm, nanolaminates with alternating layers of metallic glass (with dimensions of 100 nm or less) and another material have been suggested as a more practical material. Metallic glass-based nanolaminates with proper interfacial material and optimum layer thickness can exhibit improved strength and ductility by utilizing size-dependent homogeneous flow of metallic glass. In this study, mechanical behavior of nanolaminate with metallic glass and graphene is investigated. Nanolaminate with alternating layers of metallic glass and graphene is fabricated by repeating deposition of metallic glass by sputtering and transfer of chemical vapor deposition-grown graphene. In situ micro-tensile tests reveal that the addition of a very small fraction of graphene in the nanolaminate improve the elastic modulus and yield strength of the nanolaminate, comparing with those of the monolithic metallic glass. The nanolaminate also shows enhanced tensile ductility by homogeneous flow in the metallic glass layers. Using mechanical properties of metallic glass, metallic glass film is investigated for stretchable encapsulation material. Encapsulation is necessary to protect devices vulnerable to

moisture and oxygen and as stretchable and wearable devices are developed, stretchability is also required in encapsulation materials. Amorphous structure of metallic glass material is advantageous in encapsulation film since diffusion path of moisture or oxygen vapor is increased comparing to crystalline or organic materials with grain boundary or large size of defects. The ternary metallic glass thin film with high thermal stability is fabricated by co-sputtering process. Electrical Ca test is performed to evaluated diffusion barrier characteristic and reveal metallic glass in the system of Cu-Zr-Ti has water vapor transmission rate of 10^{-3} order. Stretchability of ternary metallic glass thin film is evaluated as 4 % through in situ tensile testing and cyclic stretching testing, showing feasibility for stretchable encapsulation material.

Contents

Abstract	i
List of Figures	v
List of Tables	ix
Chapter 1. Introduction	1
Chapter 2. Theoretical Background	3
2.1 Amorphous metallic alloy	3
2.1.1 Mechanical behavior of metallic glass	3
2.1.2 Multilayer of metallic glass	15
2.2 Encapsulation for stretchable devices	18
2.2.1 Thin film encapsulation	18
2.2.2 Water vapor transmission rate (WVTR)	27
Chapter 3. Enhanced mechanical properties of nanolaminate with metallic glass and graphene	32
3.1 Materials	32
3.1.1 Fabrication of metallic glass thin film by sputtering	32
3.1.2 Graphene by chemical vapor deposition (CVD)	33
3.1.3 Synthesis of nanolaminate with metallic glass and graphene	34
3.2 Mechanical deformation by graphene coating	38
3.3 Tensile behavior of nanolaminate	46
3.3.1 Tensile test results of monolithic metallic glass and nanolaminate	46
3.3.2 Homogeneous deformation flow of metallic glass in nanolaminate	50
Chapter 4. Metallic glass thin film for stretchable encapsulation	55
4.1 Materials	55
4.1.1 Synthesis of smooth metallic glass thin film by co-sputtering	55
4.1.2 Fabrication of high-thermally stable metallic glass	57
4.1.3 Edge sealing deposited by sputtering process	58

4.2 Diffusion barrier characteristics of metallic glass thin film	59
4.2.1 Water vapor transmission rate of metallic glass	59
4.2.2 Oxidation mechanism of metallic glass	63
4.3 Mechanical deformation of metallic glass thin film	72
4.4 Cyclic stretching behavior of thin film	77
Chapter 5. Conclusion	81
Reference	82

List of figures

Figure 1. Amorphous metallic alloys showing higher strength than crystalline metal alloys with elasticity of polymers.

Figure 2. Model for shear transformation zones in a Ni-Ti metallic glass (a) distribution of STZs size (b) distribution of energy barrier (c) typical STZ configuration before and after shear transformation.

Figure 3. (a) The snapshot schematic for the evolution of the shear band into four different stages following the elastic deformation. (b) Stress-strain curve of metallic glass corresponding to snapshots of shear band formation. (c) Plot of the elapsed time according to kinetic Monte Carlo steps involved in shear band formation.

Figure 4. (a) Small-volume metallic glass samples for in situ tensile straining experiment in the TEM. Viewing directions for the first (b) and second (c) steps of FIB. (d) Images of TEM frames during the in situ TEM tensile testing.

Figure 5. Monotomic nanotension results for the 100 nm-diameter sample. (a) SEM images captured from a movie during an in situ tension testing. (b) The engineering and (c) true stress-strain curves of tension test. True stress-strain after necking were obtained by directly measuring the diameter.

Figure 6. The equilibrium phase diagram of Cu-Zr system. The shading of the composition range of 20 to 70% shows strong glass forming ability of Cu-Zr system.

Figure 7. Relationship between compressive residual stress and film thickness of Zr-based thin film metallic glasses deposited by sputtering.

Figure 8. (a) SEM image of multilayered thin film pillar with metallic glass and Zr layer on Si (001) after compression test up to 25% strain and (b) the recorded engineering stress-strain curve.

Figure 9. (a) UTS profile of amorphous layer as function of thickness of amorphous layer. (b) Model developed for UTS of nanolaminates fitting to experimental data.

Figure 10. Schematic diagrams for encapsulation techniques; (a) conventional method using glass lid, (b) laminated barrier layer lid, and (c) monolithic thin film coating.

Figure 11. Transmission electron microscopic images of cross-sectional Al_2O_3 - ZrO_2 hybrid film grown by ALD process at (a) low resolution and (b) high resolution.

Figure 12. Encapsulation performance of $\text{Al}_2\text{O}_3/\text{ZrO}_2$ nanolaminate with different number of dyads and thickness of each layer. (a) Ca-test results of three different nanolaminate structures with the same number of interfaces. (b) Ca-test results of pure Al_2O_3 and ZrO_2 , and eight different nanolaminate structure dependent on thickness of each layer.

Figure 13. (a) Schematic diagram of the hybrid nano-stratified moisture barrier with 2.5 dyads stack. Cross-sectional TEM image of (b) total stack structure and (c) magnified view of 1 dyad with nano-stratified stack and nanocomposite layer. Electrical Ca test results of (d) single inorganic single layers and nano-stratified barrier and (e) hybrid nano-stratified barrier structure depending on the number of dyads.

Figure 14. (a) J-V curves and (b) L-V curves of thin film encapsulated device using hybrid nano-stratified barrier after fabrication for a 30-day period, and (c) optical images with time duration of un-encapsulated and encapsulated cell under severe conditions.

Figure 15. (a) The flexible lamination encapsulation process. (b) Lifetime measurement of encapsulated OLEDs. (c) Bending stability measurements of ITO-coated PET substrate and Flex Lami-capsulated OLED fabricated on ITO-coated PET substrate according to bending radius. (d) Demonstration for large-area OLEDs encapsulated with Flex Lami-capsulation.

Figure 16. Diagram of the required water vapor transmission rate and oxygen transmission rate for various electronic devices.

Figure 17. Normalized conductance versus time for a Ca pad sealed with an Al_2O_3 layer of 130 nm thickness grown by ALD process at 80°C.

Figure 18. (a) SEM image of cross section of metallic glass deposited on Si substrate. (b) TEM image of $\text{Cu}_{50}\text{Zr}_{50}$ metallic glass showing amorphous structure.

Figure 19. Schematic of fabrication of nanolaminate with alternating layers of $\text{Cu}_{50}\text{Zr}_{50}$ metallic glass and graphene and sample for in situ SEM micro-tensile testing.

Figure 20. (a) Raman spectra showing typical features of monolayer graphene. (b) The morphology of graphene transferred on $\text{Cu}_{50}\text{Zr}_{50}$ metallic glass.

Figure 21. (a) SEM image of freestanding film by etched Si substrate using XeF_2 gas. (b) Dog-bone shaped tensile sample fabricated by FIB milling. (c) P-to-P device transferred FIB-patterned tensile sample for in situ tensile testing. Inset is magnified images of tensile sample.

Figure 22. (a) Typical Raman spectra of CVD-grown graphene. (b) Typical EBSD and (c) AFM images of graphene-coated Cu. In yellow surfaces indicated as black arrow, nanoindentations were carried out.

Figure 23. (a) Typical and (b) averaged nanoindentation force-depth curves of graphene-coated Cu and graphene-removed Cu. (c) Typical nanoindentation force-indentation depth curves magnified for initial contact area. Dotted lines are Hertzian equations fitted to loading curves. (d) Histograms of indentation depth at first pop-in event of graphene-coated and graphene-removed Cu.

Figure 24. (a) Averaged elastic modulus and (b) hardness of graphene-coated and graphene-removed Cu measured by the Oliver-Pharr method.

Figure 25. (a) AFM images of residual indentation marks for graphene-removed Cu and graphene-coated Cu. (b) Distributions of von Mises stress in the loaded state analyzed by FEA. Insets show pile-up heights in the loaded state.

Figure 26. Typical tensile curves of 360 nm-thick monolithic metallic glass and nanolaminate with 60 nm-thick metallic glass and graphene. (a) The true stress-strain curves of monolithic metallic glass and nanolaminate. SEM images during tensile testing of (b) 360-thick monolithic metallic glass and (c) nanolaminate.

Figure 27. Interrupted in-situ micro-tensile testing for nanolaminate with alternating layers of 60 nm-thick metallic glass and graphene. (a) Yield strength in first, second, and third loading increases gradually, supporting that 60 nm-thick metallic glass layers are strain-hardened by homogeneous flow. (b) Homogeneous deformation is observed during interrupted micro-tensile testing.

Figure 28. Deformation map of metallic glass in nanolaminate at reduced size.

Figure 29. AFM images and profiles of binary metallic glass deposited by sputtering depending on sputtering conditions.

Figure 30. AFM images and profiles showing smooth surface morphology of metallic glass thin films deposited using optimized sputtering condition.

Figure 31. Sample preparation schematic and condition for WVTR measurements.

Figure 32. WVTR measurement results of Cu, binary and ternary metallic glass film under environment of environment of 90% relative humidity at 30°C.

Figure 33. The optical images of as deposited and oxidized for 2 days of binary metallic glass thin films, $\text{Cu}_{60}\text{Zr}_{40}$, $\text{Cu}_{40}\text{Zr}_{60}$, are under an environment of 85% relative humidity at 85°C.

Figure 34. Plot of \ln WVTR versus temperature for water vapor permeation through ternary metallic glass thin film structure.

Figure 35. Surface of nanocrystalline Cu, binary and ternary metallic glass films for as-deposited and after oxidation under an environment of 85% relative humidity at 85°C.

Figure 36. X-ray diffraction pattern of oxidized binary and ternary metallic glass thin films under an environment of 85% relative humidity at 85°C for 1000 hours.

Figure 37. XPS element-depth profiles of oxidized metallic glass films: (a) binary metallic glass $\text{Cu}_{39}\text{Zr}_{61}$ and (b) ternary metallic glass $\text{Cu}_{31}\text{Zr}_{61}\text{Ti}_8$.

Figure 38. XPS spectra of $\text{Cu}2p^3$ level for different depths of oxidized binary metallic glass film.

Figure 39. XPS spectra of Zr3d level for different depths of (a) oxidized binary metallic glass film and (b) oxidized ternary metallic glass film under environment of 85% relative humidity at 85°C.

Figure 40. WVTR measurement results of as-deposited and oxidized ternary metallic glass thin film under environment of 85% relative humidity at 85°C.

Figure 41. Schematic of sample preparation for tensile testing.

Figure 42. Typical stress-strain curves of nanocrystalline copper film, binary metallic glass and ternary metallic glass films for in-situ tensile testing.

Figure 43. SEM images of nanocrystalline Cu during in situ tensile testing showing elastic deformation followed by necking and fracture with shear-off around 3% strain.

Figure 44. SEM images of (a) binary metallic glass and (c) ternary metallic glass tensile samples during in situ tensile testing showing elastic deformation followed by fracture with single shear banding.

Figure 45. SEM and AFM images of wrinkled metallic glass thin film on PDMS substrate. Surface profile of wrinkle structure for measurement of amplitude and wavelength.

Figure 46. SEM images of nanocrystalline Cu, binary and ternary metallic glass thin films for as-deposited and after cyclic stretching 1000 cycles at 4% strain.

List of Tables

Table 1. Sputtering conditions and atomic ratio for binary and ternary metallic glass thin film.

Table 2. Gibbs energies of formation of Cu and Zr corresponding oxides.

Table 3. Thermal properties of various metallic glass in Cu-Zr-Al ternary system.

Chapter 1. Introduction

Amorphous metallic alloys, alternatively known as metallic glasses (MGs) was discovered by Pol Duwez at Caltech [1][2], the technique to fabricate MGs using undercooling a molten metal. Metallic glass is a metallic material with disordered atomic structure like glass material. They have been researched extensively since the 1960s, due to their remarkable properties such as excellent corrosion resistance, large elastic limit and strength, unique soft magnetic properties, wear resistance etc.

One of the most attractive aspect of metallic glasses is impressive suite of mechanical properties. Compared to crystalline material with similar composition, metallic glasses exhibit significantly high elastic limit and tensile strength, which make them prospective for applications where strength is fatal. The large elastic limit led to use in sporting goods which needs ability to store and efficiently return elastic energy. The factors governing superior mechanical properties for crystalline materials have been investigated expertly through the behavior of dislocation, structure component, and electronic theories. On the other hand, for metallic glasses with disordered structure, it has been recognized that the mechanical properties are closely correlated to the component element of metallic glasses since metallic glasses do not have grain boundary or slip system for deformation. This amorphous structure of metallic glasses derives corrosion and wear resistivity as well as superior strength and elastic limit. Two basic technique are employed to attain good corrosion resistance: formation of a solid solution phase with chemical and structural uniformity and the ability to form solid solution with beneficial element additions. For examples, Zr-based alloys exhibit high corrosion resistance over a wide range of pH in halide-free solutions [3]. Good corrosion resistance in Zr-based alloys attributes to the strong passivation ability of the main component element Zr, which is generally forms a barrier-type oxide layer. Compared to other stable crystalline material alloy, Zr-based alloys exhibits the best anodic passivation ability due to passive layers with a few nanometers thick on surface of alloy.

Recently, the applications of metallic glasses have been investigated in various fields. The Zr-Ti-Co-Be amorphous alloys showed no significant reactions in the muscle tissue over 28 days and good cellular-adhesion through in-vivo and in-vitro investigation, indicating favorable biological

performance of metallic glasses [4]. Utilizing wide supercooled liquid range when heated from room temperature, thermal formability of metallic glasses has been exploited for application in three-dimensional structure or nanopatterning technique as well as microelectromechanical systems (MEMS) [5]. The Zr and Pd-based nanowires having a diameter of 164 nm have fabricated by a fast drawing method in vacuum. This highly homogeneous and extremely elongated nanowire alloys showed high flexibility through vibration measurements, demonstrating possible application in mechanical and magnetic sensors.

In this study, mechanical behavior of nanolaminate with metallic glass and graphene is investigated. Nanolaminate with alternating layers of metallic glass and graphene is fabricated by repeating deposition of metallic glass by sputtering and transfer of chemical vapor deposition-grown graphene. In situ micro-tensile tests reveal that the addition of a very small fraction of graphene in the nanolaminate improve the elastic modulus and yield strength of the nanolaminate, comparing with those of the monolithic metallic glass. The nanolaminate also shows enhanced tensile ductility by homogeneous flow in the metallic glass layers. Using mechanical properties of metallic glass, metallic glass film is investigated for stretchable encapsulation material. Encapsulation is necessary to protect devices vulnerable to moisture and oxygen and as stretchable and wearable devices are developed, stretchability is also required in encapsulation materials. Amorphous structure of metallic glass material is advantageous in encapsulation film since diffusion path of moisture or oxygen vapor is increased comparing to crystalline or organic materials with grain boundary or large size of defects. The ternary metallic glass thin film with high thermal stability is fabricated by co-sputtering process. Electrical Ca test is performed to evaluated diffusion barrier characteristic and reveal metallic glass in the system of Cu-Zr-Ti has water vapor transmission rate of 10^{-3} order. Stretchability of ternary metallic glass thin film is evaluated as 4 % through in situ tensile testing and cyclic stretching testing, showing feasibility for stretchable encapsulation material.

Chapter 2. Theoretical Background

2.1 Amorphous metallic alloy

2.1.1 Mechanical behavior of metallic glass

Metallic glasses exhibit superior strength and high elastic limits, but they have a lack of tensile ductility that results in sudden and catastrophic failure due to intrinsic properties of atomic arrangement, disordered structure (Figure 1) [6]. Whereas dislocations in crystalline materials allow change in atomic arrangement at low energies or stress, the local rearrangement between neighborhood atoms in metallic glasses is quietly high-energy and stress required process, leading to high elastic modulus. After elastic deformation, severe plastic strain localization occurs in a shear mode with narrow region called shear band. The first observation of what are known as shear bands was found by Masumoto and Maddin [7]. They completed the comprehensive investigation of mechanical properties of metallic glass by conducting tensile tests in wide range of strain rate and temperature. It is found that the fracture strength was independent of sample dimension despite the high strength and macroscopically catastrophic failure behavior. They found that cracks or deformation lines on the surface of bent specimens and it is concluded “that plastic flow occurs in the amorphous alloys but by a process considerably different

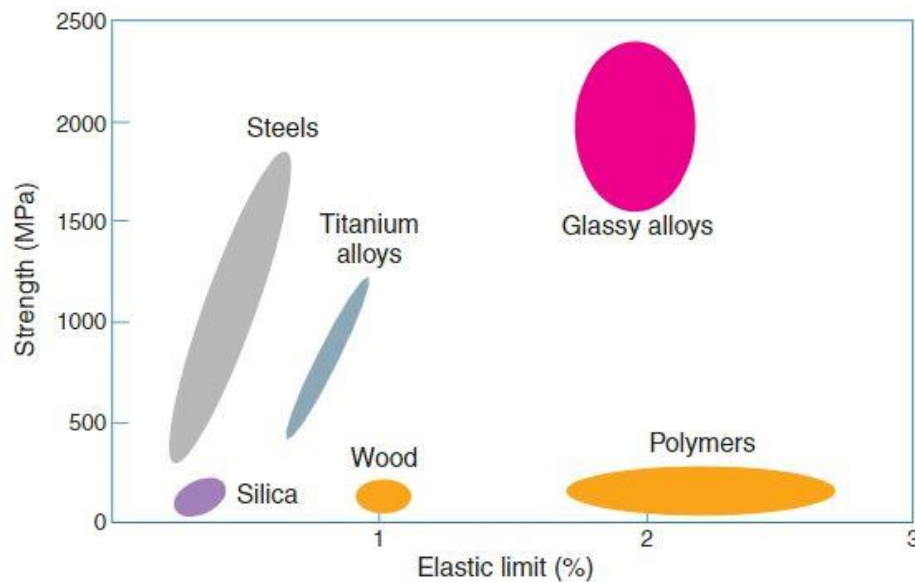


Figure 1. Amorphous metallic alloys showing higher strength than crystalline metal alloys with elasticity of polymers [6].

from crystalline material”. Interestingly, thickness line of deformation line was estimated to be 20 nm, which consistent with values of shear band thickness obtained in later investigation, mostly by transmission electron microscopy measurement. Understanding of shear band formation is important since the formation and evolution of shear bands control the yielding point and plasticity of metallic glasses at room temperature, leading to failure of materials. To understand formation and evolution of shear band in metallic glass materials, first the elementary process or event that generate shear strain have to be considered.

Argon proposed the concept of shear transformation for elementary event of metallic glass deformation, a cooperative rearrangement of a group of atoms overcoming the saddle point of an energy barrier. The exact mechanism of local atomic motion in metallic glasses is not fully verified, though fundamental unit for underlying deformation is depicted in shear transformation zone (STZ), a local cluster of atoms that accommodate shear strain [8]. This shear transformation event is very difficult to detect and characterize in experiments owing to atomic-level sized deformation. Based on numerous simulation studies for shear transformation, STZs in metallic glasses have a size of ~1 nm on average, containing a few tens to a few hundred atoms, with very wide distribution. Delogu [9] [10] reported on

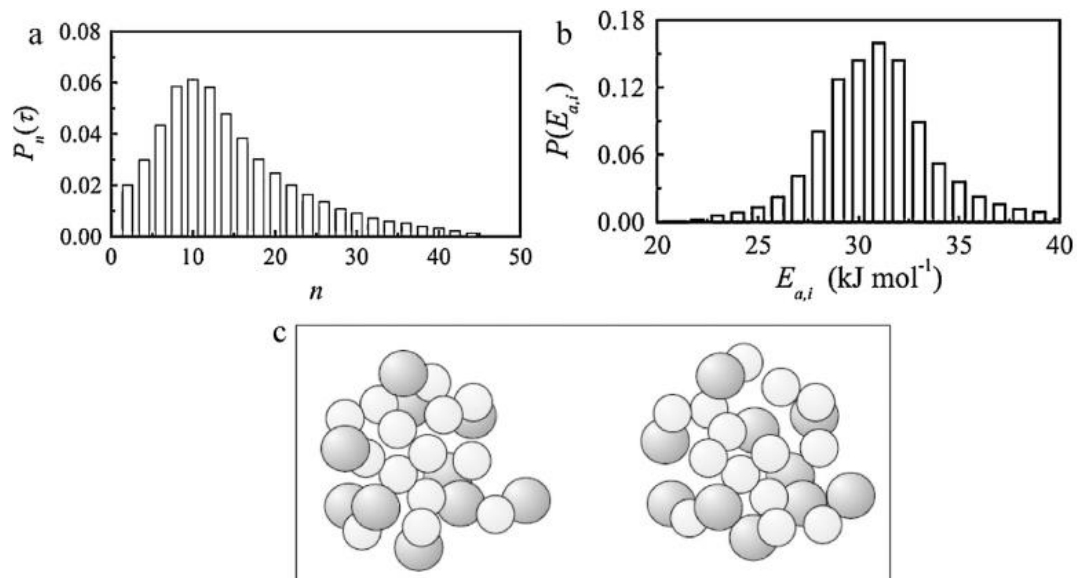


Figure 2. Model for shear transformation zones in a Ni-Ti metallic glass (a) distribution of STZs size (b) distribution of energy barrier (c) typical STZ configuration before and after shear transformation [9].

a model Ni-Zr glass material and found the STZs to have a wide size distribution centered on 10-20 atoms, with an energy barrier of about 30 kJ mol^{-1} as shown in Figure 2.

Argon suggested that when attained to critical stress activation of shear event at neighboring STZs sites lead to accumulated strain and formation of shear propagation. Schuh *et al.* reported that shear band formation process involves multiple steps: activations of individual STZs, formation on nucleus of STZs cluster, and the transition of the nucleus to a shear band. Similar other researches that investigate that shear bands are formed from stress-assisted nucleation events support theories of shear band formation. However, proving these theories for shear band formation or measuring the nucleation and propagation of shear bands are challenges since shear bands tend to propagate on time scale of 10^{-12} s and a thickness of only 10^{-8} m. Due to challenges of solving the earliest steps of shear band formation, many experimental investigations focus on statistical analysis of shear bands to get information about nucleation. For example, compression test and instrumented nanoindentation experiments are capable to approach the force-displacement data on time scale in the range of 10^{-4} to 10^{-6} s. Recent high-speed cameras have observed shear bands to frame rates as high as 5000 s^{-1} , providing details about shear band process. But, the time- and length-scales, modeling techniques still cannot obtain resolution about nanoscale motions associated with formation and deformation of shear bands in amorphous metal. Homer reported that shear localization is started from potential nucleation sites or cluster of STZs, then various stages of propagation followed through thermodynamic model in simulation [11]. It is found that stress-strain curve of nanowire deformed under a constant strain rate includes linear elastic loading, plastic yielding resulting in sudden force drop, and prolonged plastic flow at a relatively constant stress. This deformation behavior shows specific perfectly elastic model. With stress-strain curve for the constant strain rate uniaxial loading, spatial clustering of STZs activations was seen in the snapshots as shown in Figure 3. It can be seen that physical mechanism is characterized by five distinct stages: (1) linear elastic response, (2) STZ clustering, (3) growth following nucleation, (4) relaxation thickening and (5) flow thickening.

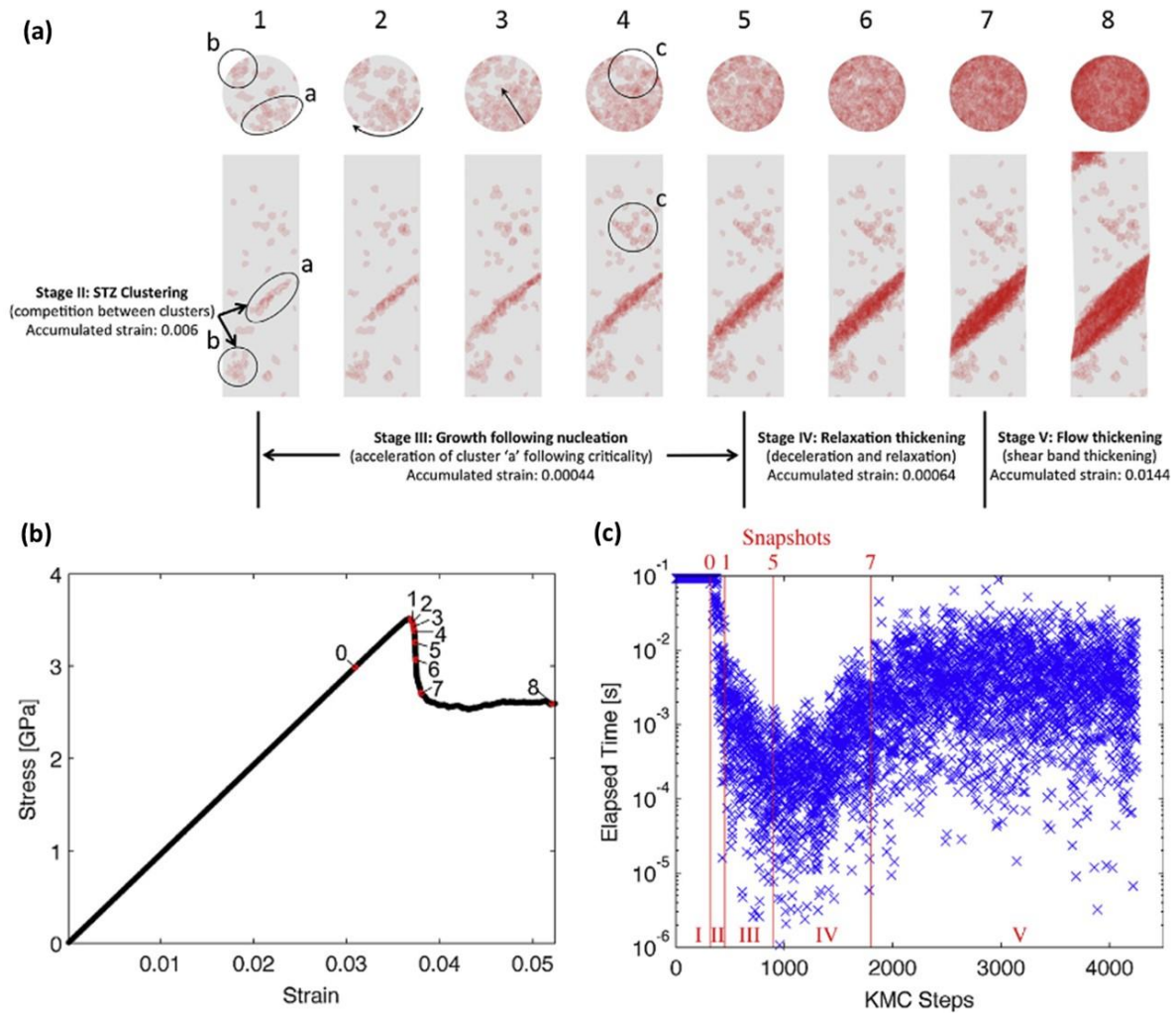


Figure 3. (a) The snapshot schematic for the evolution of the shear band into four different stages following the elastic deformation. (b) Stress-strain curve of metallic glass corresponding to snapshots of shear band formation. (c) Plot of the elapsed time according to kinetic Monte Carlo steps involved in shear band formation [11].

Stage 1 characterizes the perfectly linear elastic deformation of the amorphous nanowire. In this stage, the nanowire behaves in a perfectly elastic deformation as identified in linear stress-strain curve marked by “0”. In stage 2, the STZ clustering is characterized, which occurs between the first STZ

activation and the point where one of the activated STZ reaches the critical state for nucleation of shear band. This activation of the STZ clustering results from the increased probability of shearing between neighboring STZs separated by some distance, the statistical probability of which has been investigated in many previous researches. This clustering is also most likely to show planes oriented 45° from the tensile loading since the highest resolved shear stress occurs in these planes, leading to correspondingly high STZ activation rates along these planes. This spatial clustering can be appeared like snapshot 1 in Figure 3 (a), which shows the point at which one of the STZ clustering reaches the critical state for nucleation of shear band. This clustering point can be shown into many possible sites and is most likely to be formed on the free surface due to the reduced constraints. Finally, this clustering result in the increased probability to observe neighboring STZ activations according to elapsed time. It is notable that strain accumulating during this clustering state is just 0.006 % from the elastic deformation. The growth of the shear band immediately from the nucleation appears in stage 3. During this stage 3 of growth and nucleation of the shear band, the elapsed time between STZ activations decreases to another order of magnitude, leading to stress drop during tensile loading. However, the fact that majority of the shear plane has not been activated means that the unslipped plane with activated STZs are still experiencing high stress as shown in Figure 3 (b) and (c). As shown in snapshot 3 to 5 in Figure 3, the activated STZs start to propagate around the free surface, following which they lead to propagate to shear band across the sample. Although an additional cluster and potential nucleation site has activated as like “c” point in snapshot 4, the activated shear band below continues to expand across the sample, thereby relaxing the back half of the sample from the newly formed nucleation site. In Figure 3 (c), it is observed that stage 4, the elapsed time between activated STZs reaches the lowest value and increase, corresponding to the point at which the shear band has propagated across the sample entirely and form slip plane around 45° from the tensile loading. Lastly, stage 5 characterizes the thickening of the shear band propagation due mostly to the fact that nucleation of shear band takes a higher stress than that for continuing propagation of the shear band.

Considerable work has been aimed at improving the tensile ductility of metallic glasses. For high toughness and tensile ductility the development of glass-matrix composites is being explored [12] [13]

[14]. Two basic approaches in previous studies are employed to attain high tensile ductility: introducing a softer secondary phase in the metallic glass matrix to induce generation of local shear banding around the secondary phase and reducing its external dimensions to suppress a propagation of shear bands or occur homogeneous flow instead, leading to enhanced strength and ductility. D. Hofmann *et al.* reported Ti-Zr-based bulk metallic glasses composite with tensile ductility over 10% at room temperature and fracture energies for crack propagation as high as 340 kJm^{-2} [12]. The bulk metallic glass composites were prepared to three samples with different volume fraction of 42%, 51%, and 67% dendritic phase in a glass matrix using arc-melting and semi-solidly processing. The engineering stress-strain tensile curves for bulk metallic glass composites show failure strain in the range 9.6-13.1% and necking in the gauge section with decreasing stress. In contrast, monolithic bulk metallic glass exhibits brittle fracture behavior with a single shear band oriented at 45° . The observed tensile ductility in bulk metallic glass composites is investigated with fracture patterns. The shear bands exhibit patterns of locally parallel bands that form in domains defined by dendrites with spacing of $\sim 15 \mu\text{m}$. Through the three-point bending tests, fracture toughness of bulk metallic glass composites was determined to be 87~173

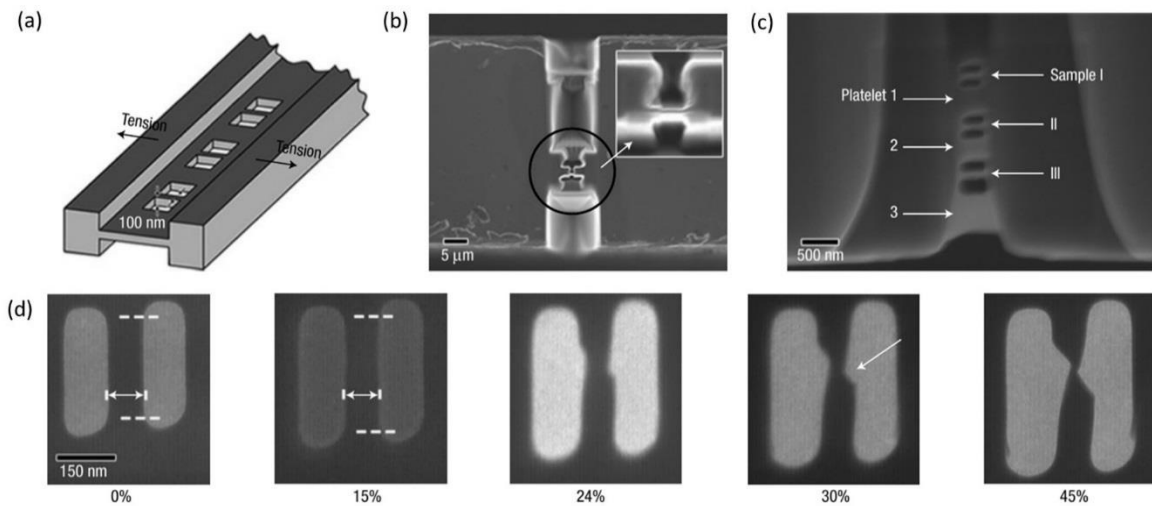


Figure 4. (a) Small-volume metallic glass samples for in situ tensile straining experiment in the TEM. Viewing directions for the first (b) and second (c) steps of FIB. (d) Images of TEM frames during the in situ TEM tensile testing [15].

MPa $m^{1/2}$, extremely high value, meaning the very high resistance to crack propagation in bulk metallic glass composites.

On the other hand, qualitatively different behavior in nano-sized metallic glasses is investigated by in situ tensile tests in a transmission electron microscope [15]. Bulk metallic glass, Zr-Cu-Al-Ni-Ti, prepared using copper mould casting was fabricated to nano-sized with gauge section of 100 nm using the dual focused ion beam micromachining technique. In situ tensile testing was carried out at a strain rate of about $5 \times 10^{-4} \text{ s}^{-1}$. Interestingly, lengths of the gauge section elongated uniformly up to a strain as high as 15% (Figure 4). The shear offset was initiated and became obvious to the elongation reached 24%. It is emphasized that the large fracture strain is achieved in small-volume of metallic glass, attributing to suppressing shear band formation and failure.

D. Jang and J. Greer reported size-dependent mechanical behavior of Zr-based metallic glass through in situ uniaxial tension tests [16]. Tensile samples of circular dimension with diameters between 100 nm and 1 μm were fabricated from bulk metallic glass disc sample by focused ion beam. Uniaxial tensile tests were carried out with tensile grips in the scanning electron microscope at a constant nominal displacement rate of 0.5-8 nms^{-1} . The stress-strain curve of 200 nm sized-metallic glass exhibit elastic loading followed by catastrophic fracture at 3-5% strain, without any plasticity (Figure 5). It seems that reduction of size to 200 nm exhibit typical deformation with shear band formation like bulk metallic glasses. On the contrary, metallic glass with size of 100 nm-diameter shows homogeneously deformation region under a uniaxial tensile loading. The true stress-strain curve obtained by directly measuring the dimension after necking show characteristics of ductile metal, nonlinear plasticity, work hardening, and necking. Homogeneous plastic deformation is demonstrated by uniform reduction in gauge section through captured images. The true stress still increases with further as a result of neck formation until fracture, showing significant work hardening. Interestingly, fracture behavior after work hardening is different from the typical ductile metal characteristic under tensile loading, failing with shearing off along 53° with respect to the loading axis. Generally, most metallic glasses exhibit fracture surface with shear band plane angle of 48° - 60° under tensile load, suggesting that 100 nm-sized

metallic glass deforms like ductile metals but fail like metallic glasses. Furthermore, work hardening of 100 nm sized metallic glass was verified by multiple-loading tension experiments. This unique deformation transition from brittle to homogeneous behavior according to size reduction is explained by two competing process of crack-like shear-band propagation and homogeneous deformation. The stress required to initiate homogeneous deformation at room temperature is independent on external dimension of metallic glass samples. Conversely, the stress for shear-band propagation gradually increases as the sample dimension decreases based on Griffith's crack-propagation criterion. This phenomenological model of two processes captures the critical sample dimension size at intersection of these two curves. When the sample dimension is smaller than the critical size, formed embryonic shear band remains to be stable and homogeneous deformation behavior occurs. Flow stress gradually increases during plastic deformation according to work hardening, and when the stress for shear band propagation is reached the fracture occurs with shear banding.

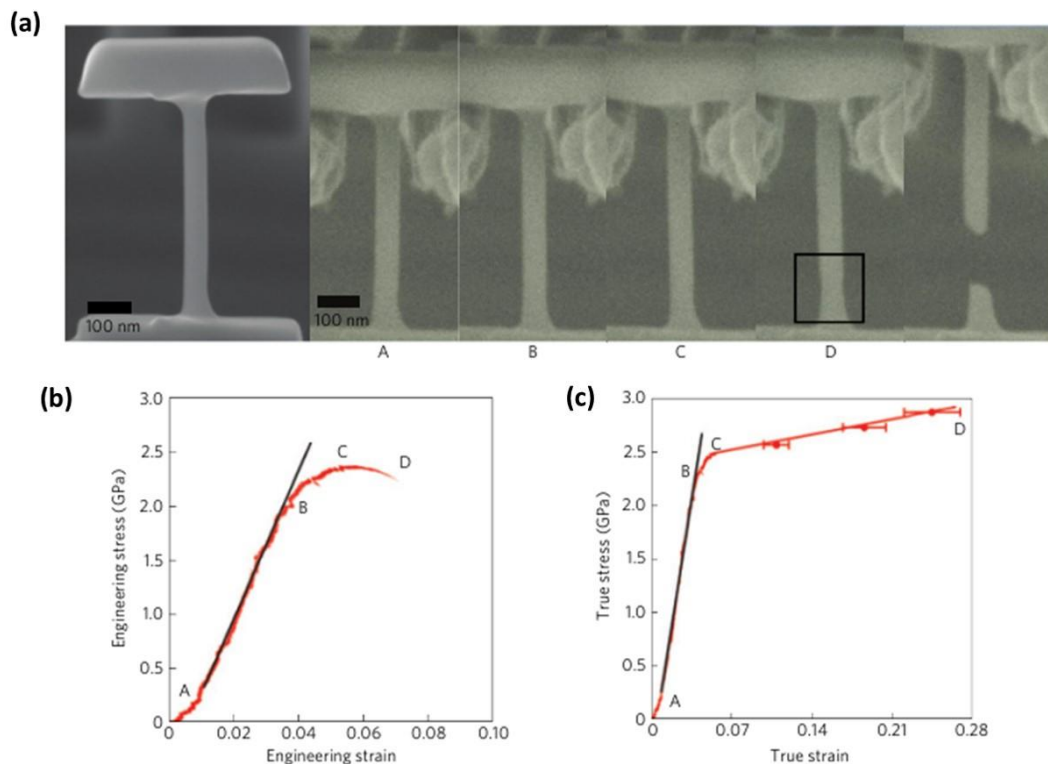


Figure 5. Monotonic nanotension results for the 100 nm-diameter sample. (a) SEM images captured from a movie during an in situ tension testing. (b) The engineering and (c) true stress-strain curves of tension test. True stress-strain after necking were obtained by directly measuring the diameter [16].

Although numerous researches have been made based on metallic glasses materials, most metallic system has multi-component elements by arc-melting or molding process, which make it difficult to investigate the glass forming ability. Consequently, simple preparation method for amorphous alloy system is developed using sputtering. Among many glass former systems, Cu-Zr binary metallic glass systems are particularly promoting for mechanical and structural applications due to their wide composition range of glass forming ability [17]. Figure 6 shows phase diagram illustrating glass forming range of Cu-Zr system with several structures observed in intermetallic phases.

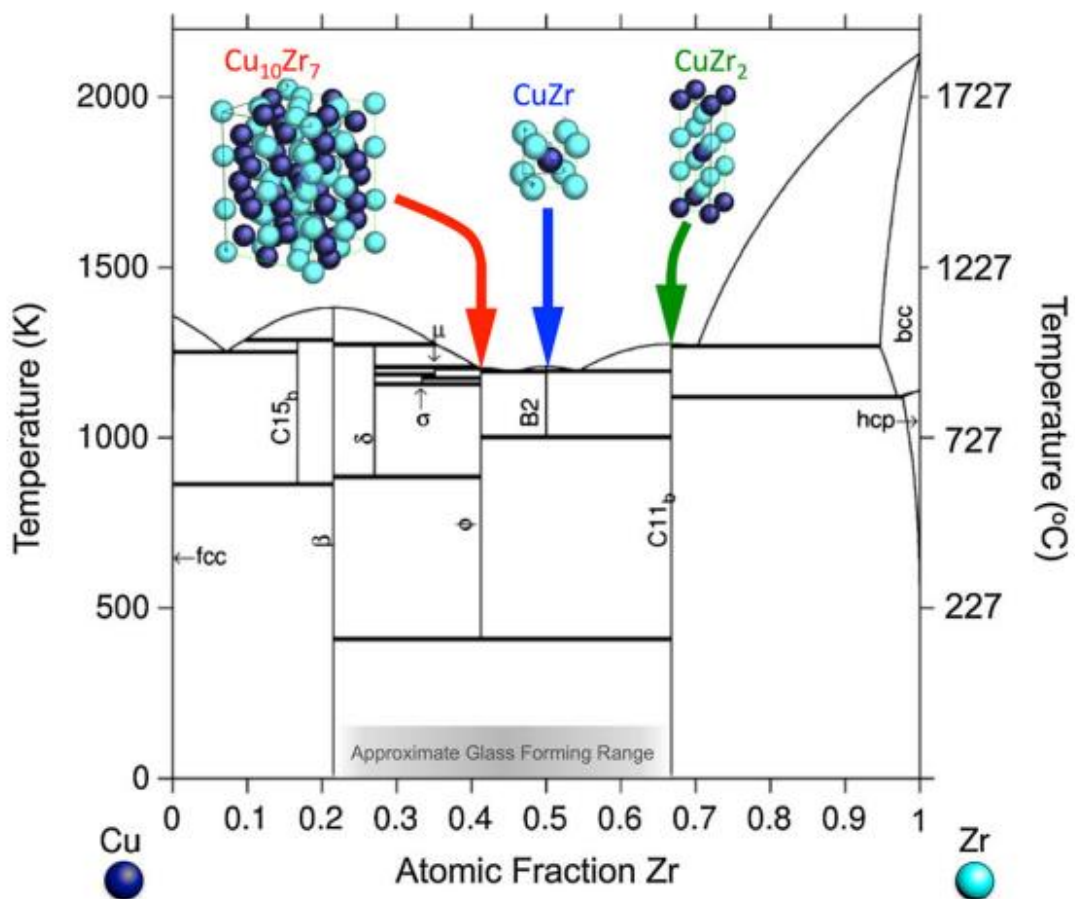


Figure 6. The equilibrium phase diagram of Cu-Zr system. The shading of the composition range of 20 to 70% shows strong glass forming ability of Cu-Zr system [17].

Several researches including the structure, mechanical properties, and superconductivity characteristic of the Cu-Zr amorphous film were reported. Dudonis *et al.* fabricated amorphous films in a wide composition range of Zr_xCu_{100-x} ($5 \leq x \leq 95$) by magnetron sputtering deposition method at high working power [18]. Although wide range of Cu-Zr film can be formed easily, detailed structure analysis such as roughness and amorphous structure confirmation were concealed. J. Qin *et al.* reported that amorphous Zr_xCu_{100-x} films can be formed by magnetron sputtering at relatively low sputtering power and investigated formation of amorphous film depending on sputtering conditions [19]. The structure was confirmed using X-ray diffraction (XRD) measurements. The film with composition Zr_xCu_{100-x} showed the crystalline characteristic evidently in XRD patterns. With the increasing content of Zr component in the range of $35 \leq x \leq 65$, crystalline characteristics were weakened. Within specific range of Zr component in Cu-Zr films XRD spectra present one broad diffuse peak, indicating an amorphous structure obtained. Thus, it can be concluded that the glass forming ability in Cu-Zr amorphous films increases with increasing of Zr component in the range of $35 \leq x \leq 65$. This result is apparently different from the bulk metallic glass characteristics.

It has been reported that $Zr_{35}Cu_{65}$ alloy fabricated by casting was proved to be a high glass former since it was fabricated around the eutectic composition from high stability liquid which was beneficial for glass formation. However, this composition, $Zr_{35}Cu_{65}$ film, fabricated by sputtering showed rather low amorphous formation ability. Additionally, deposition conditions such as substrate temperature and argon gas pressure influenced the structure of amorphous alloy film. A higher pressure and substrate temperature are unfavorable to the formation of amorphous structure during the film deposition. Furthermore, deposition conditions on the film plays a vital role to properties because residual stress can be formed during deposition film [20]. Residual stress, either in compression or tension, in film deposited by sputtering is associated with lattice misfit between film and substrate, particle bombardment, and deposition conditions such as substrate bias and working pressure. The residual stress in film also play a crucial role to mechanical properties including hardness, substrate fatigue, and adhesion between film and substrate. It is important to further evaluate the effect of film thickness on the residual stress. It is reported that compressive stresses present in Zr-based thin film metallic glasses

and the increasing tendency of stress with increasing film thickness when a bias is applied to the Si substrate as shown in Figure 7 [21].

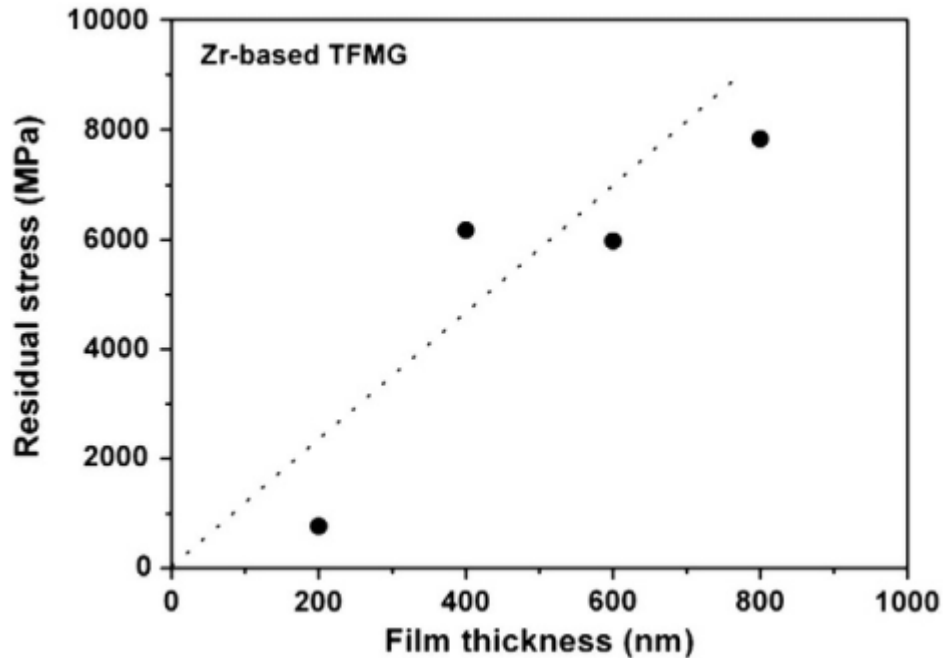


Figure 7. Relationship between compressive residual stress and film thickness of Zr-based thin film metallic glasses deposited by sputtering [21].

It is shown that thin film with small compressive stress is favorable for increasing the resistance to crack initiation and propagation. The fatigue-life improvements in the coated substrate by thin film are mainly attributed to the compressive residual stresses present in the coating materials and to the good adhesion of the coating to the substrate [22] [23].

Recently, there are many studies that the glass forming ability of metallic glass increases by introducing additional element. Especially, it is reported that glass forming ability of Cu-Zr system increases significantly with one of the transition metals such as Al, Ti, Ni, or Ag. For example, Cu-Zr-Al metallic glasses have been attracted greatly due to their high glass forming ability and mechanical properties. Wang *et al.* investigated glass forming ability of Cu-Zr-Al

system using DSC and DTA analysis depending on composition of Cu, Zr, and Al elements. As shown in Table 1, the best metallic glass formers were determined to be $Zr_{48}Cu_{45}Al_6$ system within changed 1 at.% shift in composition showing fully amorphous morphology [24]. They found that glass forming ability of metallic glass is strongly dependent on composition of the system even 1 at.% difference of composition. In essence, developed model establishes a microstructure-based analysis for a practical strategy to figure out the alloy composition with optimum glass forming ability by monitoring microstructure evolution in amorphous matrix.

Alloy label	Composition	Morphology	T_m (K)	T_1 (K)	T_g (K)	T_x (K)	T_{fg}	ΔT_x (K)	γ	ΔH_x (J/g)
8	$Zr_{50}Cu_{34}Al_{16}$	Fully crystalline in the center	1123	1209	–	–	–	–	–	0
2	$Zr_{50}Cu_{36}Al_{14}$		1121	1188	724	771	0.609	47	0.403	28
1	$Zr_{50}Cu_{38}Al_{12}$	Composite: (amorphous + τ_3)	1122	1170	722	774	0.617	52	0.409	44
7	$Zr_{50}Cu_{40}Al_{10}$		1122	1176	714	770	0.607	56	0.407	46
55	$Zr_{50}Cu_{43}Al_7$		1122	1181	703	763	0.595	60	0.405	52
11	$Zr_{46}Cu_{42}Al_{12}$	Fully crystalline in the center	1123	1262	–	–	–	–	–	–
39	$Zr_{46}Cu_{44}Al_{10}$	Composite: (amorphous + τ_5)	1125	1223	726	782	0.594	56	0.401	47
40	$Zr_{47}Cu_{45}Al_8$		1125	1218	714	772	0.586	58	0.400	54
64	$Zr_{49}Cu_{44}Al_7$	Fully amorphous	1126	1184	704	764	0.595	60	0.405	59
67	$Zr_{48}Cu_{45}Al_7$		1125	1186	708	766	0.597	58	0.404	59
56	$Zr_{49}Cu_{45}Al_6$		1126	1187	704	758	0.593	54	0.401	58
45	$Zr_{48}Cu_{46}Al_6$		1125	1192	706	762	0.592	56	0.401	58
57	$Zr_{49}Cu_{46}Al_5$		Composite: (amorphous + ZrCu)	1126	1195	701	750	0.587	49	0.396
62	$Zr_{49}Cu_{47}Al_4$	1126		1208	697	745	0.577	48	0.391	21

Table 1. Thermal properties of various metallic glass in Cu-Zr-Al ternary system [24].

2.1.2 Multilayer of metallic glass

In addition to monolithic metallic glasses, multilayered thin film metallic glasses have attracted attention in research during recent years. Since there are limited structural applications for monolithic metallic glass with dimensions of the order of 100 nm, nanolaminates with alternating layers of metallic glass (with dimensions of 100 nm or less) and another material have been suggested as a more practical material. For enhancing mechanical properties, multilayered structure consisting of thin layers of nanocrystalline metal and metallic glass are prepared. Cu(111) films showing face centered cubic structure appear to be too soft, whereas Mo(110) films showing body-centered cubic structure are too brittle as interfacial material. Hexagonal close-packed Zr(001) films is reported to the metal layer well matched with metallic glass thin film, sufficiently strong in mechanical properties while being deposited [25]. Multilayered thin film with nanocrystalline Zr(001) layer with nano-twinning and metallic glass layer exhibited highly ductile behavior, even more than many pure metals, with semi-uniform plastic deformation up to 55%. This is attributed that shear bands initiated from metallic glass layer can be absorbed and accommodated by nanocrystalline Zr(001) layer with nano-twinning. Figure 8 showed ductile plastic deformation of multilayered thin film metallic glass with Zr(001) layer. In addition to nanocrystalline metal interlayers, metallic glass thin film of different composition has been used to as interlayer for multilayered structure. Zr-based metallic glass/Pd-based metallic glass multilayered system has been investigated through uniaxial micro-compression and nanoindentation testing [26]. It is found that apparent deformation mechanism transition from a inhomogeneous mode to homogeneous mode is appeared in micropillars of multilayers consisting of two kinds of metallic glasses. Similar phenomena were observed through nanoindentation. The presence of keen interfaces between amorphous layers, which could suppress the shear band propagation, is a possible reason for the observed deformation transition in micro-compression test.

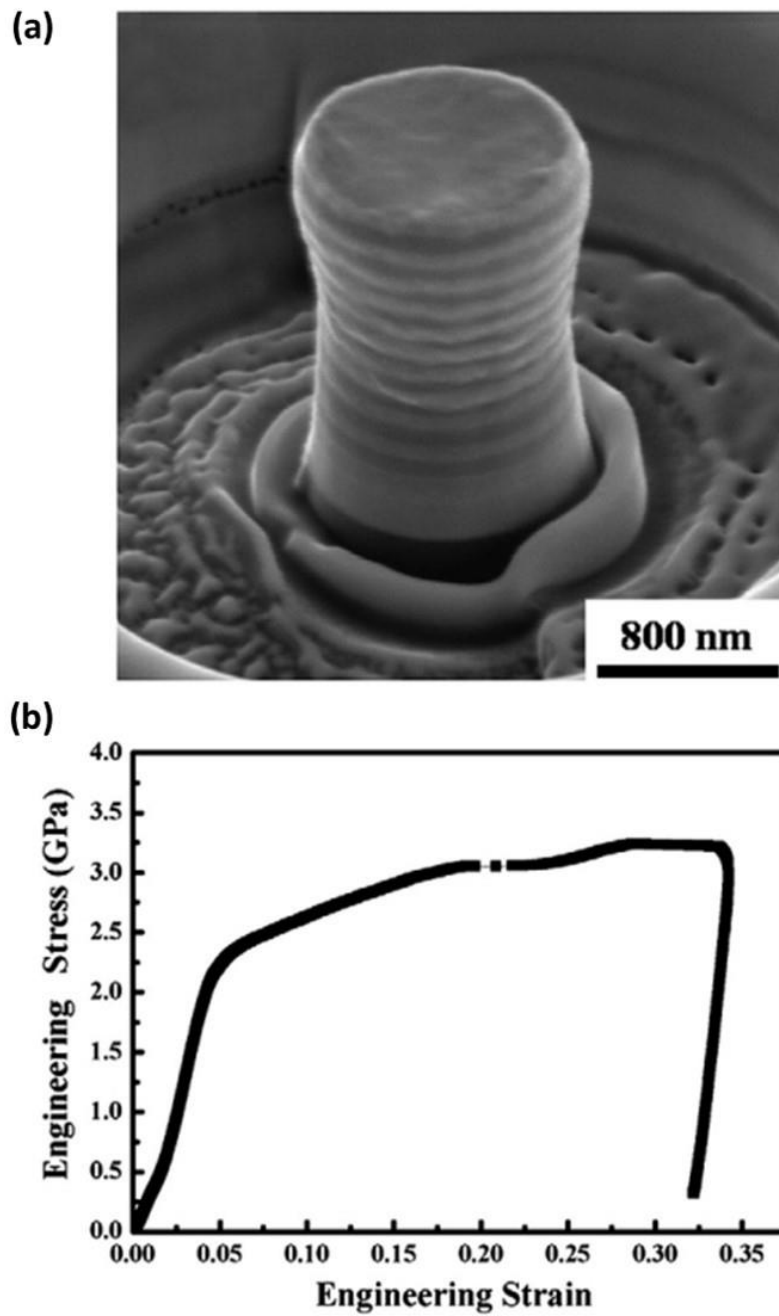


Figure 8. (a) SEM image of multilayered thin film pillar with metallic glass and Zr layer on Si (001) after compression test up to 25% strain and (b) the recorded engineering stress-strain curve [25].

The tensile behavior of multilayer thin film metallic glasses has been also investigated. Metallic glass-based nanolaminates with proper interfacial material and optimum layer thickness exhibit improved strength and ductility by utilizing size-dependent homogeneous flow of metallic glass [27]. Nanolaminates with metallic glass and nanocrystalline Cu showed clear change in mechanical behavior at the 112-128 nm thickness range of metallic glass layer. The monolithic metallic glass and the nanolaminates with thickness greater than 128 nm all exhibit similar mechanical behavior, elastic loading followed by very limited plasticity ($\sim 0.5\%$). On the other hand, the nanolaminates with thickness of 112 nm metallic glass attained the maximum strength of 2.5 GPa overall and a fracture strain of 4%, representing a significant improvement over the monolithic metallic glass sample. Through the transmission electron microscopy analysis, it is supposed that the enhanced strength and ductility are arose from the thickness-dependent deformation of the metallic glasses rather than other mechanism such as interfaces, multiple shear band formation, and effect of volume fraction. Analytical model is proposed to understand size-dependent deformation behavior of metallic glasses using UTS as a function of metallic glass thickness, consisting of upper and lower plateaus below and above the critical thickness of metallic glass. As shown in Figure 9(b), the suggested analytical model agrees with the experimental data very well.

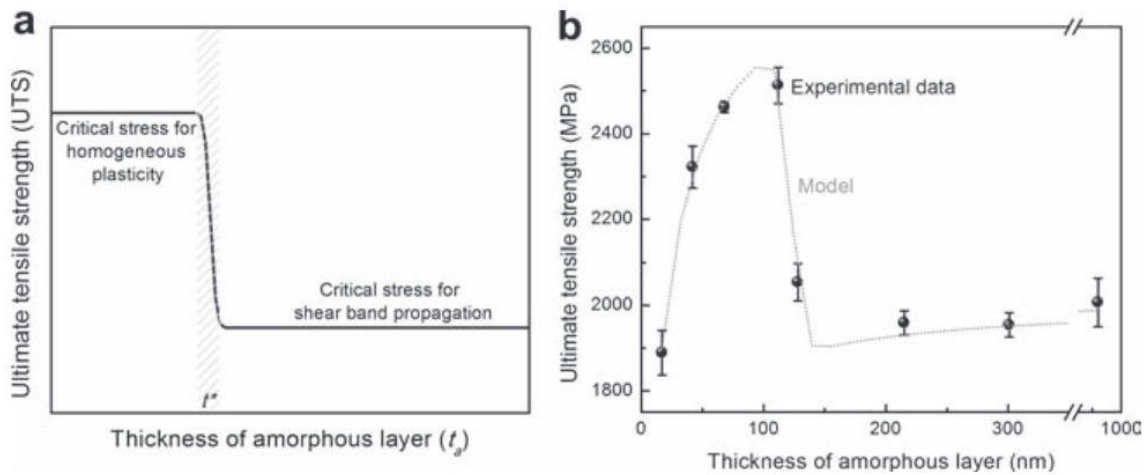


Figure 9. (a) Ultimate tensile strength profile of amorphous $\text{Cu}_{50}\text{Zr}_{50}$ layer dependent on thickness of amorphous layer. (b) Model developed for ultimate tensile strength of nanolaminates fitting to experimental data [27].

2.2 Encapsulation for stretchable devices

2.2.1 Thin film encapsulation

Devices based on organic materials for active layers are extremely sensitive to water vapor and oxygen, which cause their degradation. There have been reported many mechanisms for the degradation of devices such as oxidation of cathode or polymer layers, detachment of organic layer from the anode or cathode, diffusion between emitting layer and hole transport layer, electrical shorts, electrochemical reactions on electrodes, oxygen-activated photochemical damage. Liew *et al.* found that dark spots on cathode resulted from cathode delamination at ambient conditions [28]. When the cathode with dark spots were peeled off and newly deposited, the devices showed uniform emission. This indicates that the cause of dark spot appearance was cathode delamination. The growth of dark spots is associated with degradation in the organic layers, especially between organic and cathode layers. A. Turak reported that black spots occur in an electroluminescent polyfluorene system with poly (styrenesulfonate)-doped poly (3,4-ethylenedioxythiophene) (PEDOT:PSS) on ITO for the anode and Ca/Al for the cathode [29]. A localized electrochemical reaction such as reduction of the doped PEDOT:PSS and oxidation of the active metal appeared around the pinhole defects with the non-emissive disks. A common reason for causing the device degradation is the penetration of oxygen and moisture. Specially, in the case of perovskite, which is being studied extensively as a solar cell, it is also vulnerable to heat as well as oxygen or moisture [30]. Therefore, encapsulation is an essential technology to protect the devices from the oxidation caused by water and oxygen penetration and mechanical impact externally, leading to prolong the lifetime of the devices.

Recently, stretchable and wearable devices are attracting attention in the device industry and various researches have been reported as next-generation displays and electronics. To actualize stretchable devices, stretchable encapsulation materials and process should be developed simultaneously. The most popular encapsulation technique is to use glass lid using glass frit or epoxy resin as shown in Figure 10(a) [31] [32]. It is the most effective for prevention of moisture penetration, but it makes the size of devices to increase and epoxy sealing can be penetration path of oxygen and

moisture. Most of all, it cannot be applicable to flexible, wearable, and stretchable devices since glass lid can be broken easily when folding or stretching. Since this conventional encapsulation technique is ineffective due to the rigidity of the lid, several flexible encapsulation approaches have been developed including barrier-coated flexible lid and monolithic films, shown in Figure 10(b) and (c), respectively, called thin film encapsulation.

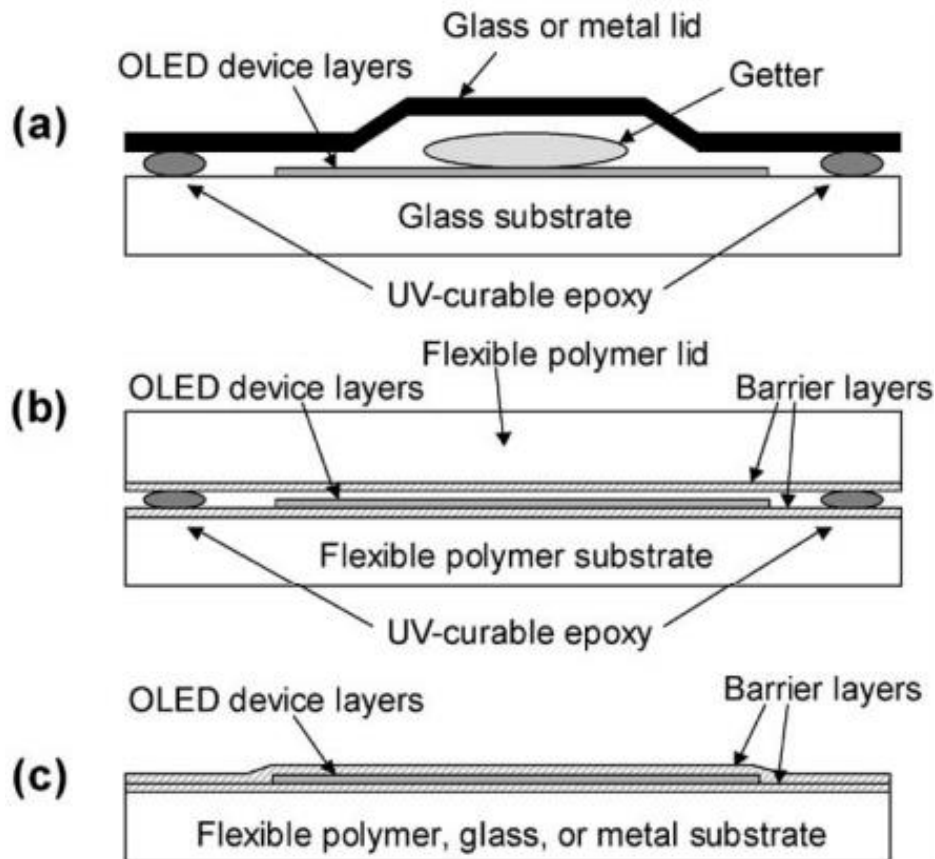


Figure 10. Schematic diagrams for encapsulation techniques; (a) conventional method using glass lid, (b) laminated barrier layer lid, and (c) monolithic thin film coating [31][32].

Thin film encapsulation (TFE) technique has been developed to improve impermeability while ensuring flexibility. Especially, TFE technique forming encapsulating layers that is flexible and prevent moisture penetration has been suggested by repeating spin coating of organic layer and atomic layer

deposition (ALD) of an inorganic layer. The ALD method has self-limiting growth mechanism based on sequential, alternate, self-limiting reactions on the top surface, ensuring the growth of thin film with excellent uniformity and conformity. For example, Al_2O_3 thin film grown by ALD process using trimethylaluminum (TMA) and H_2O is reported. The experimental analysis with deposition conditions revealed that hydrogen content in film increased and densities of thin film decreased with decreasing growth temperature. Through ALD process, compact multilayer films can be achieved by A-B binary sequential reactions, separated by washing flowing between A-B reactions [33]. This compact multilayer film grown by ALD process is promising material for thin film encapsulation. By prolonging the penetration of water vapor and oxygen, encapsulation performance can be improved through hybrid nanolaminate structure. According to some previous investigations, Al_2O_3 single thin film and Al_2O_3 - ZrO_2 hybrid film exhibited an amorphous structure as shown in Figure 11.

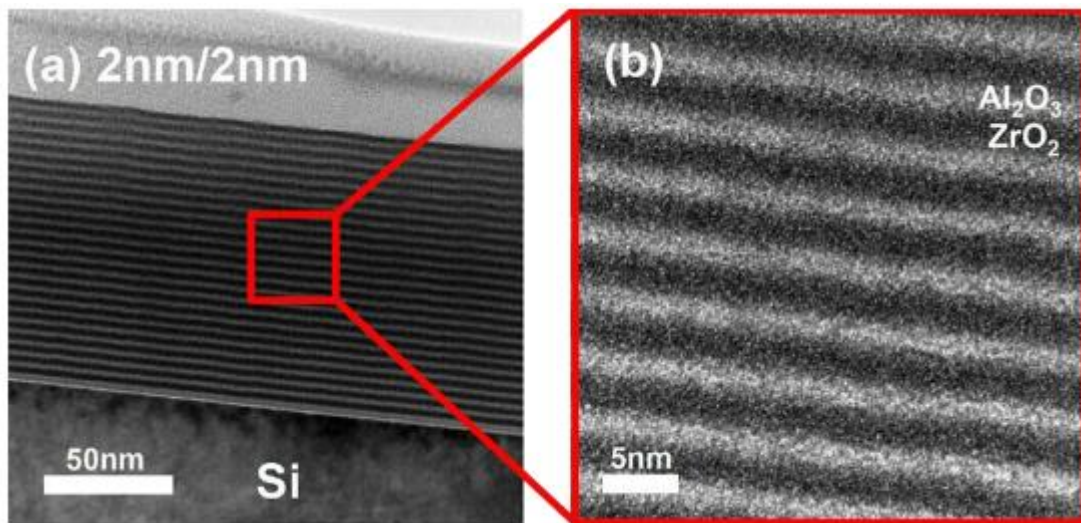


Figure 11. Transmission electron microscopic images of cross-sectional Al_2O_3 - ZrO_2 hybrid film grown by ALD process at (a) low resolution and (b) high resolution [33].

Seo *et al.* reported thin film encapsulation layers prepared by ALD at low temperature, 80°C , and investigated effect of thin film encapsulation through Al_2O_3 / ZrO_2 nanolaminate with optimized for thickness of each layer [34]. Al_2O_3 / ZrO_2 nanolaminate were prepared by repeated deposition of each

layer with the desired number of cycles and thickness. The growth rate per each cycle of Al_2O_3 and ZrO_2 was determined to be 1.1 and 0.9 Å, respectively, on SiO_2/Si substrate. The encapsulation performance was investigated using Ca test under 85°C and 85% relative humidity environment. The moisture barrier performance was enhanced with increasing the number of interfaces in nanolaminate. When the 30 nm-thick $\text{Al}_2\text{O}_3/\text{ZrO}_2$ nanolaminate with alternating layers of 1 nm-thick Al_2O_3 and ZrO_2 layers, the effect of the number of interfaces on the moisture barrier performance was investigated depending on thickness ratio of Al_2O_3 and ZrO_2 layer thickness while maintaining the number of interfaces in nanolaminates.

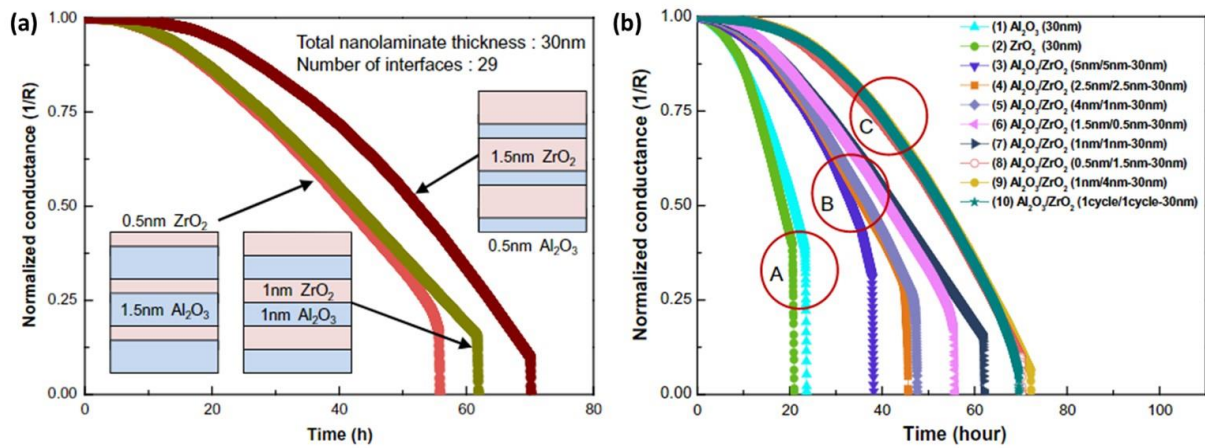


Figure 12. Encapsulation performance of $\text{Al}_2\text{O}_3/\text{ZrO}_2$ nanolaminate with different number of dyads and thickness of each layer. (a) Ca-test results of three different nanolaminate structures with the same number of interfaces. (b) Ca-test results of pure Al_2O_3 and ZrO_2 , and eight different nanolaminate structure dependent on thickness of each layer [34].

As shown in Figure 12(a), even though the total thickness and the number of interfaces were the same for the three different structure, the time to complete the oxidation of Ca sensor exhibited differently. This result indicated that moisture barrier performance is affected by the material and thickness of that as well as the number of the interfaces. In order to find the most effective nanolaminate structure for moisture barrier, 10 different 30 nm thick nanolaminate including single thin films, Al_2O_3 and ZrO_2 , are

prepared and categorized into 3 groups depending on thickness and dyads of each layer. As shown in Figure 12(b), single thin films, Al_2O_3 and ZrO_2 , showed the worst moisture barrier performance. Group C including $\text{Al}_2\text{O}_3/\text{ZrO}_2$ nanolaminate structures, 6 dyads of 1/4 nm, 15 dyads of 0.5/1.5 nm, and 150 dyads of 1.1/0.9 nm for $\text{Al}_2\text{O}_3/\text{ZrO}_2$, exhibited the best moisture barrier performance. To summarize the results, more the number of interfaces was better for the moisture barrier performance and the maximum ZrO_2 thickness per layer was determined to be under 4 nm in order to maintain the layer to be amorphous structure, leading to good moisture barrier property. With advantages of inorganic amorphous layer grown by ALD process, various multi-barrier and nanolaminate barrier have been reported as thin film encapsulation of flexible organic light emitting diodes. It is reported that nanolaminate structure using organic layer is introduced to the $\text{Al}_2\text{O}_3/\text{ZnO}$ multi-barrier system to satisfy required conditions of complicated and longer diffusion path as well as flexibility for flexible encapsulation [35]. Al_2O_3 and ZnO were deposited by thermal ALD system at a chamber temperature of 70°C as the materials of nano-stratified structure and a silica nanoparticle-embedded sol-gel organic-inorganic hybrid nanocomposite (S-H nanocomposite) was used as hybrid nano-stratified moisture barrier film. All organic and inorganic layers were coated onto PET substrate alternately. As shown in Figure 13, thickness of nano-stratified layer and organic S-H nanocomposite is 30 nm and 120 nm, respectively. The nano-stratified stack includes 5 pairs of Al_2O_3 and ZnO with each thickness of 3 nm. The hybrid nano-stratified moisture barrier structure consisting of 2.5 dyad stack of $\text{Al}_2\text{O}_3/\text{ZnO}$ multi-barrier and S-H nanocomposite with a total thickness of 330 nm and was measured using a high-resolution transmission electron microscope. The conductance change with time duration of Ca sensor encapsulated by hybrid nano-stratified moisture barrier was investigated to confirm the moisture barrier performance. As shown in Figure 13(d), the nano-stratified structure exhibited a better moisture barrier property than that of the each single layer, Al_2O_3 and ZnO and Figure 13(e) shows the effect of the number of dyads on barrier performance.

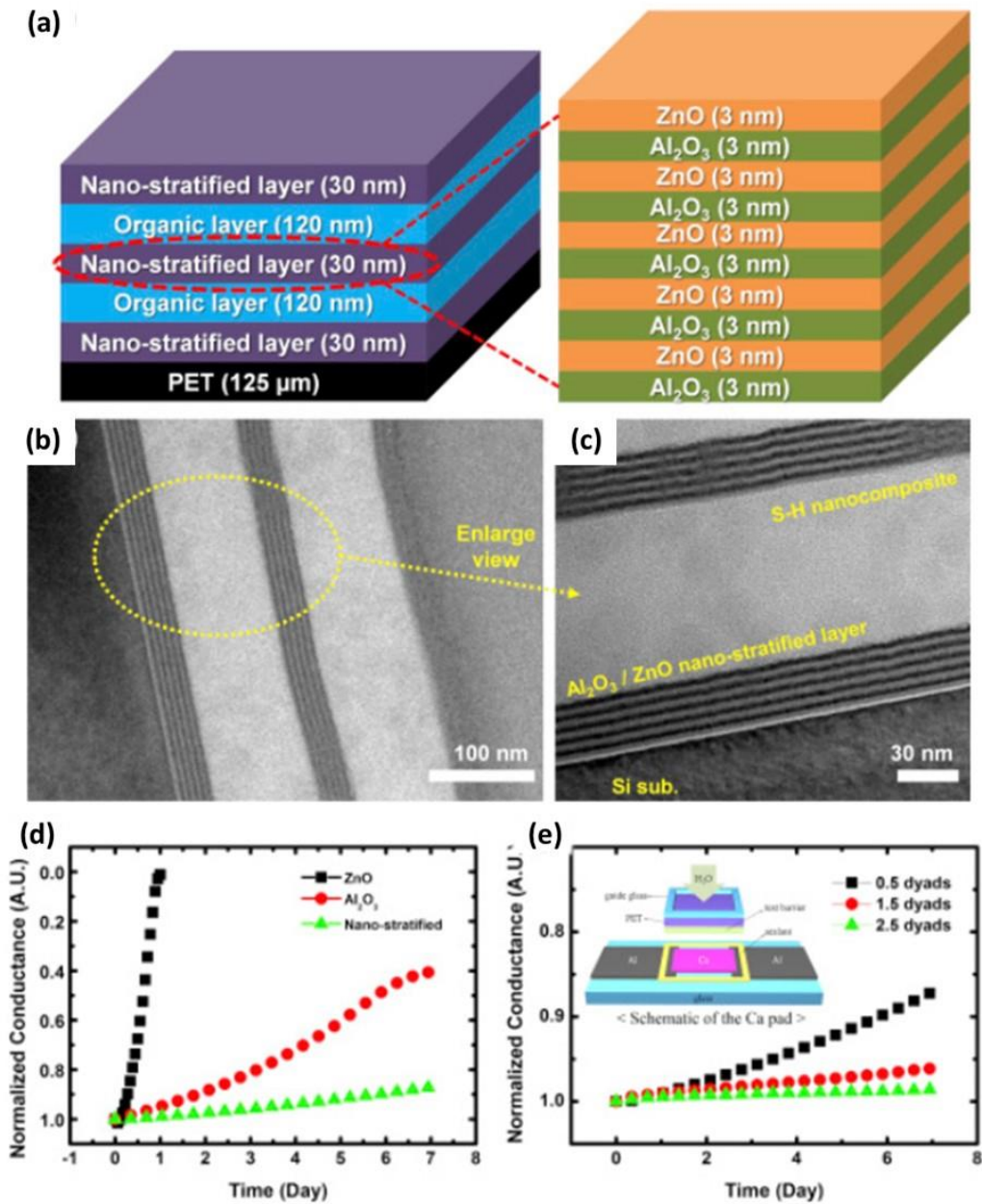


Figure 13. (a) Schematic diagram of the hybrid nano-stratified moisture barrier with 2.5 dyads stack. Cross-sectional TEM image of (b) total stack structure and (c) magnified view of 1 dyad with nano-stratified stack and nanocomposite layer. Electrical Ca test results of (d) single inorganic single layers and nano-stratified barrier and (e) hybrid nano-stratified barrier structure depending on the number of dyads [35].

For flexible OLEDs application, it is necessary to ensure flexibility with moisture barrier performance. The hybrid nano-stratified barrier structure showed moisture barrier performance even after 1000 cycles and bending radius of 3 cm during bending test. To identify the application in OLEDs, J-V-L characteristic of devices encapsulated by hybrid nano-stratified barrier was compared with that of no-encapsulated device. Figure 14 (a) and (b) shows the J-V-L characteristic of devices, confirming that the devices without or with thin film encapsulation of the hybrid nano-stratified barrier structure has almost same performance. Additionally, cell images of device were captured over the time duration under 30°C and 90% relative humidity environment. Figure 14(c) shows that after 30 days from the fabrication and bending test the luminance of the devices was decreased slightly to 93.5% compared with the initial state, while device without encapsulation was rapidly degraded with black spots just after 1 hour, confirming feasibility in application for thin film encapsulation.

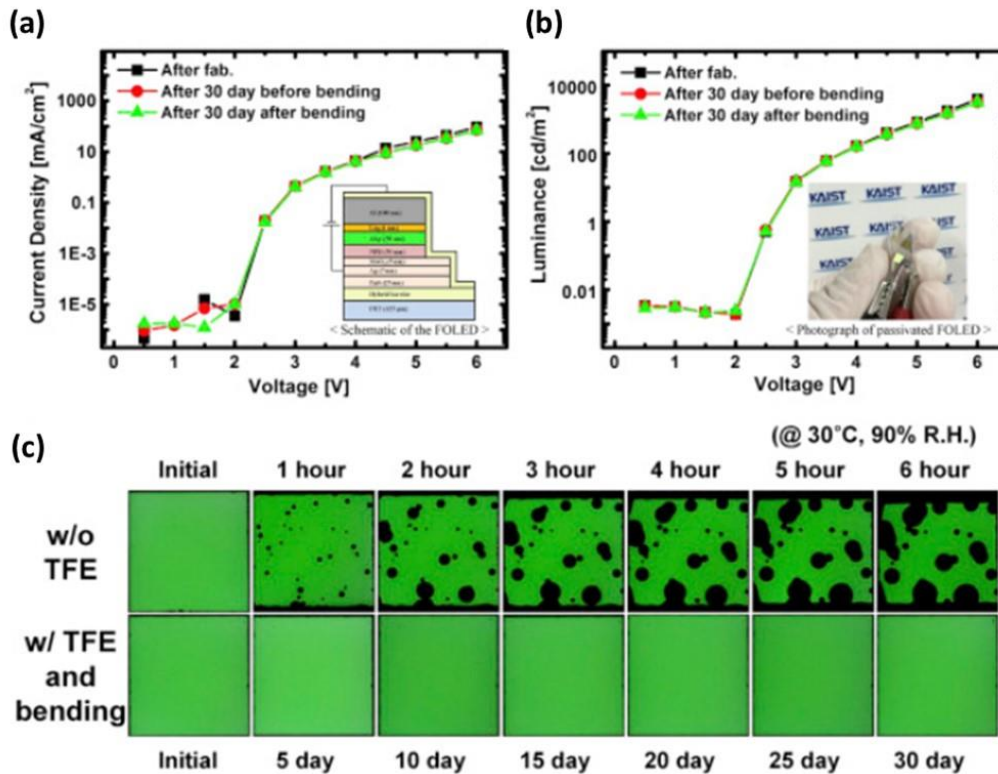


Figure 14. (a) J-V curves and (b) L-V curves of thin film encapsulated device using hybrid nano-stratified barrier after fabrication for a 30-day period, and (c) Optical images with time duration of un-encapsulated and encapsulated cell under severe conditions [35].

However, spin coating process requires contact with the device directly which can damage to organic materials by solvents. ALD process has demerits such as long processing time, high cost, and low throughput. Park *et al.* developed a novel flexible encapsulation process to enable roll-to-roll (R2R) process using Fe-Ni alloy metal foil (Figure 15) [36]. Flex Lami-capsulation process consists of surface treatment with a self-assembled monolayer (SAM) to increase adhesion between metal foil and rubbery polymer layer, polydimethylsiloxane (PDMS). This PDMS layer has three important roles in flex lami-capsulation; an insulator, intimate contact with devices, and buffer layer to protect the device from outside influence like R2R process later. This Flex Lami-capsulation method is a simple, low cost, fast, and scalable encapsulation method that is appropriate for R2R process. Organic electronic devices (OEDs) was encapsulated by developed Flex Lami-capsulation method and electrical properties and luminance of encapsulated OEDs was measured. Compared to glass-encapsulated OEDs, Flex Lami-capsulated OEDs showed almost identical electrical characteristics and lifetime. Bending stability of OEDs encapsulated by Flex Lami-capsulation was improved to bending radius of 8 mm, attributing to changing position of the neutral plane. Although the Flex Lami-capsulation was demonstrated to be applicable in large-area production and R2R process, it is still limited to water vapor penetration through epoxy like glass-encapsulation method and stretchability of 1.6% when it is evaluated as elasticity.

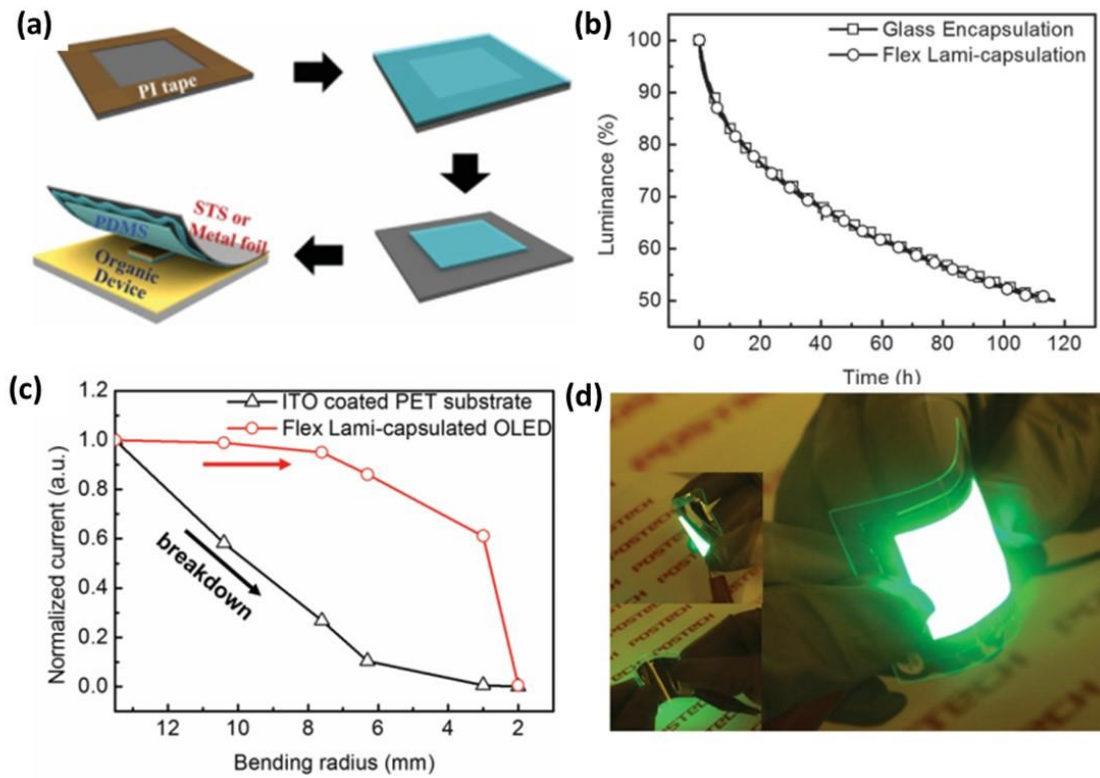


Figure 15. (a) The flexible lamination encapsulation process. (b) Lifetime measurement of encapsulated OLEDs. (c) Bending stability measurements of ITO-coated PET substrate and Flex Lami-capsulated OLED fabricated on ITO-coated PET substrate according to bending radius. (d) Demonstration for large-area OLEDs encapsulated with Flex Lami-capsulation [36].

2.2.2 Water vapor transmission rate

Moisture permeation rate, also water vapor transmission rate (WVTR), refers to the amount of moisture permeated through a barrier film per a unit area during the day. There is wide range of water vapor transmission rate requirements for various materials and applications. In the case of devices such as organic light-emitting device and solar cells that are chemically very reactive cell and electrodes, the lowest permeation rate is required since they have the highest sensitivity to moisture, occurring degradation of organic cell and electrode with permeated moisture. It is reported that the requirement WVTR of an OLEDs lifetime for 10000 hours is $1 \times 10^{-6} \text{ gm}^{-2}\text{day}^{-1}$. The WVTR requirement for organic thin film transistor application is in the range of 1×10^{-1} to $1 \times 10^{-3} \text{ gm}^{-2}\text{day}^{-1}$, are not as strict as that for OLEDs. Figure 16 shows the order of magnitude for required barrier performance for various electronic devices [37]. For barrier property requirement of various electronic devices, various materials are suggested as thin film encapsulation. Currently, the most effective method to prepare thin film encapsulation and to block moisture permeation while retaining reliable flexibility is to use multilayer barrier films by alternating layers of organic and inorganic materials. However, there are several challenges to understand the mechanisms of moisture permeation in multilayer barrier thin film structure, such as direct imaging and characterization of defect size, impractical measurement of effective diffusivity and solubility, and difference in diffusion characteristic of materials on different substrate. Considerable researches have been proposed to investigate the moisture permeation mechanism of thin film materials.

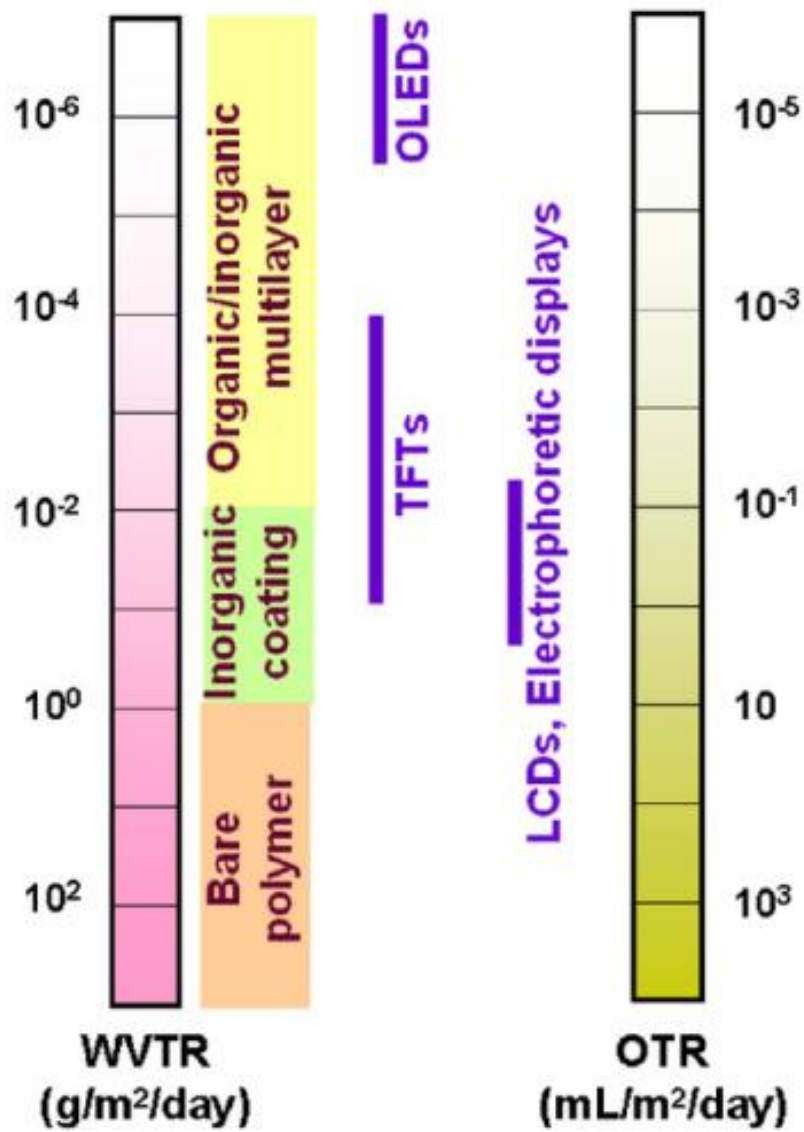
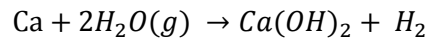


Figure 16. Diagram of the required water vapor transmission rate and oxygen transmission rate for various electronic devices [37].

Highly sensitive permeation measurement is crucial for the characterization and development of encapsulation materials, especially organic light emitting diodes (OLEDs), which are required very low permeation rate on the order of 10^{-6} g/m²/day for water vapor at ambient environment. Permeation rate of oxygen and water vapor can be measured with standard facilities from MOCON and Brugger. The permeated materials are detected by a coulometric sensor or electrolysis, respectively. Both equipments can measure the permeation rate range of 10^{-3} g/m²/day. These commercially available systems cannot meet the sensitivity requirements of permeation rate for OLEDs. Therefore, new measurement methods have been developed. One of suggested approaches is Ca test, utilizing sensitive characteristic of Ca with water and oxygen. This involves observations of the optical or electrical changes of Ca. Reaction pathway of Ca with water is as following:



The mass transport rate of water vapor, R_w , through the film with area A_f is given by,

$$R_w = WVTR \cdot A_f \quad (1)$$

The mass consumption rate of Ca by water vapor, R_{Ca} can be obtained from the mass transport rate of water vapor (R_w) as,

$$R_{Ca} = R_w \left(\frac{M_{Ca}}{M_w} \right) \frac{1}{n} \quad (2)$$

where M_w is the molecular weight of water vapor, M_{Ca} is the atomic mass of Ca, and n is the reaction ratio of Ca to water vapor (2). For thin Ca sensor relative to the length and width (nm as compared to mm), Ca is assumed to be oxidized from the top homogeneously such that,

$$R_{Ca} = A_{Ca} \delta \frac{dh}{dt} \quad (3)$$

where A_{Ca} is the total area of Ca sensor, δ is the density of Ca (1.55 gcm^{-3}), h is the Ca thickness, and t is oxidation time of Ca. Combining equation (1) to (3), WVTR is calculated to

$$\text{WVTR} = n \delta \left(\frac{A_{Ca}}{A_f} \right) \left(\frac{M_w}{M_{Ca}} \right) \frac{dh}{dt} \quad (4)$$

The change of height of Ca sensor according to time ($\frac{dh}{dt}$) can be calculated from the Ca sensor resistance with width (w), length (l), and Ca volume resistivity (ρ_{Ca}), $R = \frac{\rho_{Ca} l}{wh}$, as following,

$$\frac{dh}{dt} = \frac{\rho_{Ca} l}{w} \left(\frac{d(1/R)}{dt} \right) \quad (5)$$

Combining equation (4) to (5) yields

$$\text{WVTR} = n \delta \rho_{Ca} \frac{l}{w} \left(\frac{A_{Ca}}{A_f} \right) \left(\frac{M_w}{M_{Ca}} \right) \left(\frac{d(1/R)}{dt} \right) \quad (6)$$

for WVTR measurement using relation between Ca sensor resistance change and permeation of water vapor through the film. The electrical Ca test has been investigated in numerous researches to measure WVTR for encapsulation materials. Meyer *et al.* investigated encapsulation layers prepared by ALD at low temperature and proved highly efficient permeation barrier characteristic using electrical Ca test (Figure 17) [38]. Nanolaminate with Al_2O_3 and ZrO_2 thin film grown using an ALD reactor showed the permeation rate of $4.7 \times 10^{-5} \text{ g/m}^2/\text{day}$ for water vapor under a controlled environment of 70% humidity and 70°C by electrical Ca test. Owing to amorphous structure, Al_2O_3 and ZrO_2 thin film can be presented

to efficient gas-diffusion barrier. In addition, the nanolaminate structure with repeating Al_2O_3 and ZrO_2 thin film have been demonstrated to provide a very low defect density statistically compared to a single Al_2O_3 layer, showing effective strategy for thin film encapsulation of organic electronic devices.

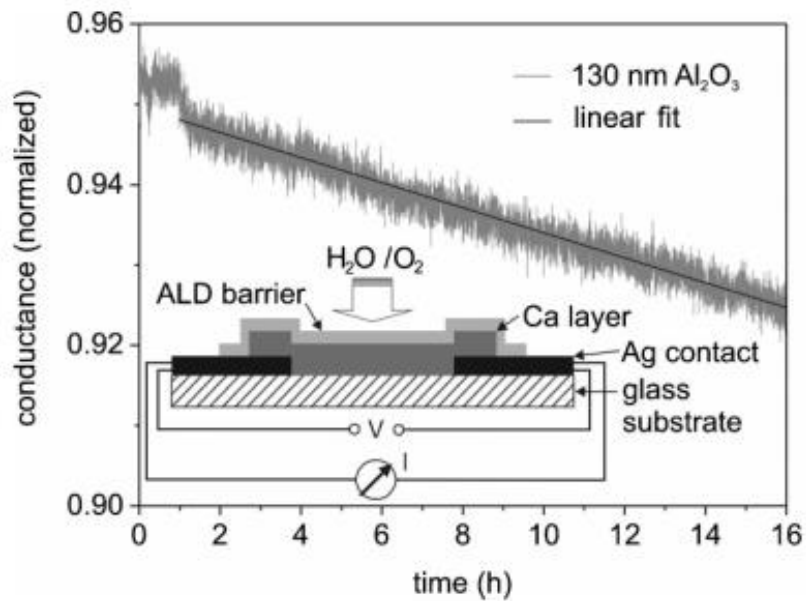


Figure 17. Normalized conductance versus time for a Ca sensor sealed with a 130 nm-thick Al_2O_3 layer grown by ALD process at 80°C [38].

Chapter 3. Enhanced mechanical properties of nanolaminate with metallic glass and graphene

3.1 Materials

3.1.1 Fabrication of metallic glass thin film by sputtering

Several methods, such as electroless plating, melt spinning, arc-melting, and physical vapor deposition have been proposed to fabricate metallic glasses. Among them, magnetron sputtering, kinds of physical vapor deposition method, shows the many merits over others for widely controllable alloy component and adjustable composition and thickness. In this study, metallic glass thin film in the system of Cu-Zr were prepared by two single target, pure Cu and pure Zr.

Monolithic 360 nm-thick $\text{Cu}_{50}\text{Zr}_{50}$ metallic glass was deposited by co-sputtering at room temperature. $\text{Cu}_{50}\text{Zr}_{50}$ metallic glass was deposited on Si (100) substrate by co-sputtering with two separated pure Cu and Zr targets. We used RF power of 23 W for Cu and 50 W for Zr at base pressure of 5×10^{-6} Torr and working pressure of 3 mTorr under Ar environment, which results in deposition of $\text{Cu}_{50}\text{Zr}_{50}$ metallic glass at a rate of 0.12 nm/s. As shown in Figure 18. The chemical composition of the $\text{Cu}_{50}\text{Zr}_{50}$ metallic glass was measured by energy-dispersive X-ray spectroscopy and the amorphous phase was confirmed by transition electron microscopy.

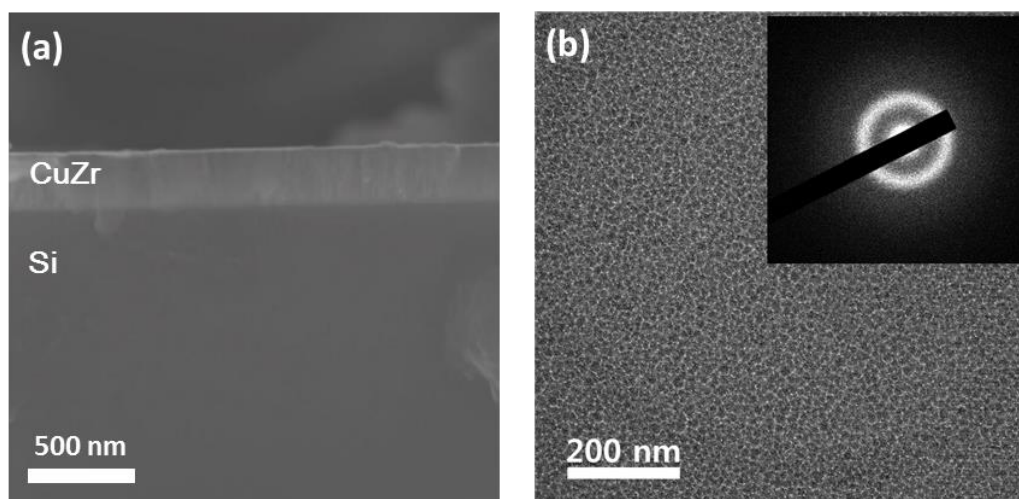


Figure 18. (a) SEM image of cross section of metallic glass deposited on Si substrate. (b) TEM image of $\text{Cu}_{50}\text{Zr}_{50}$ metallic glass showing amorphous structure.

3.1.2 Graphene by chemical vapor deposition (CVD)

Graphene is a single layer of carbon atoms and has hexagonal lattice. Although it is only one-atomic layer, it has many remarkable properties, intrinsic strength of 130 GPa and elastic modulus of 1 TPa [39] [40], as well as heat and electricity efficient [41], carrier mobility [42] [43], and transparency. On account of these noticeable mechanical properties, many studies have been aimed at utilizing graphene as an interfacial material or surface coating material such as interlayer in composites, corrosion barrier, and lubricant materials [44] [45] [46]. In this study, graphene was synthesized on a 25 μm -thick Cu foil and 2-mm-thick single-crystalline Cu substrate by CVD process.

For the graphene synthesis on Cu crystal, the surface of the (111)-orientation single-crystalline Cu was prepared by mechanical polishing with a 0.25 μm colloidal silica suspension and electro-polishing in phosphoric acid (85% H_3PO_4) for 2 min. Before the CVD process, the Cu surface was treated with H_2 gas at 1000 $^\circ\text{C}$ at a base pressure of 4 mTorr. Graphene was synthesized under a flow of CH_4 and H_2 gas for 4 minutes, and the furnace was cooled to room temperature under a flow of Ar gas. We used Raman spectroscopy mapping to confirm the quality and uniformity of CVD-grown graphene on the Cu substrate. Samples for Raman spectroscopy were prepared by transfer of graphene on a SiO_2 substrate. The graphene was transferred on SiO_2 substrate for Raman spectroscopy measurements because the ratio of peak intensities depends on substrate and the ratio of 2D/G peak intensities of monolayered graphene is known to be approximately 2 for SiO_2 substrate.

For graphene synthesis on Cu foil substrate, the as-received Cu foil was treated with acetic acid for 1 hour to remove native oxide layer at the surface, followed by rinsing with DI water and acetone and blow-drying with N_2 gas. Oxide-free Cu foil was then loaded into the CVD chamber and the chamber was pumped down to 2.5×10^{-4} Torr. The Cu foil was maintained at 1050 $^\circ\text{C}$ in H_2 flow for 2 hours, and CH_4 gas was introduced into the chamber for graphene synthesis. The as-grown substrate was rapidly cooled to room temperature by sliding the hot zone of the furnace.

3.1.3 Synthesis of nanolaminate with metallic glass and graphene

Monolithic $\text{Cu}_{50}\text{Zr}_{50}$ metallic glass film with thickness of 360 nm and nanolaminates with metallic glass and graphene were prepared as in Figure 19. Nanolaminates with alternating layers of $\text{Cu}_{50}\text{Zr}_{50}$ metallic glass and CVD-grown graphene was fabricated by repeated deposition of a 60nm-thick $\text{Cu}_{50}\text{Zr}_{50}$ metallic glass layer and graphene transfer process, resulting in six 60 nm-thick metallic glass layers and five graphene layers between them. First, metallic glass layer is deposited on Si substrate by co-sputtering method. The composition and amorphous structure of metallic glass was confirmed using energy dispersive spectrometry and transmission electron microscopy analysis, respectively. Then, CVD-grown graphene was transferred onto a $\text{Cu}_{50}\text{Zr}_{50}$ metallic glass layer by PMMA-assisted wet transfer method. We confirmed graphene films transferred onto metallic glass thin film by Raman spectroscopy. To free-standing film Si substrate is etched using XeF_2 gas and dog-bone shaped tensile sample is patterned using FIB milling method. This patterned tensile sample is transferred onto P-to-P device using Omniprobe manipulator for in-situ tensile testing. Both ends of tensile samples were gripped by ion-beam assisted Pt deposition. Then, tensile test was performed using Picoindenter with diamond flat punch tip.

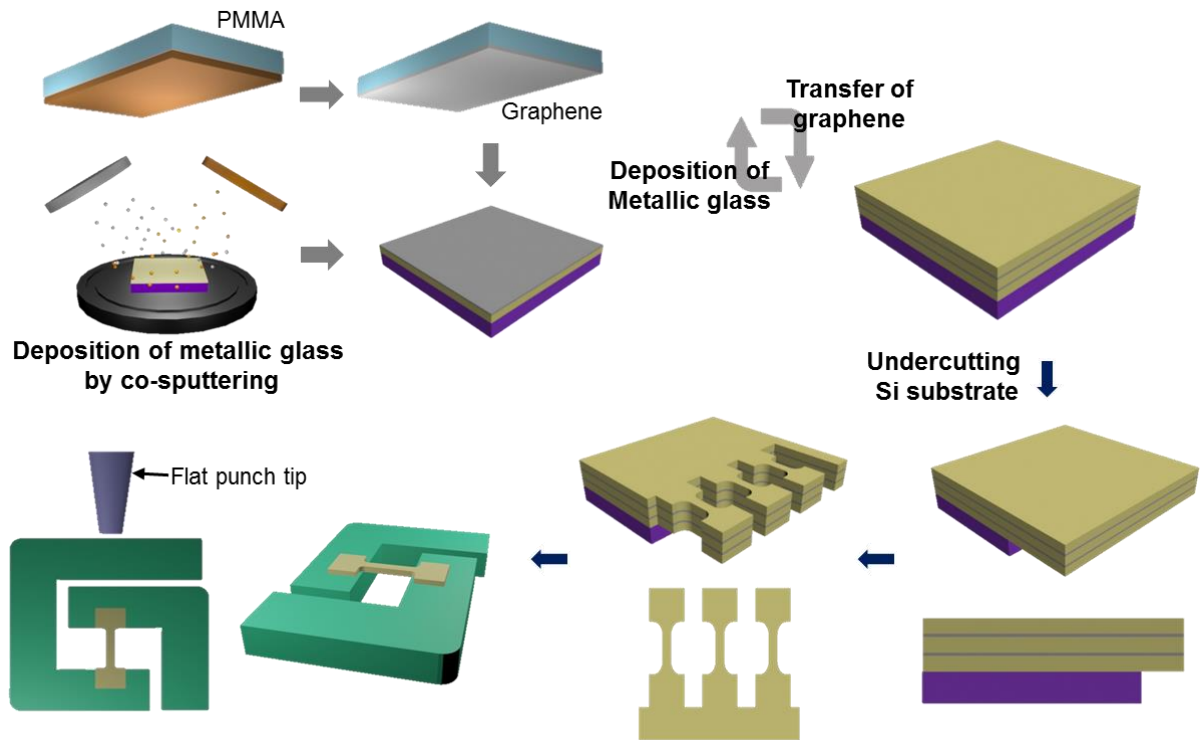


Figure 19. Schematic of fabrication of nanolaminate with alternating layers of $\text{Cu}_{50}\text{Zr}_{50}$ metallic glass and graphene and sample for in situ SEM micro-tensile testing [47].

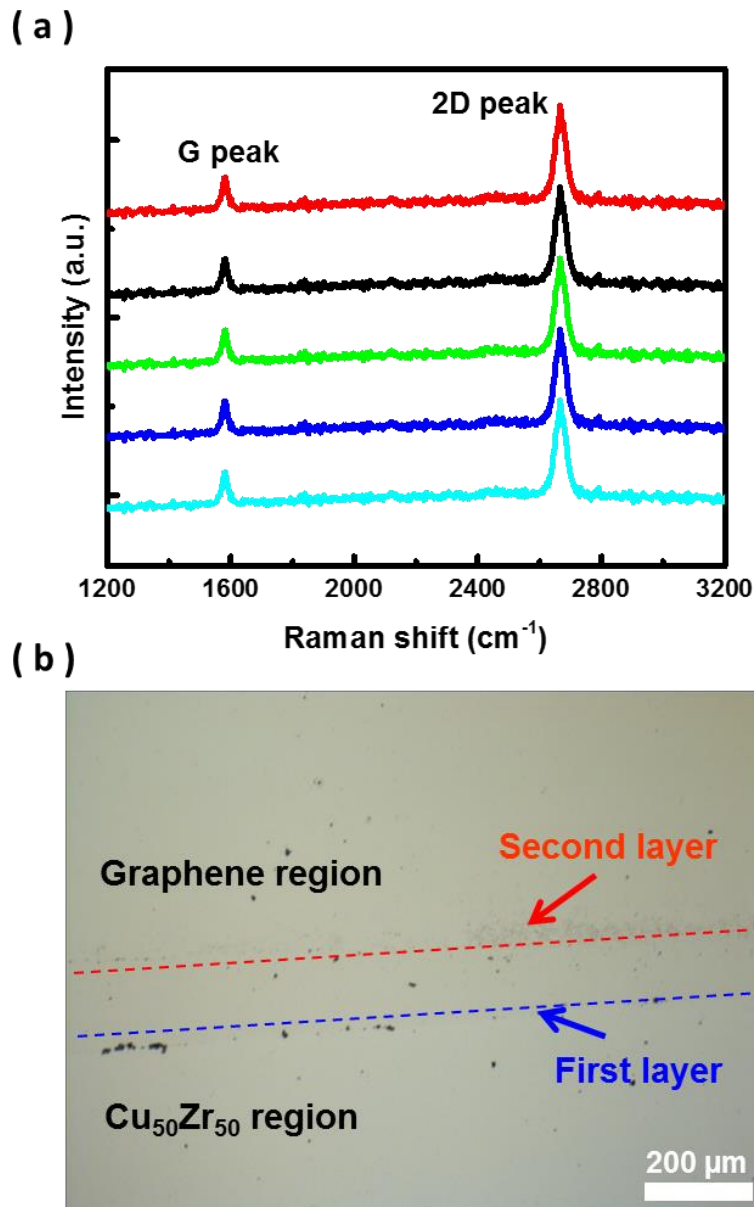


Figure 20. (a) Raman spectra showing typical features of monolayer graphene. (b) The morphology of graphene transferred on Cu₅₀Zr₅₀ metallic glass.

As shown in Figure 20, Raman spectra show that ratios of 2D/G are about 2 for entire area, meaning that monolayer graphene is transferred for most of the area. Optical micrograph image in Figure 20(b) shows graphene films transferred onto metallic glass thin film by PMMA-assisted transfer method.

Figure 21 shows the freestanding films of monolithic metallic glass and nanolaminate prepared by undercutting Si substrate by isotropic dry-etching using XeF₂ gas. Micro-tensile samples in dog-bone shape with dimensions of 1 μm gauge width × 4 μm gauge length were prepared by focused ion beam (FIB) (FEI Quanta 3D) milling. Micro-tensile samples were transferred onto push-to-pull (P-to-P) devices (provided by Hysitron) using an Omniprobe micromanipulator for in-situ SEM micro-tensile testing. Both ends of the micro-tensile sample were gripped by ion-beam assisted platinum (Pt) deposition.

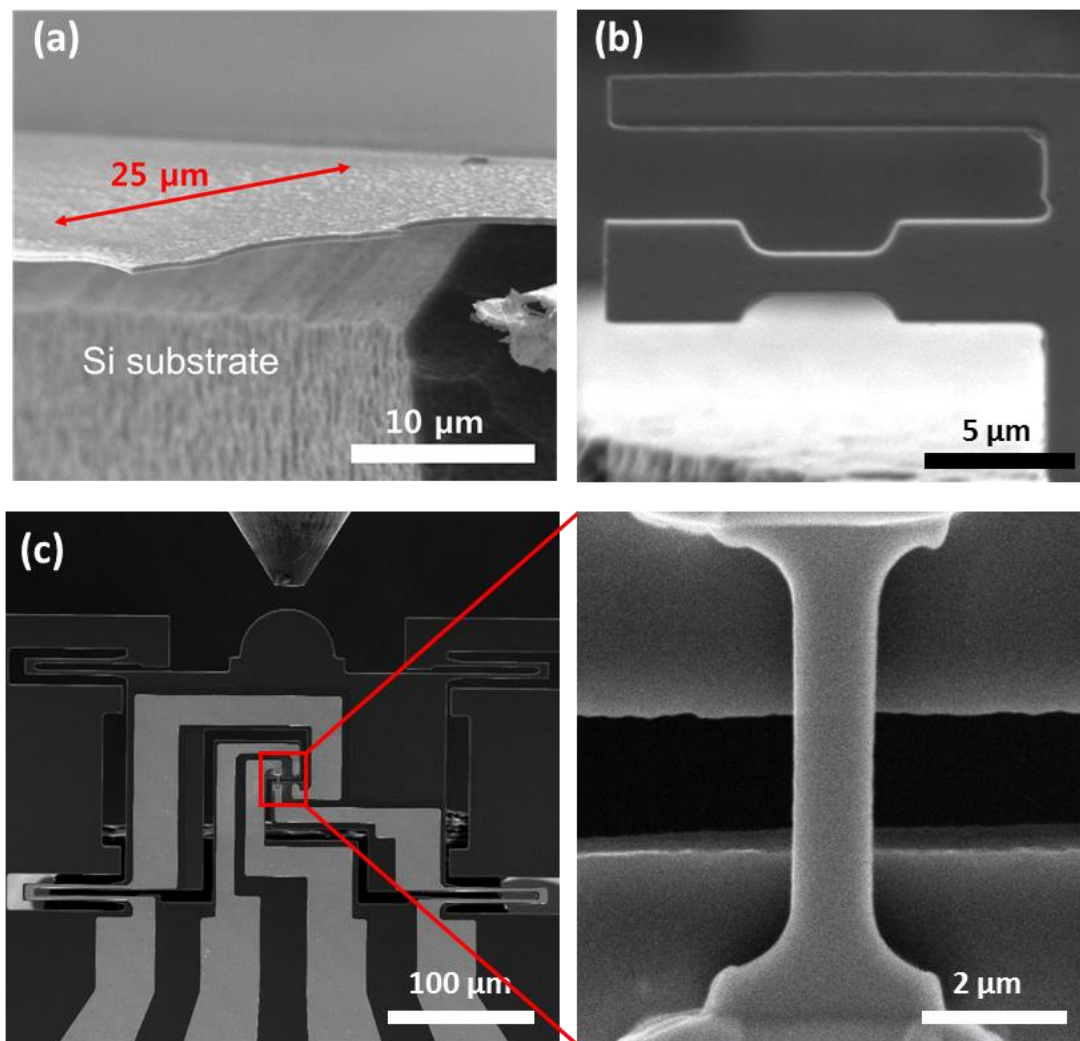


Figure 21. (a) SEM image of freestanding film by etched Si substrate using XeF₂ gas. (b) Dog-bone shaped tensile sample fabricated by FIB milling. (c) P-to-P device transferred FIB-patterned tensile sample for in situ tensile testing. Inset is magnified images of tensile sample.

3.2 Mechanical deformation by graphene coating

In this study, the contact behavior during nanoindentation of graphene-coated Cu is investigated; the initial elastic contact region, the transition region from elastic to plastic deformation, and the fully plastic contact region are analyzed. Nanoindentations were carried out on two samples, graphene-coated Cu (hereafter referred to as Gr-coated Cu), and pristine Cu (hereafter referred to as Gr-removed Cu). The Gr-removed Cu was prepared by physical removal of graphene from the Gr-coated Cu by using adhesive tape. We measured Raman spectroscopy for area of $10\ \mu\text{m} \times 10\ \mu\text{m}$ at several different locations, no G and 2D peaks were observed indicating graphene was removed completely by adhesive tape. Nanoindentations were conducted using the continuous stiffness measurement (CSM) mode of Nanoindenter G200 (Keysight) with a diamond Berkovich indenter, to a maximum indentation depth of 100 nm at a constant strain rate of $0.05\ \text{s}^{-1}$. At least 20 reproducible nanoindentation force–depth curves were obtained for each sample.

Figure 22(a) shows that the 2D/G peak intensity ratio from Raman spectroscopy is approximately two for the mapping area, which is a typical feature of monolayer graphene [48]. Single-crystalline Cu with a (111)-orientation surface was found to have a polycrystalline surface after the CVD process, as shown in the electron backscatter diffraction (EBSD) image in Figure 22(b). This polycrystallization is likely to be attributable to the dynamic nature of the Cu surface, due to sublimation and surface pre-melting, during the CVD process [49] [50]. We carried out nanoindentations on surfaces with root mean squares of surface roughness R_q lower than 2 nm [51] [52], shown in yellow in the EBSD inverse pole figure map in Figure 22(b). This surface has a misorientation angle of 23° with respect to the (100) direction of Cu. Nanoindentations for both Gr-coated and Gr-removed samples were carried out only for the surface with this crystallographic orientation for comparison.

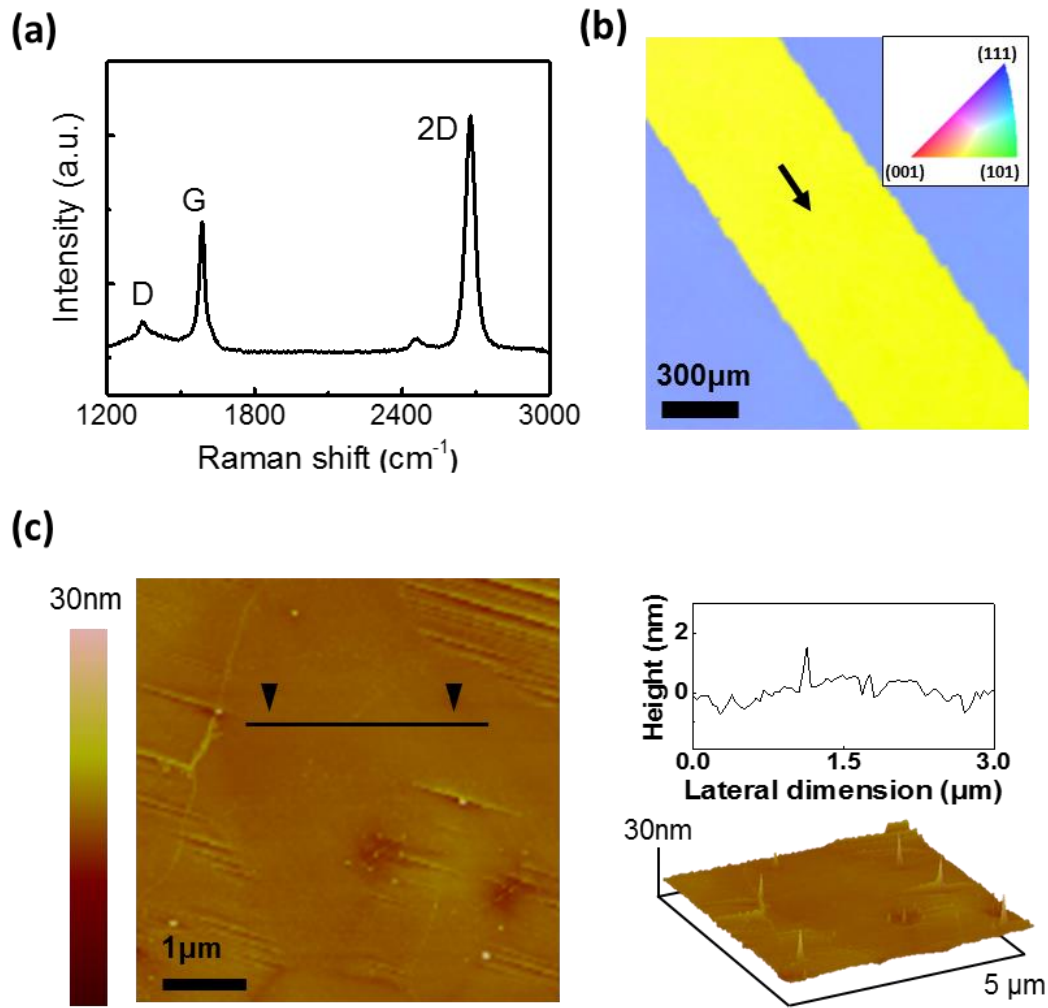


Figure 22. (a) Typical Raman spectra of CVD-grown graphene. (b) Typical EBSD and (c) AFM images of graphene-coated Cu. In yellow surfaces indicated as black arrow, nanoindentations were carried out [53].

Figure 23 show typical nanoindentation force–depth curves and the average force at every 10 nm of nanoindentation depth for Gr-coated and Gr-removed Cu. These figures show that We investigate how the graphene layer affects contact behavior in (1) initial contact region, and (2) fully plastic contact region in following parts.

To investigate the effect of the graphene layer on the initial elastic contact behavior during nanoindentation, typical nanoindentation force–depth curves and the distribution of indentation depth at first pop-in event are presented in Figure 23(c) and 23(d), respectively. Figure 23(c) is the enlarged graphs of Figure 23(a) showing initial elastic loading and pop-in events better. In Figure 23(c), Gr-coated Cu shows slightly stiffer loading than that of Gr-removed Cu. The initial elastic contact during nanoindentation can be described by the Hertzian contact theory for purely elastic contact of a sphere on flat surface, which is given by [54] [55]

$$F = \frac{4}{3}E^*\sqrt{R}h^{1.5}, \quad (7)$$

where F is the indentation force, E^* is the reduced elastic modulus, R is the radius of the indenter, and h is the indentation depth. Before the first pop-in event, for $R = 50$ nm (measured by observing side views of the nanoindenter in SEM), the reduced elastic moduli of Gr-removed and Gr-coated Cu were determined as 158.6 ± 17.8 GPa and 170.2 ± 17.0 GPa, respectively. In reduced elastic modulus, effect of elastic deformation of diamond indenter is included. By applying the relation,

$$1/E^* = (1-\nu_i^2)/E_i + (1-\nu_{mat}^2)/E_{mat}, \quad (8)$$

with E_i of 1141 GPa and ν_i of 0.07 for diamond indenter, elastic modulus of target materials can be evaluated. The elastic modulus is 163.4 ± 22.8 GPa for Gr-removed Cu and 176.7 ± 20.8 GPa for Gr-coated Cu, respectively. The graphene layer, with its ultra-high elastic modulus of 1 TPa, is likely to enhance the elastic moduli only for indentation depths up to the first pop-in event (about 10 nm). Another possible reason for different stiffness is that residual stresses are induced in Cu by the lattice mismatch between graphene and Cu [56]. The stiffer loading curve in Gr-coated Cu could be caused by compressive in-plane residual stresses in the Cu substrate, because compressive in-plane stresses act to “push” the indenter, resulting in a stiffer nanoindentation loading curve [57].

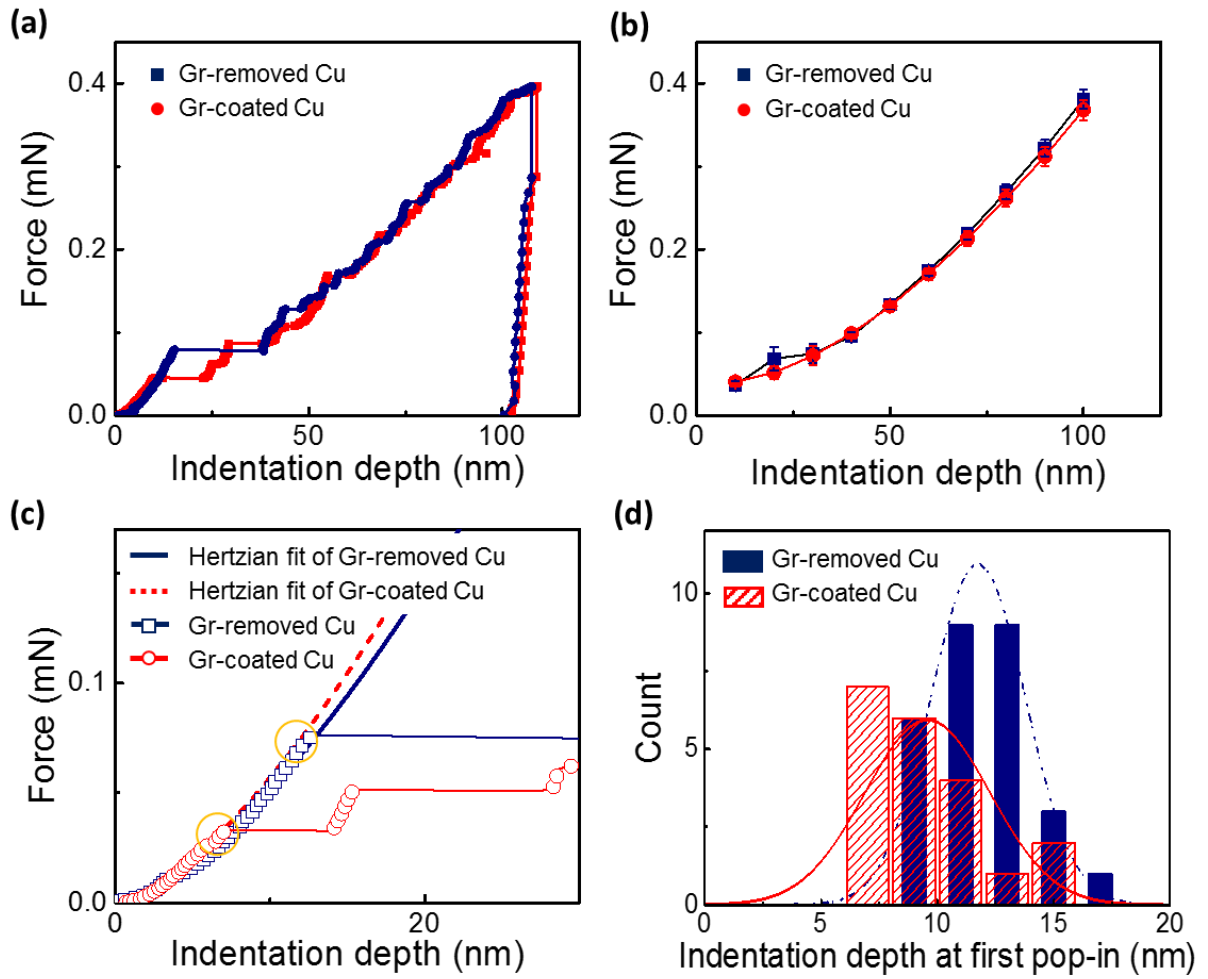


Figure 23. (a) Typical and (b) averaged nanoindentation force-depth curves of graphene-coated Cu and graphene-removed Cu. (c) Typical nanoindentation force-indentation depth curves magnified for initial contact area. Dotted lines are Hertzian equations fitted to loading curves. (d) Histograms of indentation depth at first pop-in event of graphene-coated and graphene-removed Cu [53].

In previous MD simulations, the compressive in-plane stress in Cu was found to decrease the critical indentation depth at which incipient plasticity occurs, whereas tensile stresses do not affect the critical indentation depth [58]. Atom clusters with severe lattice distortions, which are regarded as precursors for the nucleation of dislocations, were formed beneath the indenter before the critical

indentation depth due to shear stress. At the critical indentation depth, the shear stress applied on these clusters exceeds the critical resolved shear stress, and thus, dislocations nucleate, extending on {111} slip planes. The critical indentation depth corresponds to the indentation depth at the first pop-in event. Figure 23(d) shows a histogram of indentation depth at the first pop-in event for all measurements of Gr-removed and Gr-coated Cu.

The indentation depth at the first pop-in event for Gr-coated Cu is shallower than that for Gr-removed Cu, which indicates that compressive in-plane residual stresses might be introduced to the top surface volume of the Cu due to the graphene coating, which agrees with the presumption that compressive stress stiffens the initial elastic loading curves for Gr-coated Cu. The critical resolved shear stress applied on these dislocation precursors, τ_{max} , can be described by [54] [55]

$$\tau_{max} = 0.31 \left(\frac{6FE^{*2}}{\pi^3 R^2} \right)^{1/3}, \quad (9)$$

where F is the indentation force at the indentation depth of the first pop-in event. With an estimated indenter radius $R=50$ nm, the critical resolved shear stress was found to be 15.5 ± 0.98 GPa for Gr-removed Cu and 14.4 ± 1.11 GPa for Gr-coated Cu. The difference in the critical resolved shear stress between the two samples is smaller than for the indentation depths of the first pop-in events, and the values are similar to the theoretical shear strength of Cu (15 GPa) calculated by $\mu_s/2\pi$ [59] [60]. Despite the thickness of graphene (0.34 nm), the graphene coating affects both the initial elastic loading and incipient plasticity as described above, possibly because the graphene layer has an ultra-high elastic modulus and introduces compressive in-plane residual stress in Cu.

We investigate how graphene coating affects the measured mechanical properties for fully plastic contact region at greater indentation depths. The average elastic modulus and hardness at every 10 nm of indentation depth were measured by the Oliver–Pharr method [61] [62], as shown in Figure 24(a) and (b), respectively. The elastic modulus converged for indentation depths deeper than about 60 nm. At the maximum indentation depth (100 nm), an elastic modulus of 117.4 ± 2.3 GPa and hardness of

1.18 ± 0.04 GPa were measured for Gr-removed Cu, and an elastic modulus of 119.3 ± 3.3 GPa and hardness of 1.14 ± 0.04 GPa were measured for Gr-coated Cu. Compared to Gr-removed Cu, there was an increase in elastic modulus of 1.7% and decrease in hardness of 3.2% caused by the graphene coating.

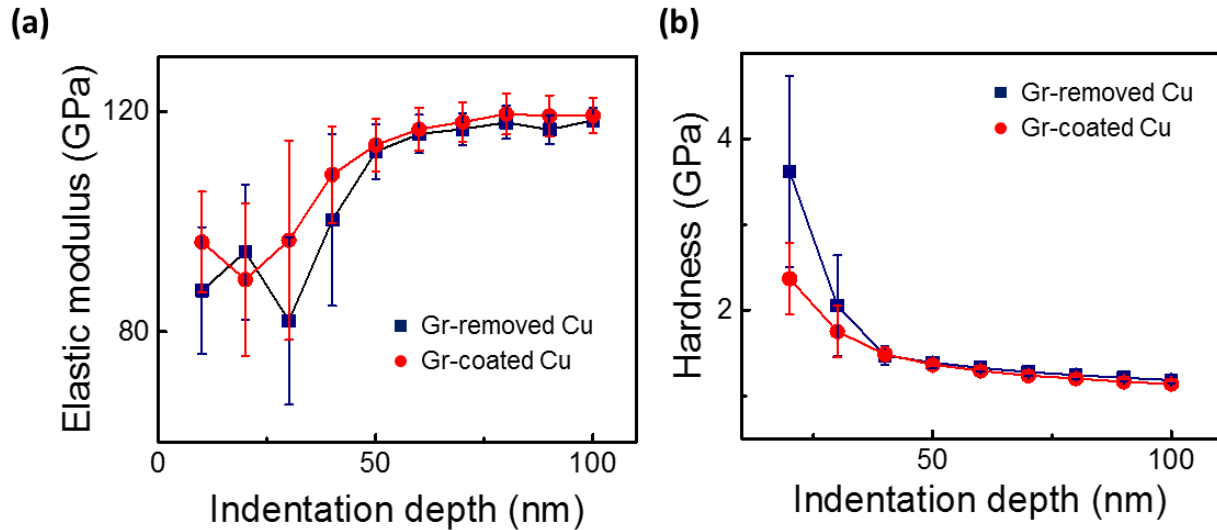


Figure 24. (a) Averaged elastic modulus and (b) hardness of graphene-coated and graphene-removed Cu measured by the Oliver-Pharr method [53].

In ductile metals such as Cu, plastic pile-up generally occurs during nanoindentation, which is not taken into account in the Oliver–Pharr method [62] [63]. By atomic force microscopy (AFM) scanning of residual indentation marks, as shown in Figure 25(a), we found that the graphene coating affects pile-up considerably. Pile-up height was measured as 22.3 (±2.08) nm for Gr-removed Cu and 18.9 (±3.06) nm for Gr-coated Cu, meaning that the graphene coating suppressed pile-up. AFM scanning was carried out for at least 20 residual nanoindentation marks for each sample that were formed with reproducible nanoindentation force-depth curves. The ultra-stiff graphene is likely to suppress the upward stress that would otherwise introduce pile-up in vicinity of the indenter.

Finite element analysis (FEA) was carried out using the commercial package ABAQUS (Simulia) to investigate the stress distribution in Cu during nanoindentation. The specimen was modeled with

four-node axisymmetric reduced integration elements (CAX4R) with an analytical rigid shell of radius $R = 50$ nm for the nanoindenter, and a 0.34nm-thick Gr coating for Gr-coated Cu. The thickness and radius of the specimen were both $2 \mu\text{m}$, which is enough to minimize the boundary effect for 100 nm deep nanoindentations. The material parameters of Cu used for FEA simulations were as follows: elastic modulus $E = 124$ GPa, yield strength $\sigma_y = 46.6$ MPa, ultimate tensile strength $\sigma_u = 217.6$ MPa, and strain-hardening exponent $n = 0.411$ for Cu [64]. $E = 1$ TPa for graphene was used for FEA simulations [41]. Figure 25(b) shows the distribution of the von Mises stresses at the indentation depth of 100 nm in Gr-removed Cu and Gr-coated Cu, as simulated by FEA. The von Mises stress boundary of the Gr-coated Cu near the indenter are more restricted than that of Gr-removed Cu along the in-plane direction, whereas they distribute deeper along the loading direction, as indicated by the orange arrows in Figure 25(b). As shown in the insets of Figure 25(b), this difference in stress distribution results in pile-up heights of 2.30 nm for Gr-coated Cu and 9.23 nm for Gr-removed Cu—the same trend as for AFM measurements. True contact height h_{true} is given by

$$h_{\text{true}} = h_{\text{max}} - h_d + h_{\text{pile-up}}, \quad (10)$$

where h_{max} is the maximum indentation depth, h_d is the elastic deflection depth, and $h_{\text{pile-up}}$ is the pile-up height [61] [65] [66]. By this correction, using the pile-up heights as measured by AFM, an elastic modulus of 98.3 ± 2.7 GPa and hardness of 0.81 ± 0.05 GPa were calculated for Gr-removed Cu, and an elastic modulus of 103.3 ± 2.7 GPa and hardness of 0.82 ± 0.05 GPa were calculated for Gr-coated Cu. This means that the graphene coating enhanced the elastic modulus by 5% and does not significantly change hardness, even in the fully plastic contact region at an indentation depth of 100 nm.

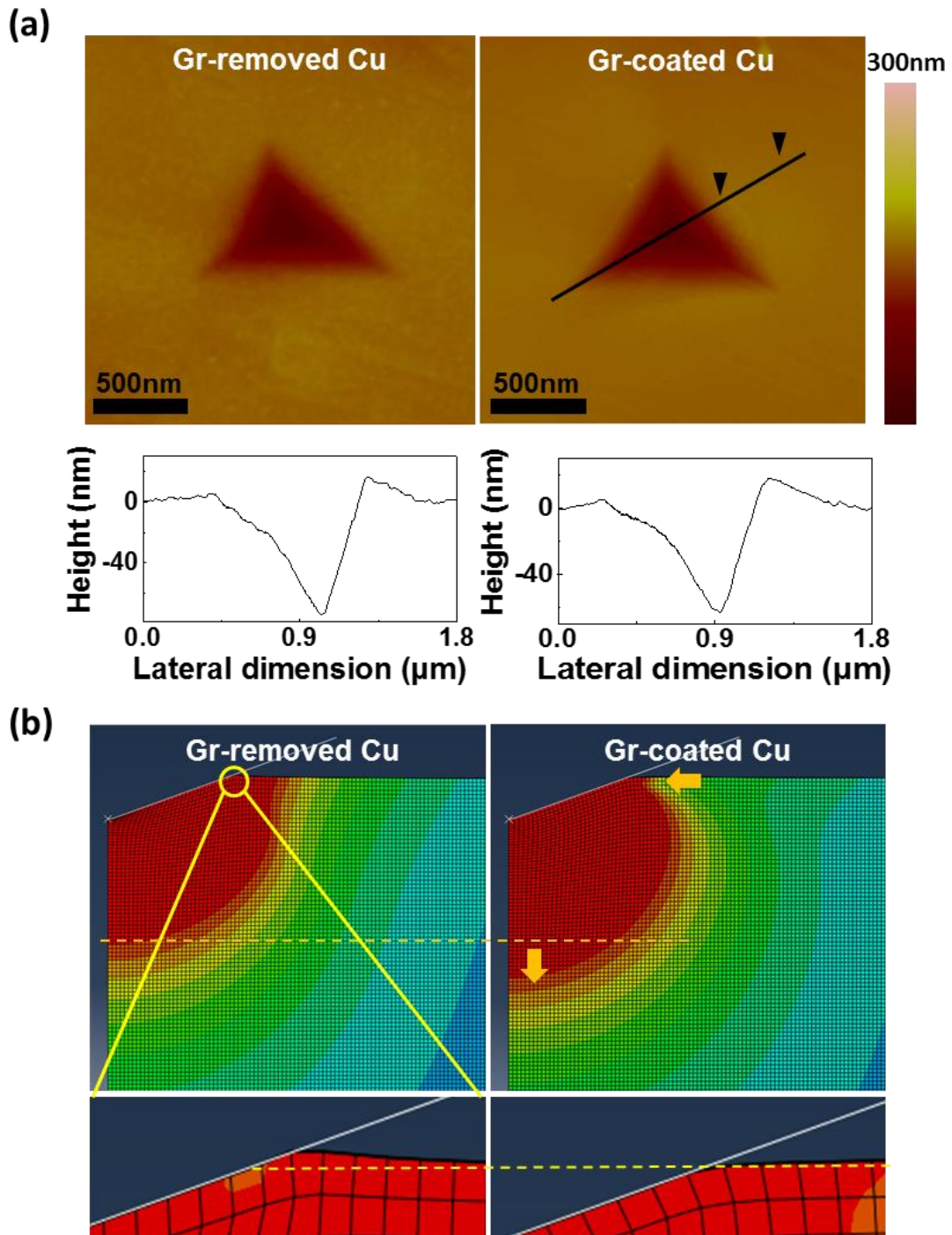


Figure 25. (a) AFM images of residual indentation marks for graphene-removed Cu and graphene-coated Cu. (b) Distributions of von Mises stress in the loaded state analyzed by FEA. Insets show pile-up heights in the loaded state [53].

3.3 Tensile behavior of nanolaminate

3.3.1 Tensile test results of monolithic metallic glass and nanolaminate

In-situ SEM uniaxial micro-tensile tests were performed using Picoindenter (Hysitron PI-87) with a flat punch diamond indenter. Micro-tensile tests were carried out at constant strain rate $1 \times 10^{-3} \text{ s}^{-1}$, and real-time movies were recorded in FE-SEM (FEI Quanta200). The actual force to dog-gone shaped sample was computed by subtracting the estimated force using the spring stiffness of the push-to-pull devices. Initial sample geometry was measured by SEM images and gauge length change was measured by still images extracted from the movie, from which true stress and strain were calculated. We performed in-situ SEM tensile testing and typical stress-strain curves appear in Figure 26(a). Monolithic metallic glass shows typical brittle fracture behavior: linear elastic deformation followed by sudden and catastrophic failure directly after yielding at yield strength of 1.74 (± 0.03) GPa which was measured by 0.2% offset method. Compared to monolithic metallic glass, nanolaminate of metallic glass and graphene shows higher yield strength of 1.98 (± 0.04) GPa and enhanced ductility after yielding, leading to an ultimate tensile strength of 2.23 (± 0.06) GPa and strain from yielding to failure of 1.7%. While monolithic metallic glass shows a typical tensile stress-strain curve with catastrophic failure by shear-band propagation, fracture does not occur by typical shear-off but shows jagged surface normal to loading direction (Figure 26). These may results from the high lateral stiffness of the push-to-pull device used for micro-tensile testing. When semicircular end is pushed using flat punch tip, a sample on the gap in the middle is pulled in tension. It should be pointed out that the lateral stiffness of device is much higher than that of tensile loading as shown in the SEM image. However, this high lateral stiffness of push-to-pull device was affected to suppress sliding and typical shear off process of tensile samples. This high lateral stiffness suppresses sliding and shear-off along one rejuvenated plane by shear-band propagation; instead, fracture seems to occur catastrophically along normal plane to loading direction. This normal fracture in metallic glass has been reported in monolithic La-based metallic glass, and for controlled ratio of normal to shear stresses.

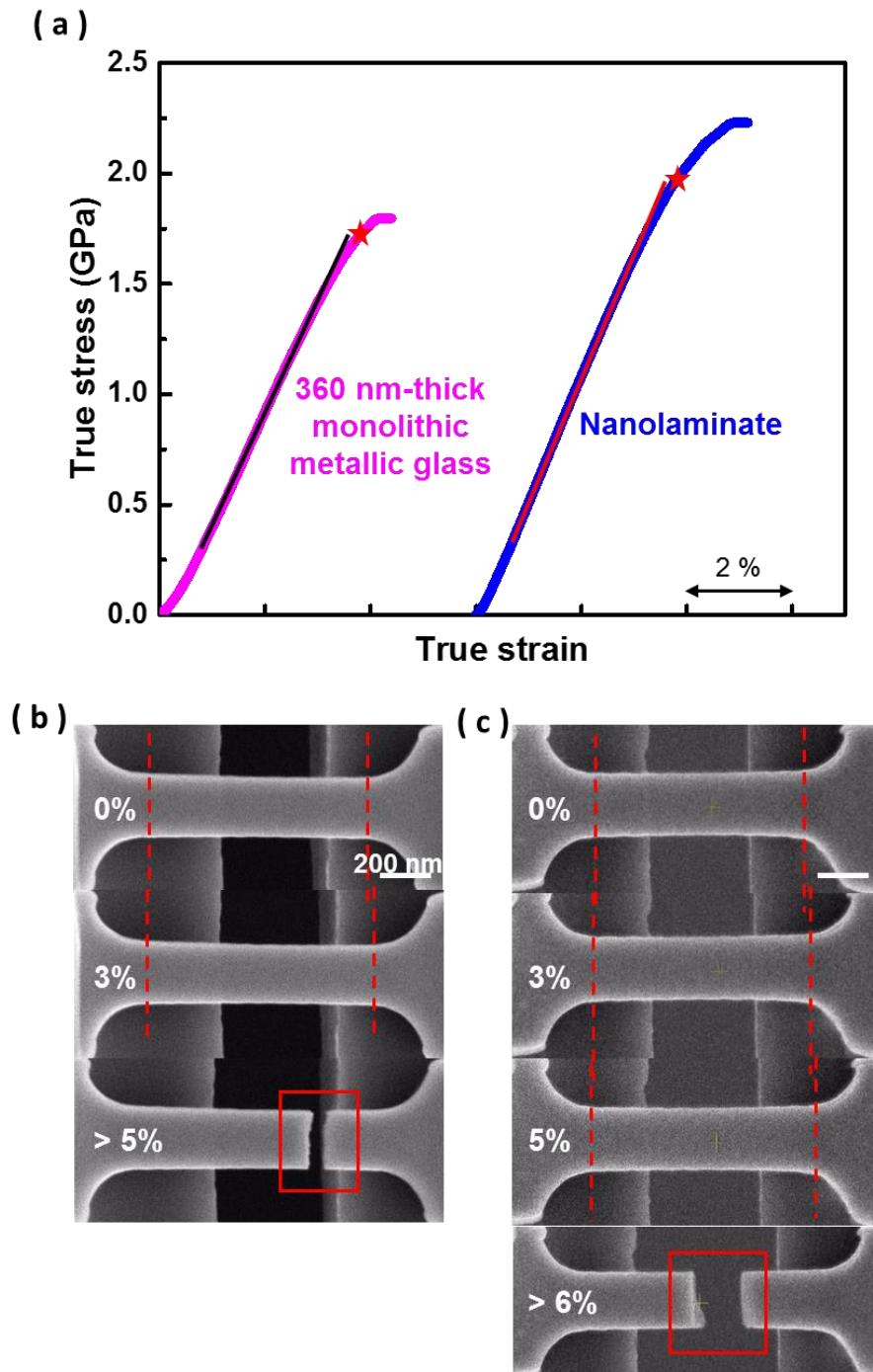


Figure 26. Typical tensile curves of 360 nm-thick monolithic metallic glass and nanolaminate with 60 nm-thick metallic glass and graphene. (a) The true stress-strain curves of monolithic metallic glass and nanolaminate. SEM images during tensile testing of (b) 360-thick monolithic metallic glass and (c) nanolaminate [47].

The tensile stress-strain curve for graphene with perfect atomic configuration investigated by computational simulations show parabolic nonlinear elasticity followed by failure. The elastic modulus, fracture strength and strain deviate slightly depending on loading direction and computational methods, but are approximately 1 TPa, 100 GPa, and 20%, respectively [67]. Elastic modulus of 1 TPa and intrinsic breaking strength of 130 GPa at strain of 25% for single-crystalline graphene were measured through hole-nanoindentations [14]. More recently, fracture strength of 98.5 GPa and elastic modulus of 979 GPa were measured for CVD-grown graphene with grain size of 1~5 μm , and fracture strength of 118 GPa and elastic modulus of 1011 GPa were measured for CVD-grown graphene with grain size of 50~200 μm [39]. These values are in good agreement with those for single-crystalline graphene suggested by computational simulations. CVD-grown graphene used in this study was assumed to have grain size about 10 μm [43]. It is likely that few grain boundaries are included in five graphene layers in the 1 μm \times 4 μm nanolaminate gauge section. Nanolaminates are under iso-strain condition and fracture strain of nanolaminates is 5.39 (\pm 0.32) %, which is much below the fracture strain of graphene. Regardless of graphene grain size, it seems reasonable to assume that graphene as a nanolaminate constituent shows elastic behavior with elastic modulus of 1 TPa up to nanolaminate failure.

Elastic modulus as measured by slope in linear elastic region is 51.0 (\pm 2.14) GPa for monolithic metallic glass and 55.9 (\pm 1.68) GPa for the nanolaminate. Elastic modulus in laminated materials is evaluated by a simple rule-of-mixture when tensile force is applied along the in-plane direction. The rule-of-mixture is applied for six layers of 60-nm-thick metallic glass with elastic modulus 51 GPa and five layers of 0.335 nm-thick graphene with elastic modulus 1 TPa [40], which predicts the nanolaminate elastic modulus as 56 GPa, similar to our measurements. Despite the very low volume graphene fraction in the nanolaminates, 0.46%, the graphene layers enhance the elastic modulus of nanolaminate by 9.6% due to the graphene's ultra-high elastic modulus.

The yield strength of nanolaminate is 14% above that of monolithic metallic glass. Stress applied to constituent materials in laminated materials can be evaluated by a simple rule-of-mixture as well when tensile force is applied along the in-plane direction:

$$\sigma_{Nanolaminate} = \sigma_{MG}V_{MG} + \sigma_{graphene}V_{graphene}, \quad (11)$$

where σ is the stress and V is the volume fraction and subscript MG indicates metallic glass. Using the measured yield strength of nanolaminate, 1.98 GPa, the stress applied at graphene at yield strain of nanolaminate 3.69%, 36.9 GPa as evaluated from elastic modulus of 1 TPa, and the volume fractions mentioned above, the yield strength of metallic glass in nanolaminates is estimated to be 1.81 GPa. This value is slightly above the yield strength of 360 nm-thick monolithic metallic glass, 1.74 GPa. By reduction of external size at sub-100 nm scale, a transition in deformation mode of monolithic metallic glass has been reported from negligible plasticity by shear-band propagation, resulting in catastrophic failure, to enhanced plasticity by homogeneous flow [68] [69]. While the ultimate tensile strength of monolithic metallic glass is enhanced by plastic flow at sub-100 nm scale, their yield strength is not clearly enhanced [68] [70]. In nanolaminates with metallic glass layers thinner than the critical thickness for the transition, yield strength of constituent metallic glass layer is similar to or slightly higher than that for metallic glass layer thicker than the critical thickness.

3.3.2 Homogeneous deformation flow of metallic glass in nanolaminate

Unlike 360 nm-thick monolithic metallic glass, nanolaminate shows enhanced strain-hardening behavior: its ultimate tensile strength of 2.23 GPa is 12.6% greater than its yield strength of 1.98 GPa, and its fracture strain of 5.39 (± 0.32)% is 46% greater than its yield strain of 3.69 (± 0.04)%. Since elastic deformation of monolithic graphene layer is described by parabolic nonlinear elastic deformation behavior up to strains well above the nanolaminate fracture strain, the onset of nonlinearity in the nanolaminates should most probably be attributed to a transition in deformation mode of the metallic glass layers. When designing 60nm-thick metallic glass layers in the nanolaminates, we expected the enhanced plasticity by homogeneous flow that was observed in monolithic metallic glass thickness and metallic glass layers in nanolaminates at sub-100 nm scale. We presumed that enhanced plasticity of nanolaminates is caused by homogeneous flow in 60 nm-thick metallic glass layers. To confirm this presumption, we carried out interrupted micro-tensile testing for nanolaminates as shown in Figure 27.

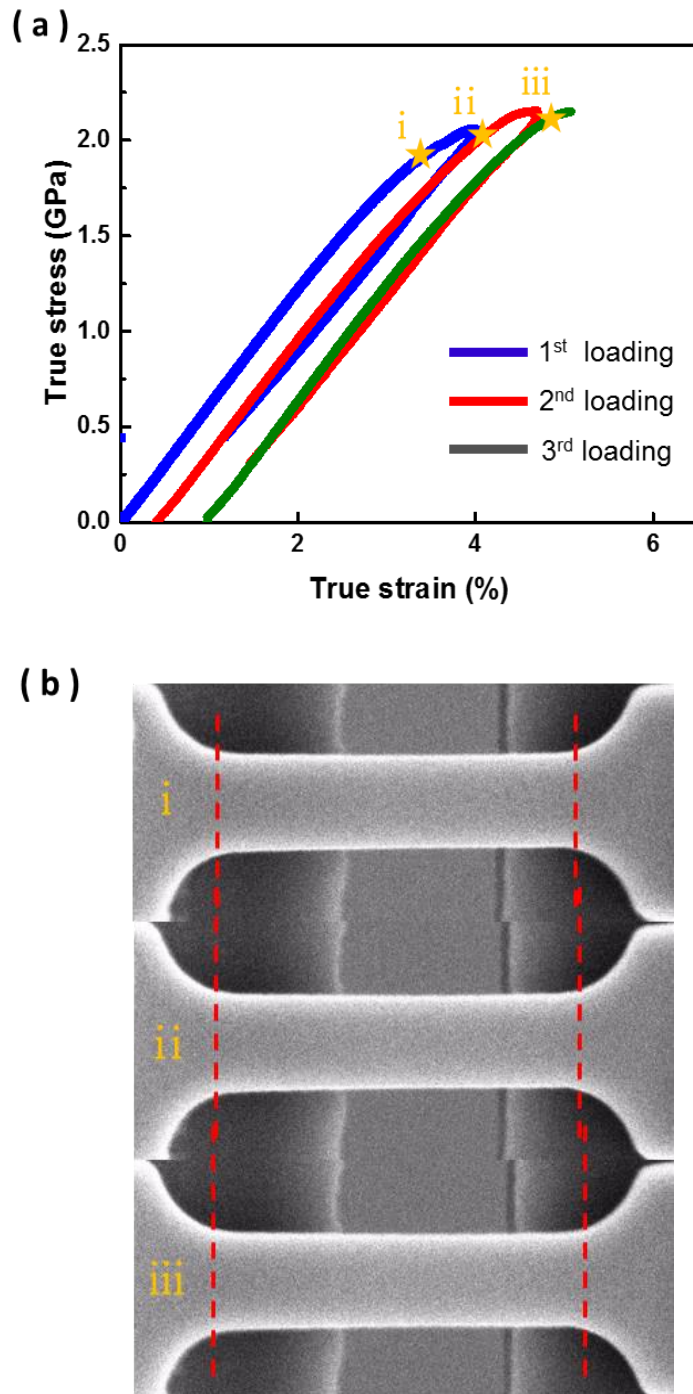


Figure 27. Interrupted in-situ micro-tensile testing for nanolaminate with alternating layers of 60 nm-thick metallic glass and graphene. (a) Yield strength in first, second, and third loading increases gradually, supporting that 60 nm-thick metallic glass layers are strain-hardened by homogeneous flow. (b) Homogeneous deformation is observed during interrupted micro-tensile testing [47].

Possibly because of graphene's nonlinear elastic behavior, the second and third re-loading curves do not show linear elastic behavior up to the peak stress of previous steps. However, the yield strengths in the first, second, and third loading gradually increase to 1.95 (± 0.05), 2.02 (± 0.02), and 2.11 (± 0.02) GPa, respectively. This should be attributed to strain-hardening of the nanolaminates' metallic glass layers. The fracture surface of nanolaminates (Figure 27) is similar to that of 360 nm-thick monolithic metallic glass, indicating that 60 nm-thick metallic glass layers undergo catastrophic failure after some plasticity by homogeneous flow. Stress-strain curves (Figure 27) show that the graphene layer does not act as an obstacle to shear band propagation, leading to catastrophic failure of nanolaminates.

Homogeneous flow in metallic glass has been investigated. For bulk metallic glasses, Johnson and Samwer suggested a phenomenological model for temperature-dependent plastic yielding of metallic glass as

$$\frac{\gamma_y}{G} = 0.036 - 0.016 \left(\frac{T}{T_g} \right)^{2/3}, \quad (12)$$

where γ_y is the elastic strain limit in shear, E the elastic modulus, T the temperature, and T_g the glass transition temperature [71]. A modified Johnson-Samwer relation was suggested as

$$\frac{\varepsilon_y}{E} = 0.026 - 0.012 \left(\frac{T}{T_g} \right)^{2/3}, \quad (13)$$

where ε_y is the yield strain with $\varepsilon_y = \gamma_y / (1 + \nu)$ where ν is Poisson's ratio [72]. For $\text{Cu}_{50}\text{Zr}_{50}$ bulk metallic glass, a shear modulus of 31.3 GPa, elastic modulus of 84 GPa, Poisson's ratio of 0.35, and glass transition temperature of 670 K were measured for $\text{Cu}_{50}\text{Zr}_{50}$ bulk metallic glass [73]. Putting these values into the two equations yields that homogeneous flow can occur at uniaxial stress of 1.06 GPa by the Johnson-Samwer relation and uniaxial stress of 2.05 GPa by the modified Johnson-Samwer relation.

The mechanical properties and glass transition temperature of $\text{Cu}_{50}\text{Zr}_{50}$ metallic glass could be different from those for $\text{Cu}_{50}\text{Zr}_{50}$ bulk metallic glass used above because our samples were prepared by co-sputtering leading to different microstructure such as atomic packing density, homogeneity of atomic mixing and so on. However, Johnson-Samwer relation and modified one give insights that $\text{Cu}_{50}\text{Zr}_{50}$ metallic glass can deform by homogeneous flow at lower than or similar to yield strength of 360 nm-thick monolithic $\text{Cu}_{50}\text{Zr}_{50}$ metallic glass, 1.74 GPa that shows catastrophic failure by shear band propagation. Possible maximum strength of metallic glass layer could be theoretical strength. Theoretical strength of $\text{Cu}_{50}\text{Zr}_{50}$ metallic glass layers fabricated by co-sputtering in nanolaminates with alternating layers of $\text{Cu}_{50}\text{Zr}_{50}$ metallic glass and nanocrystalline Cu was evaluated as 2.83 GPa [74]. By taking into consideration of volume fractions of metallic glass and graphene layers, ultimate tensile strength of nanolaminate 2.23 GPa yields that 60 nm-thick metallic glass layers in nanolaminates attain stress required for shear band propagation at 1.98 GPa which is much lower than theoretical strength.

Two stress values, stress required for homogeneous flow and theoretical strength, are independent of external size of metallic glass. However, the stress required for shear-band propagation is most likely to depend on the external size of metallic glass sample. In Griffith's theory, equating energy released by crack propagation proportional to square of external sample size and elastically-stored energy proportional to cube of external sample size gives stress criterion between regions for brittle fracture and homogeneous deformation [68] [75] [72]. By using nanopillar diameter and effective sample radius, stress required for shear band propagation for metallic glass was suggested to increase with decreasing external sample size in the form of exponent function, i.e. $\sigma \propto d^{-m}$ where d is the external sample dimension (Figure 28). Embryonic shear band is known to form at several atomic scale [76] [77]. 'Shear band propagation' indicates development of embryonic shear band to mature shear band propagation which is believed to require higher stress as external sample size decreases. As mentioned above, yield strength of nanolaminates means that metallic glass layers in nanolaminates initiate homogeneous flow at 1.81 GPa. Metallic glass layers in nanolaminates initiate homogeneous flow at yield strength of nanolaminates and show catastrophic failure by shear band propagation at ultimate tensile strength of nanolaminates.

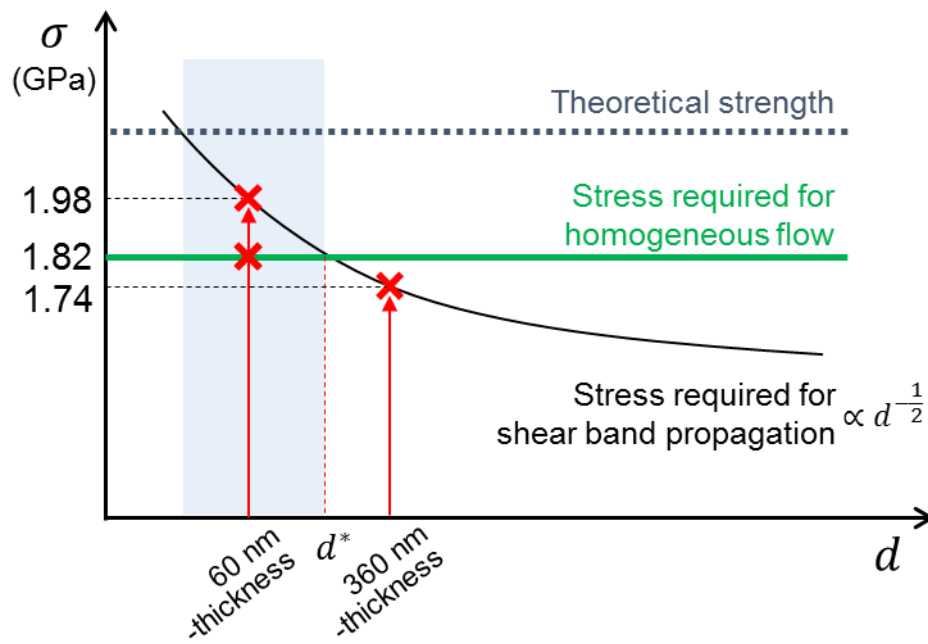


Figure 28. Deformation map of metallic glass in nanolaminate at reduced size.

Chapter 4. Metallic glass thin film for stretchable encapsulation

4.1 Materials

4.1.1 Synthesis of smooth metallic glass thin film by co-sputtering

Metallic glass thin film was prepared by magnetron sputtering technique. It is reported that rapid deposition process and the differences in atomic sizes between Zr and Cu together with the heat of mixing make the Zr-Cu binary system an ideal model for analyzing the glass forming ability. Moreover, the low temperature and easy controllability characteristic of sputtering process can lead to intermetallic alloys in the equilibrium Zr-Cu phase diagram. Since the structure, chemical and phase composition of the film are influenced by sputtering parameter such as power, gas pressure and flow, and deposition rate, condition for fabricating smooth metallic glass thin film is optimized.

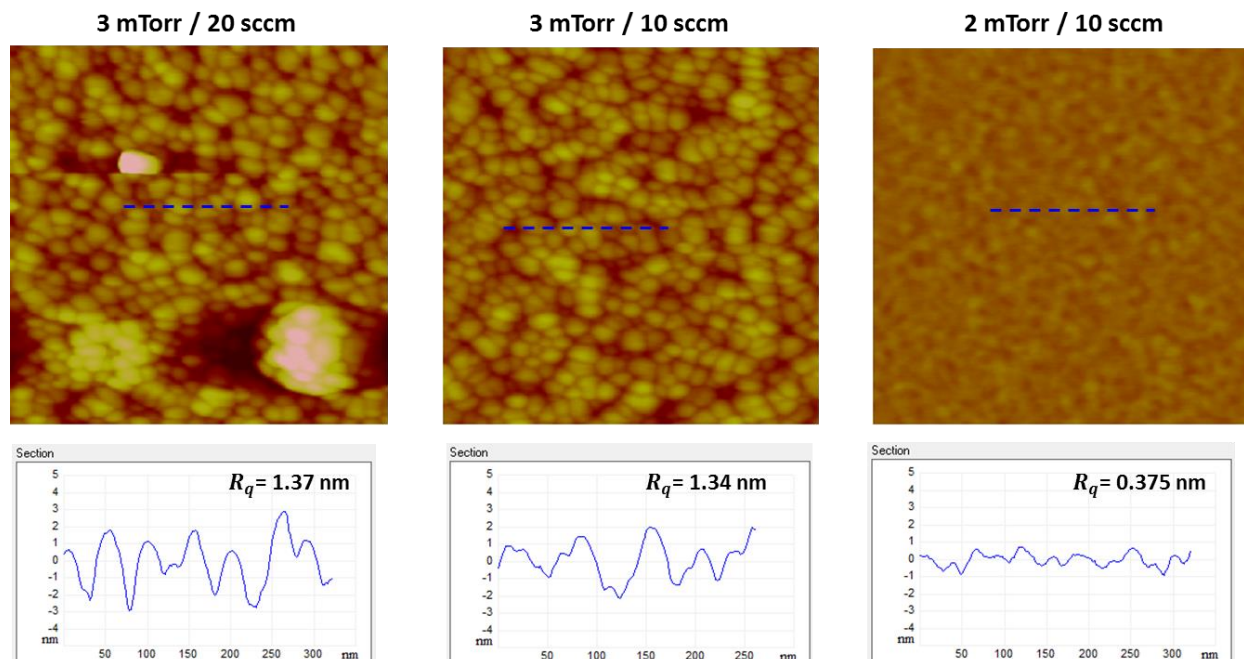


Figure 29. AFM images and profiles of binary metallic glass deposited by sputtering depending on sputtering conditions.

Composition of deposited metallic glass thin film were confirmed using energy dispersive analysis of X-rays. Surface roughness was measured by atomic force microscopy. The scanned area was $10 \times 10 \mu\text{m}^2$ at the scan rate of 1 Hz and averaged value of surface roughness was obtained from ten different position at least.

In order to determine the influence of two parameter, Ar gas flow and working pressure, other parameters for sputtering process were fixed: distance between the target and the substrate ($D=10$ cm), power of each target (4W for Cu and 24W for Zr), and substrate temperature (room temperature, 298K). As shown in Figure 29, morphology of binary metallic glass depends on Ar gas flow and working pressure during sputtering and change from a very rough to a smooth state. AFM measurements revealed that argon gas flow and pressure have the strong influence on the structure of the film. The surface roughness of film is decreased with decreasing argon gas flow and working pressure. Similar results were reported in previous research for both amorphous and crystalline materials. Thornton et al obtained empirically a zone classification of surface morphology upon sputtering condition such as gas pressure and substrate temperature. Recently, Serjey V. K *et al.* showed that preparation of amorphous thin film in two mode, cluster and smooth, is capable by RF magnetron sputtering process [78]. It was found that morphology of the amorphous Ni-Nb thin film was influenced by gas pressure and discharge power and low argon gas pressure and flow decrease the probability for interaction between target atoms with argon gas and formation a smooth thin film is favorable. In this research, metallic glass thin film is synthesized to utilize to stretchable encapsulation material, which required to have the lowest of diffusion path density. Sputtering conditions for synthesize a metallic glass thin film, $\text{Cu}_{39}\text{Zr}_{61}$, with smooth surface are optimized as following: argon gas flow of 10 sccm, working pressure of 1 mtorr, and DC power of 4 W and 24 W for Cu and Zr target, respectively, which results in deposition rate of 6 nm/s on Si substrate.

4.1.2 Fabrication of ternary metallic glass

Multicomponent bulk metallic glasses exhibit remarkable mechanical properties and formable characteristic at high temperature due to enhanced glass forming ability (GFA). Considerable works have been aimed to develop the BMG with excellent GFA. One of the most effective methods to enhance GFA of metallic glass materials is to add new elements to the composition, leading to more complex reaction for crystallization. The key points for the BMG formation include the empirical three rules; multicomponent alloy at least three element, negative heat of mixing between the elements, and over 12% atomic radius mismatch between elements [79] [80]. In this study, binary CuZr metallic glass was chosen as a matrix material, and the effect of the minor addition, Al and Ti element, on the thermal stability was examined. Condition for binary Cu-Zr metallic glass thin film was optimized to fabricate impermeable thin film. Then, based on condition for smooth thin film, four kinds of metallic glass, $\text{Cu}_{57}\text{Zr}_{43}$, $\text{Cu}_{39}\text{Zr}_{61}$, $\text{Cu}_{37}\text{Zr}_{57}\text{Al}_6$, $\text{Cu}_{31}\text{Zr}_{61}\text{Ti}_8$ were deposited by co-sputtering at room temperature. We used both RF and DC power of single target (Cu, Zr, Al, and Ti) at base pressure of 3×10^{-6} Torr and working pressure of 1 mTorr under Ar environment, which results in deposition of metallic glass at a rate of 6 nm/min for all samples. The chemical composition of the metallic glass deposited by sputtering were examined by scanning electron microscopy and energy dispersive analysis of X-rays (Table 2). Surface roughness was confirmed using atomic force microscopy. Surface morphology of metallic glass thin films deposited by co-sputtering is shown in Figure 30.

		Binary		Ternary	
		CuZr		CuZrAl	CuZrTi
Power	Cu (DC)	6 W	4 W	4 W	4 W
	Zr (DC)	18 W	24 W	24 W	30 W
	Al (RF)	-	-	3 W	-
	Ti (RF)	-	-	-	12 W
Atomic ratio		57 : 43	39 : 61	37 : 57 : 6	31 : 61 : 8

Table 2. Sputtering conditions and atomic ratio for binary and ternary metallic glass thin film.

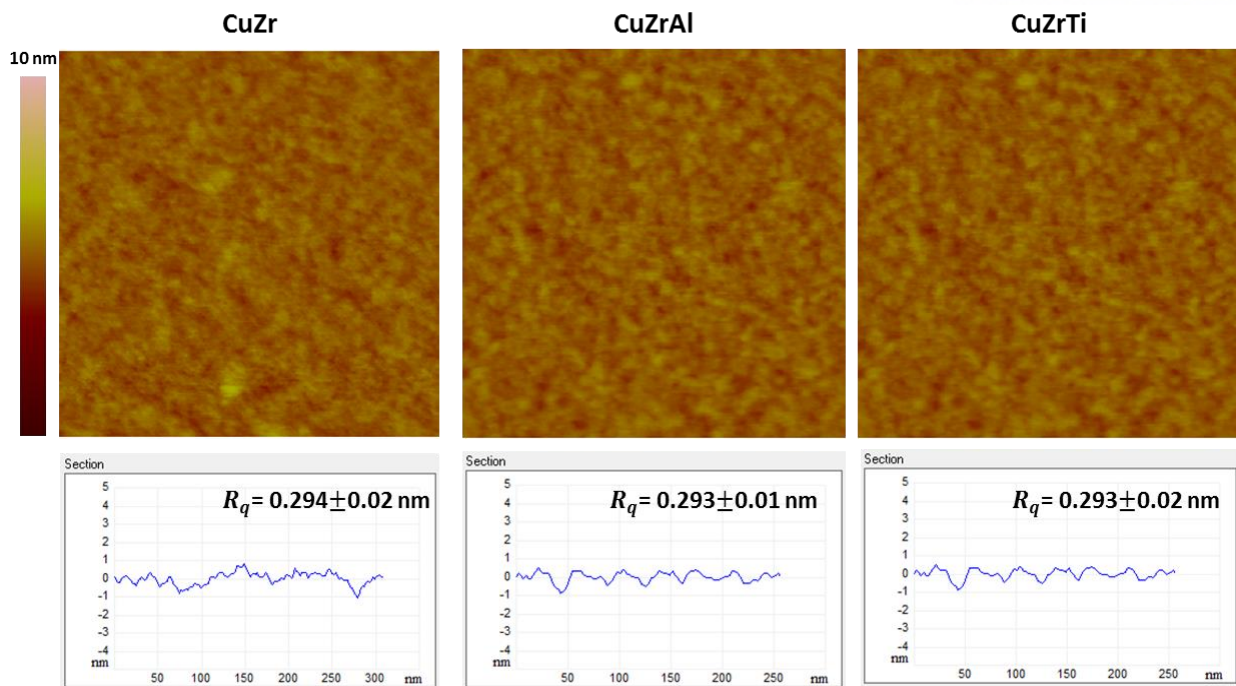


Figure 30. AFM images and profiles showing smooth surface morphology of metallic glass thin films deposited using optimized sputtering condition.

4.1.3 Edge sealing deposited by sputtering process

As well as impermeability, the encapsulation layers must also be able to form a homogeneous structure without local defects acting as paths for water vapor permeation. An optical test was performed using sensitive Ca sensors to address a homogeneous film of metallic glass thin film on large areas and edge sealing from the sputtering process. The 121 Ca pads of 1 mm diameter were deposited on a glass substrate using a thermal evaporator. The glass substrates were subsequently encapsulated with a 260 nm-thick binary and ternary metallic glass thin film using the sputtering process. The encapsulated samples by binary and ternary metallic glass thin film were stored in an environment of 90% relative humidity at 30°C and photographed at regular spaced intervals. The Ca pads encapsulated by binary and ternary metallic glass were corroded and turned to be transparent, meaning a low permeation rate for oxygen and water vapor of ternary metallic glass thin film. For both Ca pads encapsulated by binary and ternary metallic glass film, there is even corrosion in a large area, showing edge sealing capability of the sputtering process.

4.2 Diffusion barrier characteristics of metallic glass thin film

4.2.1 Water vapor transmission rate of metallic glass

WVTR of metallic glass thin film is measured using electrical Ca test. WVTR is water vapor mass per unit area in a day, which is typical indicator for evaluating diffusion barrier characteristic. Schematic of sample preparation for permeation sensor is shown in Figure 31. The sensor consists of 100 nm thick Au electrodes with a spacing of 6 mm. A 10 nm thick Cr layer is used for adhesion layer between glass substrate and Au electrodes. Ca pad was evaporated thermally in between Au electrodes. The width and thickness of the Ca pads are 1 mm and 200 nm, respectively. Then Ca pad was encapsulated by barrier film deposited on PET substrate of 70 μm thickness. A PET/barrier film was attached using epoxy sealant. Barrier films, nanocrystalline copper, binary and ternary metallic glass thin films, are deposited by sputtering. We used DC power for Cu and Zr targets and RF power for Ti and Al targets at base pressure of 5×10^{-6} Torr and working pressure of 1 mTorr under Ar environment, which results in deposition of metallic glasses at a rate of 6 nm/min.

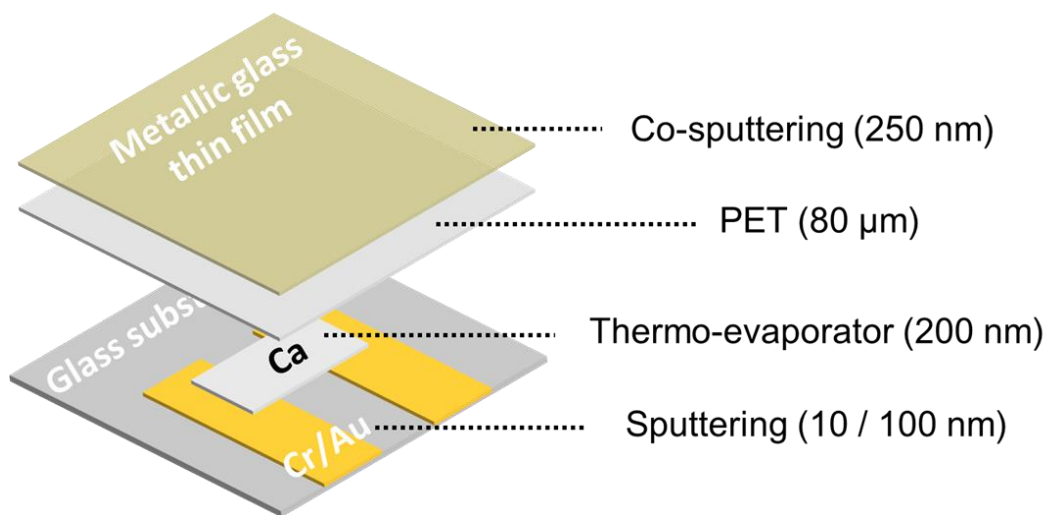


Figure 31. Sample preparation schematic and condition for WVTR measurements.

The WVTR has been investigated under an environment of 90% relative humidity at 30°C in a climatic chamber. WVTR is evaluated by measuring the conductance change of Ca oxidizing by permeated water vapor at constant voltage:

$$\text{WVTR (gm}^2\text{d}^{-1}\text{)} = -n \cdot \left(\frac{M_{\text{water}}}{M_{\text{Ca}}} \right) \cdot \rho_{\text{Ca}} \cdot \sigma \cdot \left[\frac{d(1/R)}{dt} \right], \quad (14)$$

where n is the molar equivalent of the degradation reaction (2), M_{water} is the molecular weight of water (18 gmol^{-1}), M_{Ca} is the molecular weight of calcium (40 gmol^{-1}), ρ_{Ca} is the density of calcium ($1.54 \times 10^6 \text{ gm}^3$), σ is the resistivity of calcium ($3.5 \times 10^{-8} \text{ }\Omega\text{m}$), and $\frac{d(1/R)}{dt}$ is the rate of change in conductance. As shown in Figure 32, in initial region called lag time the conductance does not change, meaning none reaction of Ca pad with water vapor in this region. The transition of slope may be caused by permeated water vapor through metallic glass thin film. Therefore, WVTR is evaluated by linear fitting in this “fall off” region. As a result, WVTR of 260 nm thick binary and ternary metallic glass films were $7.8 \pm 1.5 (\times 10^{-2}) \text{ gm}^{-2}\text{day}^{-1}$ and $6.9 \pm 1.2 (\times 10^{-2}) \text{ gm}^{-2}\text{day}^{-1}$ under an environment of 90% relative humidity at 30°C, respectively, suggesting that they have similar density of atomic structure. WVTR of nanocrystalline copper film was $1.1 \pm 0.6 (\times 10^{-2}) \text{ gm}^{-2}\text{day}^{-1}$, showing the lower permeation rate than metallic glass thin films. This can be attributed to dense structure of nanocrystalline copper film deposited by sputtering. Glass-encapsulated Ca sensor does not change in conductance over time that Ca sensors encapsulated by metallic glass films were oxidized. This behavior verified that measured WVTR are obtained through metallic glass thin film, not through epoxy sealant. By varying the temperature in the climatic chamber, activation energy E_A for the permeation of water through the ternary metallic glass thin film is determined to be 44 kJmol^{-1} for ternary metallic glass thin film (Figure 33). Using the activation energy E_A for the permeation of water vapor, WVTR of ternary metallic glass thin film at room temperature can be determined to $3.4 \pm 1.5 (\times 10^{-3}) \text{ gm}^{-2}\text{day}^{-1}$, showing feasibility for utilizing as stretchable encapsulation for solar cell or thin film transistor devices.

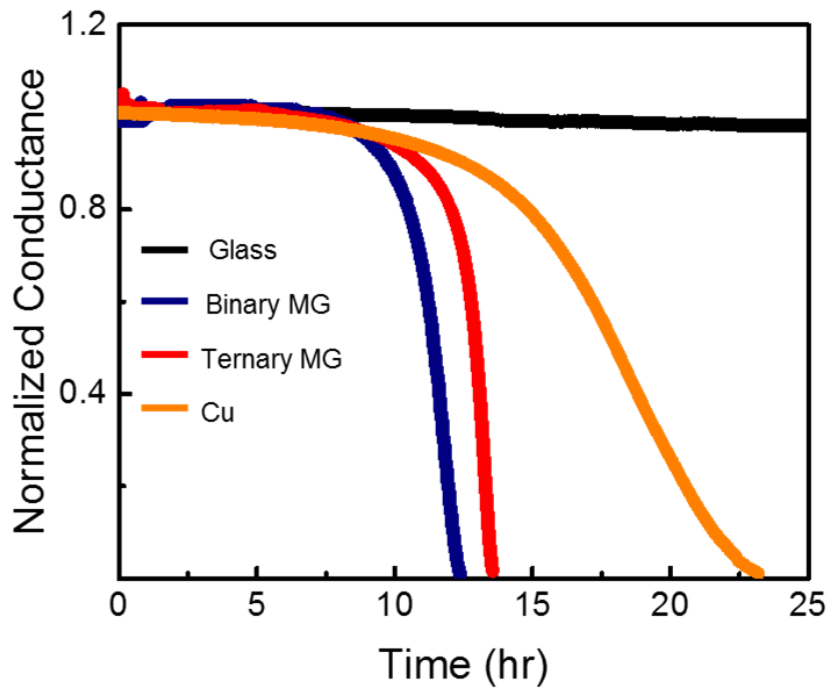


Figure 32. WVTR measurement results of Cu, binary and ternary metallic glass film under environment of environment of 90% relative humidity at 30°C.

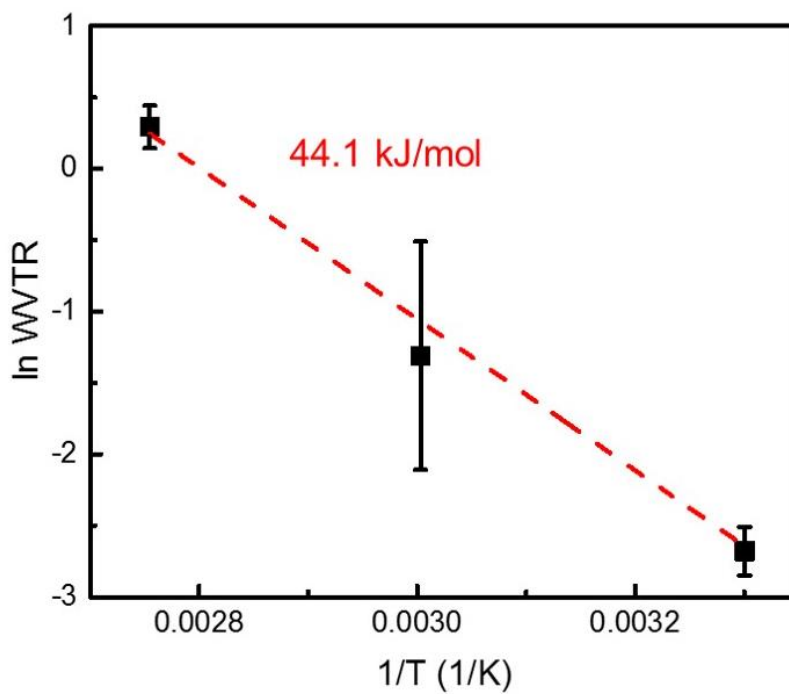


Figure 33. Plot of \ln WVTR versus temperature for water vapor permeation through ternary metallic glass thin film structure.

The accelerating condition increases permeation rate of water and oxygen through the barrier film. The “acceleration” has many kinds of meaning in the reliability, but that term commonly includes making “time” go faster, so that reliability information of lifetime can be obtained rapidly. In this research, to evaluate reliability of metallic glass thin film for encapsulation material relating variables, temperature and humidity, acceleration factor (AF) is investigated using Arrhenius-Peck model. Acceleration factor is the ratio of the characteristic life between the use environment and accelerated test environment, as following:

$$AF = \frac{f(t_2, h_2)}{f(t_1, h_1)}, \quad (15)$$

where $f(t_x, h_y)$ denotes the Arrhenius-Peck’s acceleration model at temperature (t_x) and humidity (h_y), t_1 and h_1 is the temperature and humidity at use environment, and t_2 and h_2 is the temperature and humidity at acceleration environment. Using the Peck’s model defined in equation (15), the acceleration factor is determined by as following:

$$AF = \left(\frac{RH_{accel}}{RH_{use}}\right)^m \cdot e^{\frac{E_a}{R} \cdot \left(\frac{1}{T_{use}} - \frac{1}{T_{accel}}\right)}, \quad (16)$$

where RH is the relative humidity (%), m is the empirical value (-2.66), E_a is the activation energy for permeation of water vapor (44 kJmol⁻¹), R is the gas constant (8.614 Jmol⁻¹K⁻¹), T is the temperature (K), and subscript *use* and *accel* indicates condition of use and acceleration environment, respectively. In this research, acceleration environment is the 85%RH/85°C and use environment is the 40%RH/25°C. The acceleration factor of ternary metallic glass is determined to be 78 using the obtained activation energy E_A for the permeation of water vapor, meaning 1 hour in acceleration environment is equivalent to 78 hours in use environment.

4.2.2 Oxidation mechanism of metallic glass

As well as impermeable properties, encapsulation materials have to be able to maintain diffusion barrier characteristic without structural changes during production process and operating environment of devices, so long-term thermal stability has been verified. The 260 nm-thick metallic glass thin films and nanocrystalline copper film deposited on Si substrate by sputtering were kept in climate chamber of and oxidized for 1000 hours and observed using optical microscope over a period of time. The crystallographic structure and thermal stability of oxidized metallic glass films has been investigated by grazing incidence X-ray diffraction (GIXRD) on a Bruker with a Cu X-ray anode. The scanning range of 2θ is $20-80^\circ$ with a step size of 0.10° . The chemical states and the depth distribution in the oxidized binary and ternary metallic glasses have been investigated by X-ray photoelectron spectroscopy using Al $K\alpha$ radiation ($h\nu=1486.68$ eV and analysis area ~ 400 μm in diameter size).

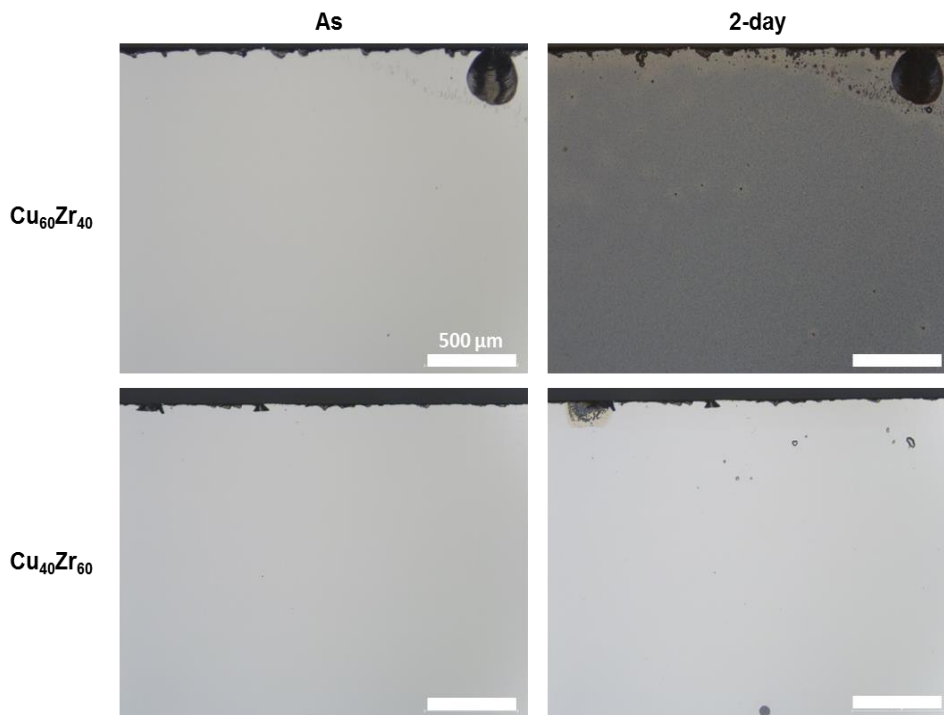


Figure 34. The optical images of as deposited and oxidized for 2 days of binary metallic glass thin films, $\text{Cu}_{60}\text{Zr}_{40}$, $\text{Cu}_{40}\text{Zr}_{60}$, are under an environment of 85% relative humidity at 85°C .

To investigate the effect of oxidation behavior depending on atomic composition, binary metallic glass thin films, $\text{Cu}_{57}\text{Zr}_{43}$, $\text{Cu}_{39}\text{Zr}_{61}$, are compared. The optical images of the as-deposited amorphous $\text{Cu}_{57}\text{Zr}_{43}$ and $\text{Cu}_{39}\text{Zr}_{61}$, as shown in Figure 34, show very smooth and uniform surface morphology. The optical images of binary metallic glass thin films oxidized for 2 days suggest that the oxidation behavior depends on atomic concentration. Surface of $\text{Cu}_{57}\text{Zr}_{43}$ sample exhibits color change on whole area of film, while $\text{Cu}_{39}\text{Zr}_{61}$ sample shows oxidation behavior on partial areas. This homogeneous oxidation behavior of $\text{Cu}_{39}\text{Zr}_{61}$ sample can be attributed from lower crystallization driving force than that of $\text{Cu}_{57}\text{Zr}_{43}$ sample. The crystallization driving force has linear relationship with the difference between the Gibbs free energies of two states, crystalline and amorphous phases. These atomic-concentration-dependent oxidation behavior of metallic glass thin films was investigated by Xu *et al* [81]. They prepared amorphous CuZr alloys over a wide composition range and investigated oxidation behavior using combined experimental approach including scanning electron microscopy, X-ray diffraction, and cross-sectional transmission electron microscopy, to reveal the oxidation mechanism in Cu-Zr alloy system. The amorphous Cu-Zr alloys when atomic concentration of Cu is under 67% shows clear passivation behavior. Amorphous ZrO_2 layer with thickness of about 5 nm forms on the surface of alloy and Cu-enriched region forms below the oxidation layer. With diffusion of oxygen into the alloy, the spherical tetragonal ZrO_2 phase nucleates at between oxide layer and amorphous alloy layer. It can be concluded from the Gibbs driving force of the transition to tetragonal ZrO_2 is determined by the difference between the bulk Gibbs energy and surface energy. Generally, the monoclinic ZrO_2 is more stable than tetragonal ZrO_2 at room temperature due to negative bulk Gibbs energy, but when the diameter of nanocrystal is smaller than critical size the surface energy can overcome the bulk Gibbs energy, leading to a large enough driving force and occurrence of the transition from monoclinic phase to tetragonal phase at room temperature. On the other hand, amorphous Cu_2O layer with thickness of 3 nm are formed on top of the oxidized Cu-Zr alloys with Cu atomic concentration of 75%. This can be attributed from the dominant Cu concentration and rapid diffusion of Cu atoms. Further oxidation forms metallic Cu cluster precipitation in the Cu oxide film layer and below the amorphous Cu_2O layer amorphous ZrO_2 layer with thickness of 8 nm is formed.

The optical microscope images of as-deposited and oxidized nanocrystalline copper film, as shown in Figure 35, oxidation was observed in the whole area with color change in 2 days under an environment of 85% relative humidity at 85°C. The optical microscope images of as-deposited and oxidized binary metallic glass showed that binary metallic glass was partially oxidized under an environment of 85% relative humidity at 85°C. The X-ray diffraction patterns of the oxidized binary metallic glass revealed that oxides such as ZrO_2 , CuO , and Cu_2O were formed on surface after oxidation. In the case of ternary metallic glass, no oxidation was observed through optical microscope and only broad intensity humps in the range of $30-40^\circ$ was observed, confirming the amorphous states of ternary metallic glass after 1000 hours under environment of 85% relative humidity at 85°C (Figure 36). The oxidized binary and ternary metallic glasses have been investigated by XPS depth profiling to verify how the oxidation was appeared according to depth. Figure 37 shows the atomic percent profiling of binary and ternary metallic glasses according to depth. The binary metallic glass exhibits high atomic percent of Zr element as 90% at the surface. Gradually, atomic percent of Zr element decreased and at the depth of about 10-30 nm an increasing atomic percent of Cu element region appeared.

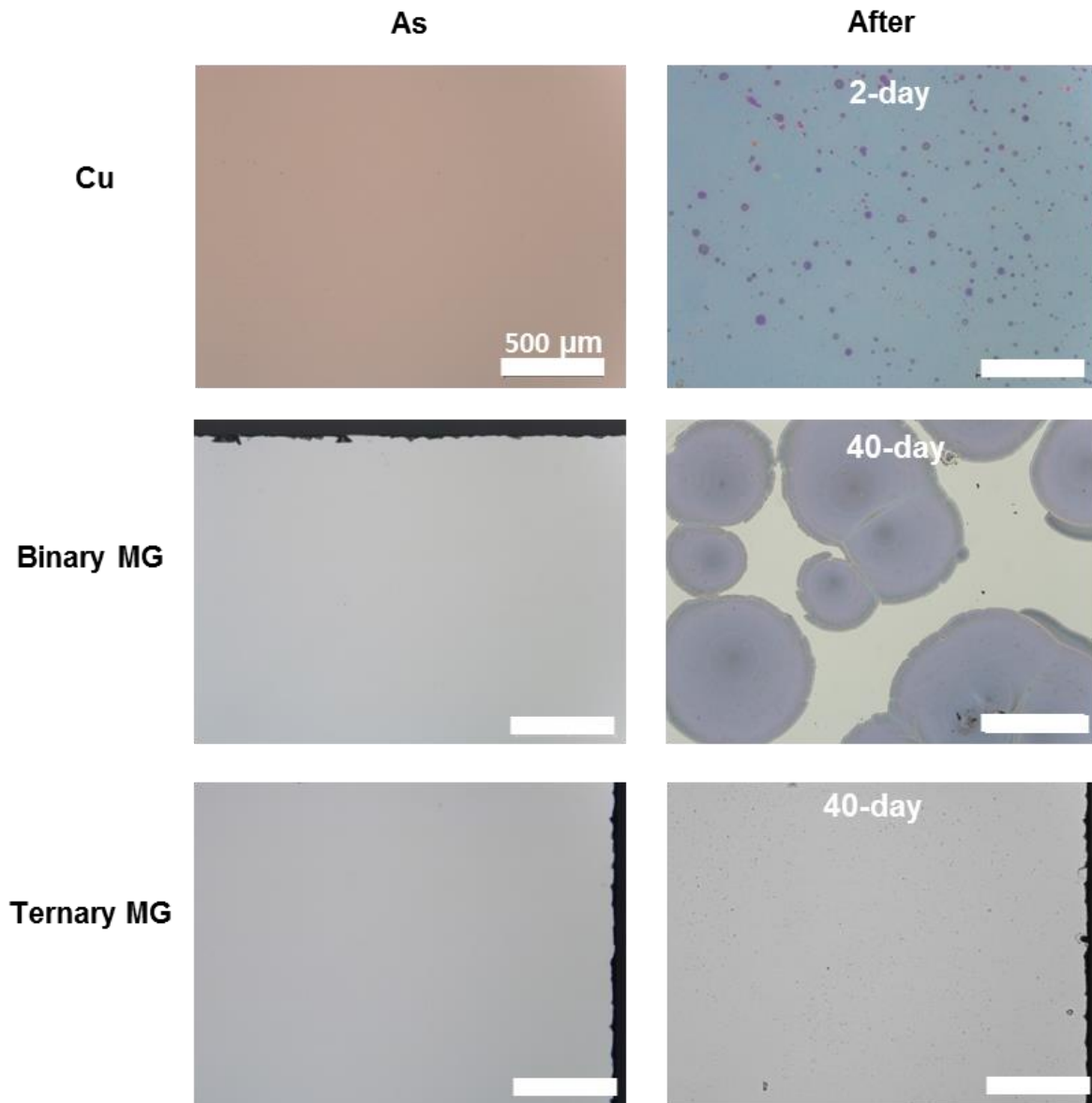


Figure 35. Surface of nanocrystalline Cu, binary and ternary metallic glass films for as-deposited and after oxidation under an environment of 85% relative humidity at 85°C.

At the 30 nm depth from the surface, the atomic percent of Zr and Cu element was shown to be the same as that of the as-deposited metallic glasses. Detailed XPS analysis of the Cu and Zr elements for different depths in oxidized binary and ternary metallic glass are shown in Figure 37 and 38. After oxidation for 1000 hours, the binding energy of the Zr 4p on top of (depth under 10 nm) the oxidized binary metallic glass is 182 eV and this binding energy value is same to the literature values for Zr in ZrO_2 . The binding energy of Cu 2p³ is 933 eV and beneath the 10 nm, a weak satellite feature at 945 eV was observed in Cu element of binary metallic glass. According to the XPS elemental concentration-depth profile, the atomic percent of Cu increased rapidly at about depth of 10 nm. It is concluded that 10 nm thick ZrO_2 is formed on top layer of binary metallic glass and below this thin ZrO_2 layer, Cu-enriched alloy with Cu oxide is formed after oxidized for 1000 hours under environment of 85% relative humidity at 85°C. With the going deep in depth, the binding energy of Zr element is appeared at 178.7 eV corresponding to metallic Zr, indicating binary metallic glass is oxidized partially (Figure 39). The Gibbs energies of formation for Zr and Cu oxides have been gathered in Table 3. The Gibbs energies of formation for ZrO_2 is much more negative than that for Cu oxides, meaning that Zr has much higher affinity to be oxidized than Cu. This indicates the selective oxidation of Zr over Cu in amorphous metallic glass. Along with the outward diffusion and thus depletion of Zr, Cu accumulates below the ZrO_2 layer and a Cu-enriched region can be formed.

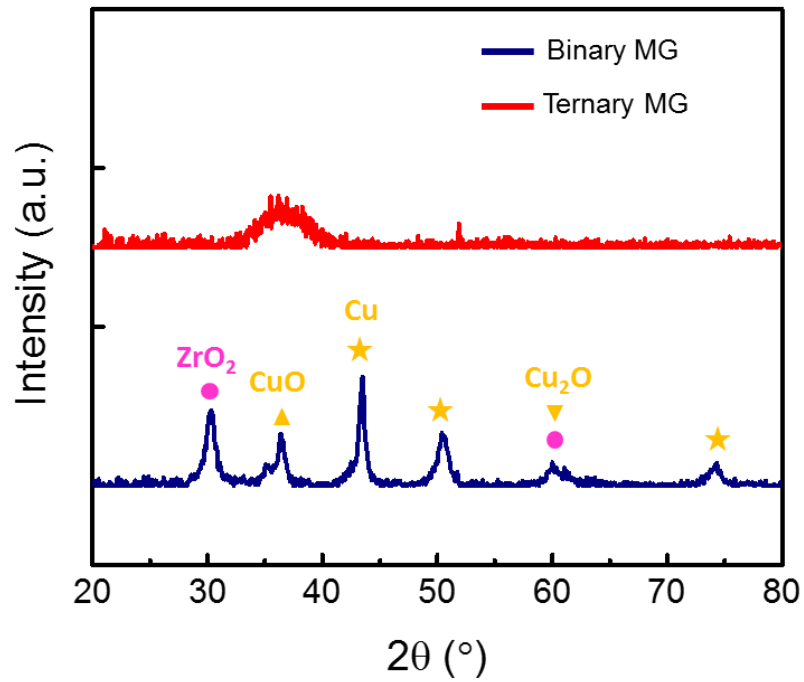


Figure 36. X-ray diffraction pattern of oxidized binary and ternary metallic glass thin films under an environment of 85% relative humidity at 85°C for 1000 hours.

Element	Oxide form	ΔG^0 (kJ/mol)
Cu	CuO	-128.3
	Cu ₂ O	-147.9
Zr	m-ZrO ₂	-1039.7
	t-ZrO ₂	-1037.3
	am-ZrO ₂	-972.7

Table 3. Gibbs energies of formation of Cu and Zr corresponding oxides.

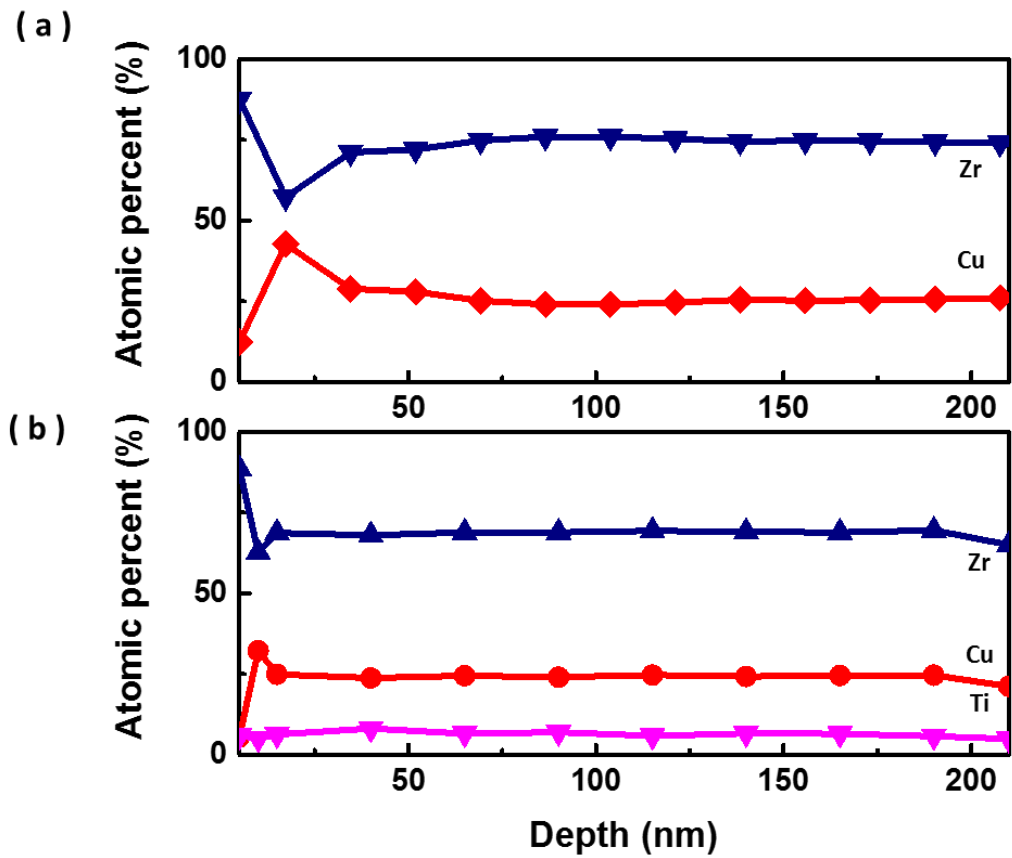


Figure 37. XPS element-depth profiles of oxidized metallic glass films: (a) binary metallic glass $\text{Cu}_{39}\text{Zr}_{61}$ and (b) ternary metallic glass $\text{Cu}_{31}\text{Zr}_{61}\text{Ti}_8$.

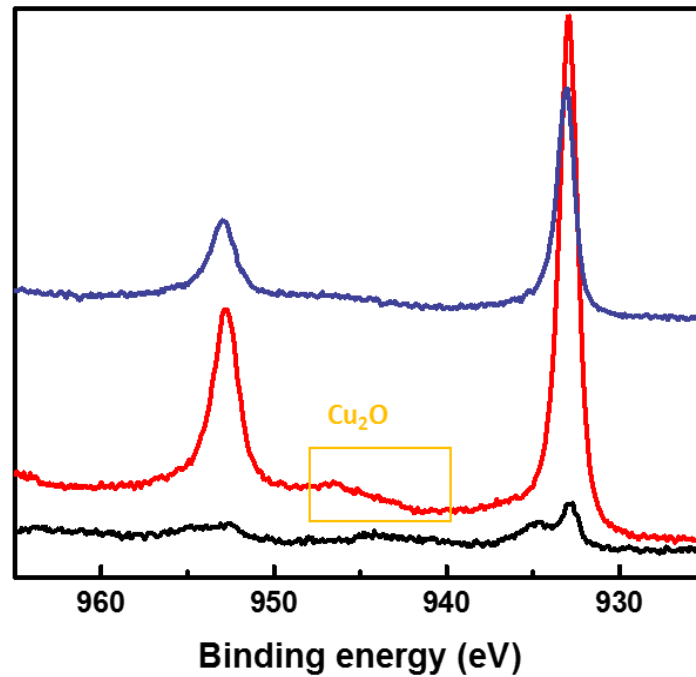


Figure 38. XPS spectra of $\text{Cu}2p_{3/2}$ level for different depths of oxidized binary metallic glass film.

On the other hand, the binding energy of the Zr 4p on top of ternary metallic glass after oxidation is 178.7 eV. Although the partially oxidized peak of Zr and Cu appeared on the surface, they are very small fraction in thickness of under 6 nm. It is concluded that ternary metallic glass maintains the amorphous structure without Zr oxidation in the whole region except for the surface for 1000 hours under environment of 85% relative humidity at 85°C.

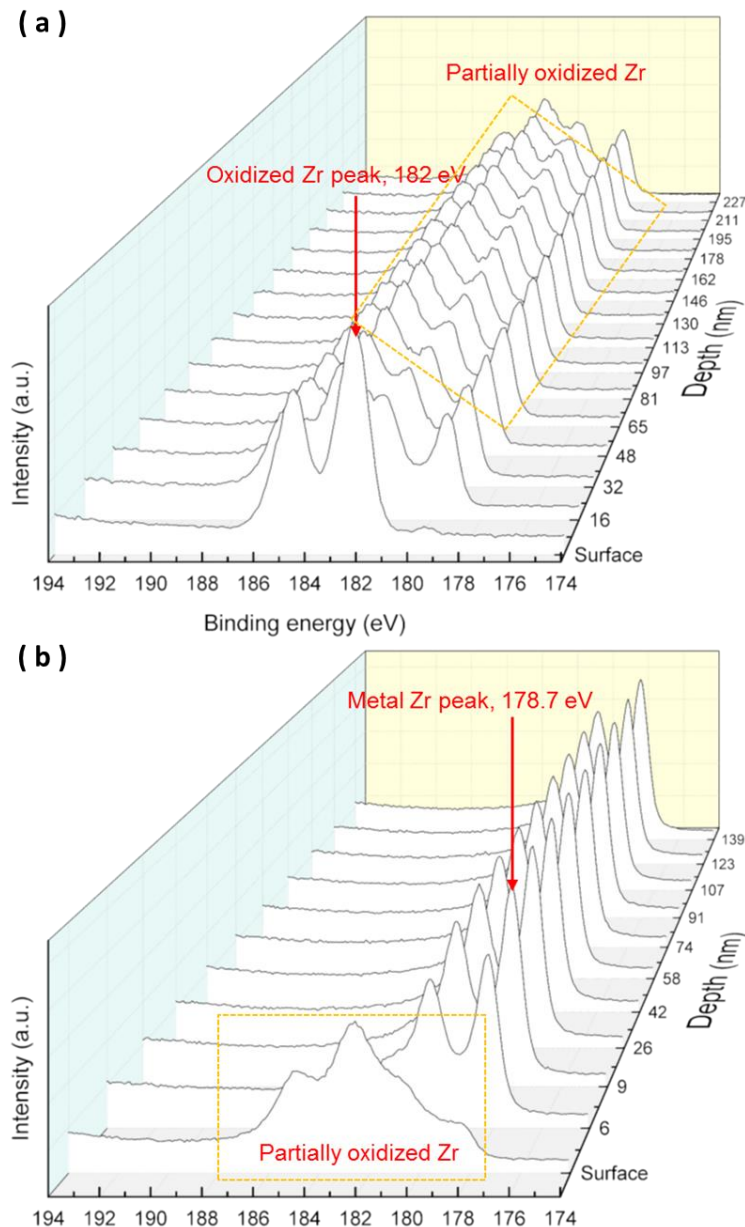


Figure 39. XPS spectra of Zr3d level for different depths of (a) oxidized binary metallic glass film and (b) oxidized ternary metallic glass film under environment of 85% relative humidity at 85°C.

Diffusion barrier performance of ternary metallic glass thin film after oxidation testing is confirmed by WVTR measurement. First, in order to prevent the PET substrate from being deformed, bare PET substrate is sufficiently oxidized for more than 5 days under environment of 85% relative humidity at 85°C. Ternary metallic glass thin film was deposited on the oxidized PET substrate by sputtering and metallic glass/PET samples were attached on Ca sensor deposited on glass substrate. As a result, as shown in Figure 40, WVTR of oxidized ternary metallic glass thin film was determined to $7.2 \pm 1.5 (\times 10^{-2}) \text{ gm}^{-2}\text{day}^{-1}$, showing similar characteristic with as deposited-ternary metallic glass thin film. The acceleration factor of ternary metallic glass was determined to be 78 in previous section, meaning 1000 hours in acceleration environment (85% relative humidity at 85°C) is equivalent to 9 years in use environment (40% relative humidity at 25°C). It is concluded that ternary metallic glass is expected to maintain diffusion barrier performance without structure change for 9 years, showing reliability as encapsulation film.

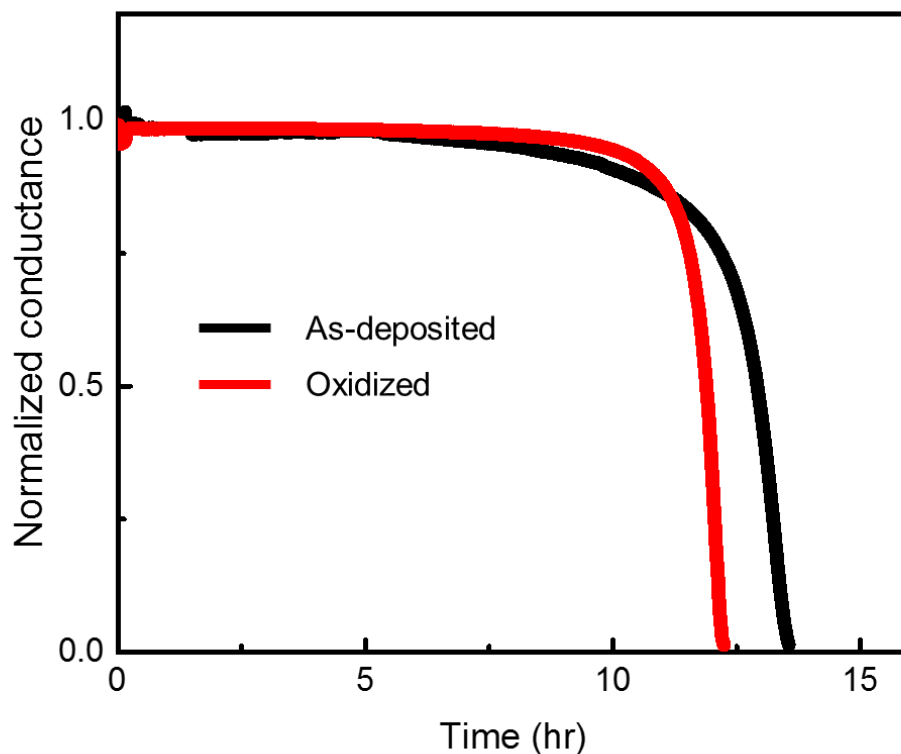


Figure 40. WVTR measurement results of as-deposited and oxidized ternary metallic glass thin film under environment of 85% relative humidity at 85°C.

4.3 Mechanical deformation of metallic glass thin film

In-situ SEM tensile test was performed to measure the mechanical properties of metallic glass thin films. Schematic for sample preparation is shown in Figure 41. Metallic glass films were deposited on Si substrate by sputtering and the freestanding metallic glass thin films were prepared by undercutting Si substrate by isotropic dry-etching using XeF_2 gas. Micro-tensile samples in dog-bone shape with dimensions of $1 \mu\text{m}$ gauge width \times $4 \mu\text{m}$ gauge length were prepared by focused ion beam (FIB) (FEI Quanta 3D) milling. Micro-tensile samples were transferred onto push-to-pull (P-to-P) devices (provided by Hysitron) using an Omniprobe micromanipulator for in-situ SEM micro-tensile testing. Both ends of the micro-tensile sample were gripped by ion-beam assisted platinum (Pt) deposition. Micro-tensile tests were carried out using Picoindenter (Hysitron PI-87) with a flat punch indenter in SEM (FEI Quanta 200). The tests were performed under constant strain rate $1 \times 10^{-3} \text{ s}^{-1}$ and movies were recorded in FE-SEM in real-time. Since the force obtained by Picoindenter contains the spring stiffness of the push-to-pull device, the actual force to dog-gone shaped sample was computed by subtracting the estimated force using the spring stiffness of the push-to-pull devices. Initial sample geometry was measured by SEM images and gauge length change was measured by still images extracted from the movie, from which true stress and strain were calculated.

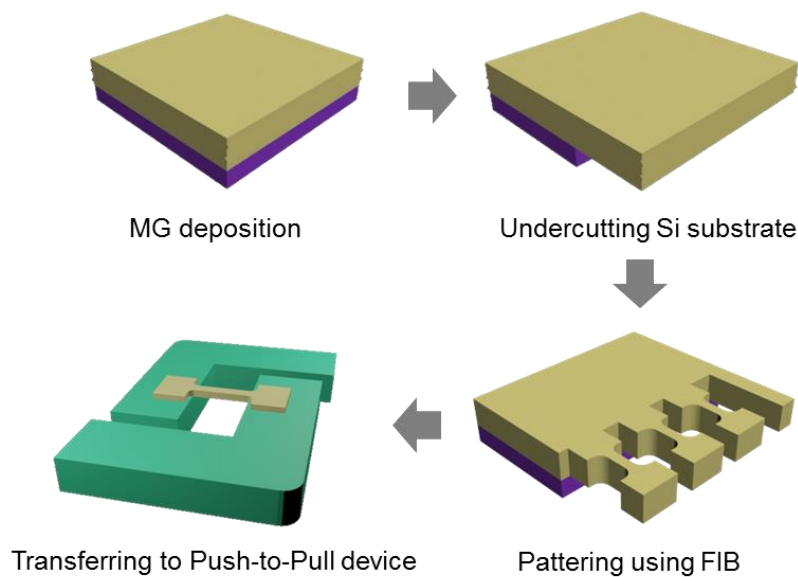


Figure 41. Schematic of sample preparation for tensile testing.

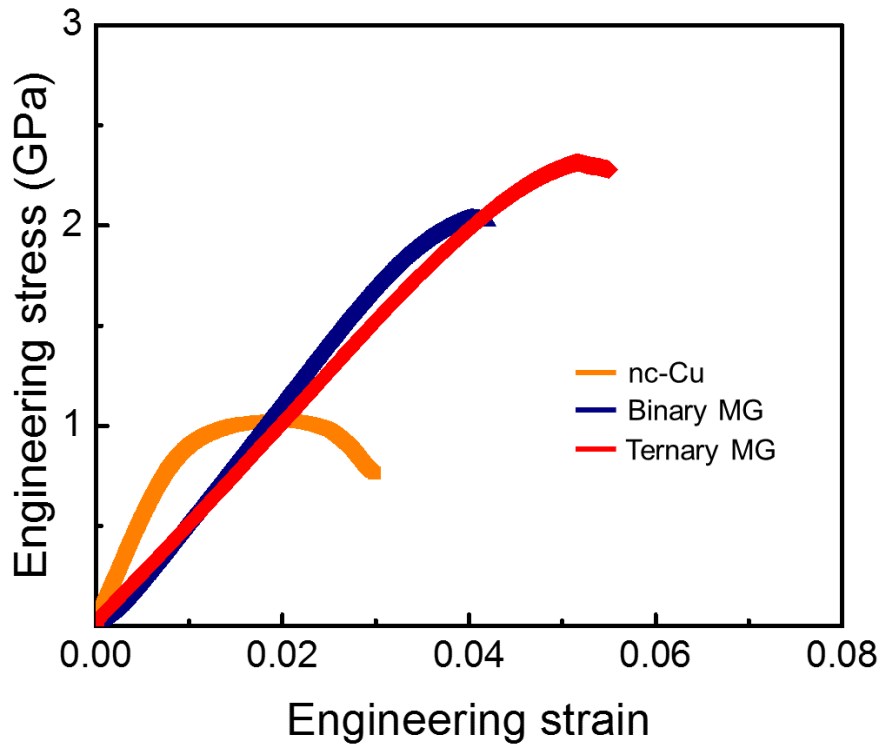


Figure 42. Typical stress-strain curves of nanocrystalline copper film, binary metallic glass and ternary metallic glass films for in-situ tensile testing.

Typical stress-strain curve and mechanical properties for nanocrystalline copper, binary and ternary metallic glass films is shown in Figure 42. The 260 nm - thick nanocrystalline copper thin film show elastic deformation followed by nonlinear plasticity, work hardening, and necking: ultimate tensile strength of 1.02 GPa, yield strength of 0.93 GPa, and fracture strain of 3.24 %. However, as shown in Figure 43, nanocrystalline Cu metal film exhibit shear-off fracture behavior, differently from general ductile metal, attributing structure of nanocrystalline copper different from bulk pure metals. Among the tensile tests performed on pure nanocrystalline metals, the first test was done by Nieman *et al* [82]. The nanocrystalline Pd showed 7 times higher yield stress than that of annealed coarse-grained Pd. It is also found that tensile properties of nanocrystalline Cu exhibit 5 times higher yield stress than that of annealed coarse-grained copper [83]. Sanders *et al.* investigated elastic and tensile behaviors of nanocrystalline Cu dependent on structure such as density and purity. Nanocrystalline Cu samples with

grain size of 10-110 nm and density of greater than 98% were prepared by inert-gas condensation and warm compaction method, and the elastic properties were measured. The tensile modulus of nanocrystalline Cu with grain size of 20-110 nm exhibited $104 (\pm 0.3)$ GPa, similar value with elastic modulus of nanocrystalline Cu deposited using sputtering. For Cu with gran sizes below 100 nm, higher strengths and lower elongations were observed. J. Y. Zhang *et al.* found that yield strength of Cu thin film increases with recuing grain size and somewhat drops occurs when grain size of Cu thin film reduces to about 20 nm. Strengthening mechanism in metallic thin films can be divided into two kinds, dislocation glide-controlled effect and nucleation-controlled effect. Nanocrystalline Cu deposited by sputtering in here, is expected to have structure with grain size of under 20 nm, leading to significantly higher strength and elongation than those of reported nanocrystalline Cu in previous research.

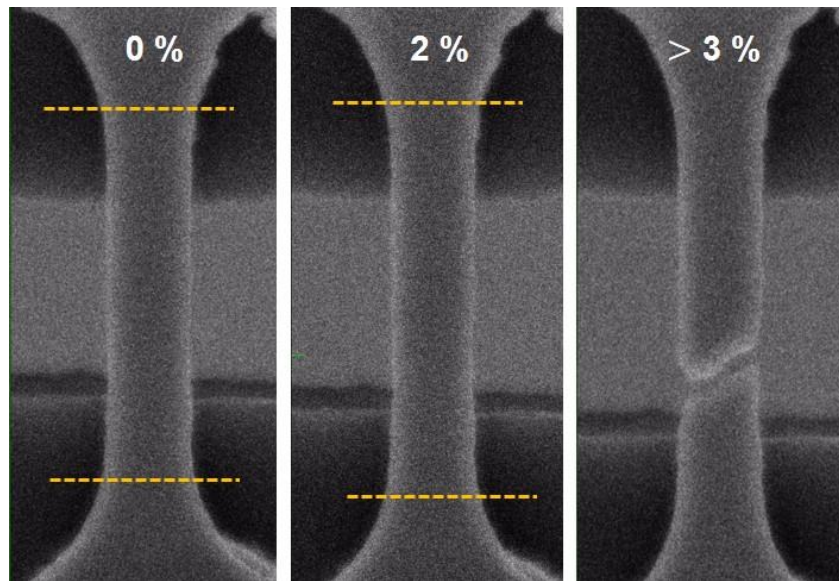


Figure 43. SEM images of nanocrystalline Cu during in situ tensile testing showing elastic deformation followed by necking and fracture with shear-off around 3% strain.

On the other hand, both binary and ternary metallic glass show typical brittle fraction behavior, linear elastic deformation followed by sudden and catastrophic failure directly (Figure 44). Yield

strength and strain of binary metallic glass was measured to $1.93 (\pm 0.3)$ GPa and $3.45 (\pm 0.4)$ %, respectively, by 0.2% offset method. Compared to binary metallic glass, ternary metallic glass shows higher yield strength of $2.27 (\pm 0.04)$ GPa and yield strain of $4.37 (\pm 0.1)$ %, showing enhanced elastic limit and feasibility for utilizing as stretchable encapsulation materials. The increased in yield strength and elastic limit can be attributed to addition of Ti element in Cu-Zr metallic glass system. This increased in yield strength and elastic limit can be explained by increasing in structural inhomogeneity of ternary metallic glass configuration. E. Ma and J. Ding reported that intrinsic potential of ductility of amorphous structure molecular dynamic simulation [84]. An atomic configuration of monolithic Cu-Zr metallic glass exhibits a wide range of local configurations in atoms, differently crystalline materials. This distribution of local environments has characteristic short-range order (SRO), which is the most favored type of atomic configuration motif. In the meantime, there are also unfavored configuration in a range of variations, called geometrically unfavored motifs (GUMs). The GUMs may be local packing configurations with less range order occurred due to the fast cooling rate when the metallic glass is formed, leading to average excess free volume. Such configuration is more flexible to re-configure themselves and hence to more prone to deform elastically under stress state. As a result, when a high content of GUMs is contained in metallic glass, it would tend to show more liquid like behavior under applied stresses. In other words, the addition of Ti element in Cu-Zr metallic glass attribute to increase local region containing GUMs, leading to enhanced yield strength and elastic limit compared to binary metallic glass.

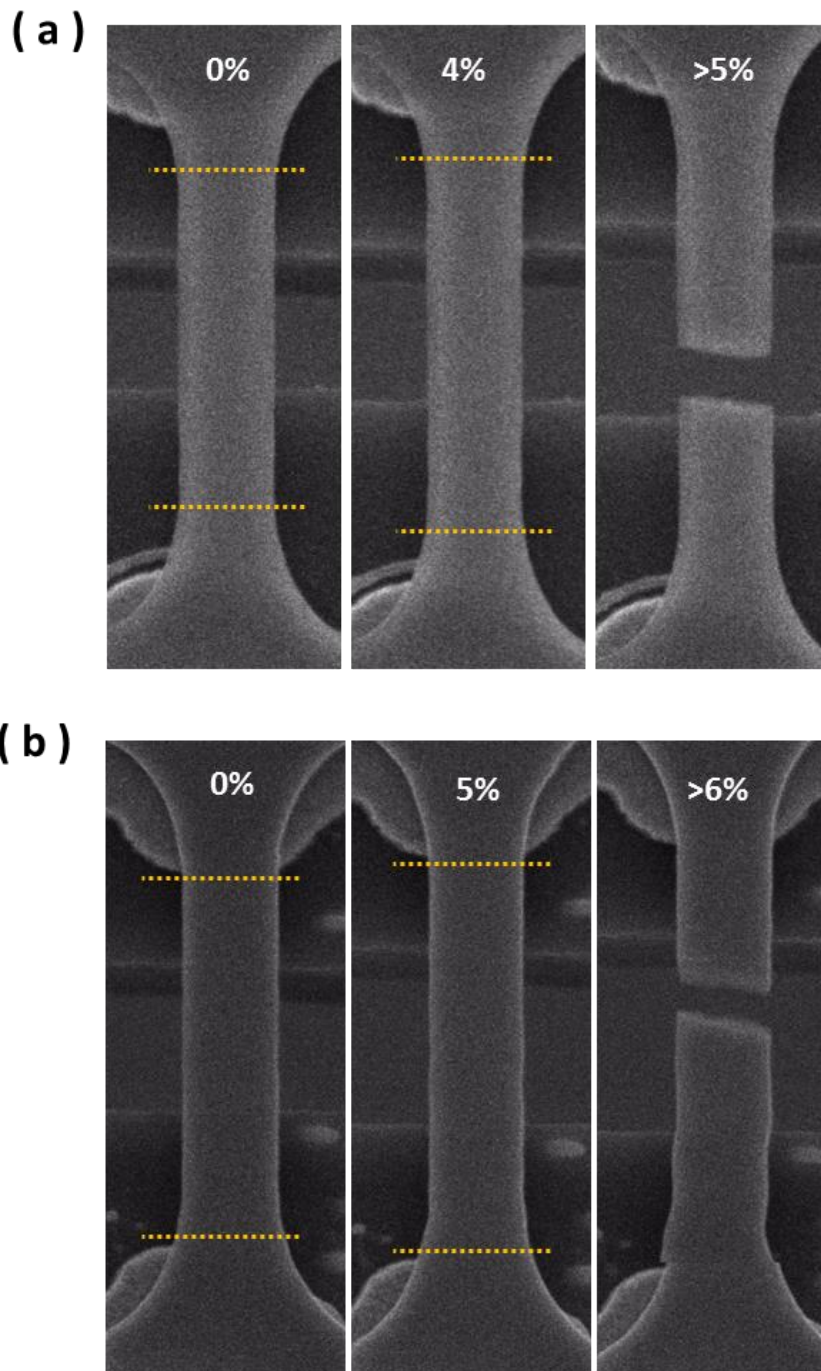


Figure 44. SEM images of (a) binary metallic glass and (c) ternary metallic glass tensile samples during in situ tensile testing showing elastic deformation followed by fracture with single shear banding.

4.4 Cyclic stretching behavior of thin film

The actual operating conditions for flexible, wearable, and stretchable devices may include cyclic mechanical deformation, so it is necessary to understand the fatigue behavior of their components. Fatigue damage formation was investigated after cyclic stretching of metallic glass thin film. Polydimethylsiloxane (PDMS) is used as stretchable substrate. The PDMS (Sylgard 184, Dow Corning) and curing agent were mixed with weight ratio of 1:10, then mixed PDMS was cured in an oven at 70°C for 2 hours. Metallic glass thin films with a thickness of 250 nm were deposited on PDMS substrate by sputtering. For reliability in repeated stretching behavior cyclic stretching test was performed using a customized repeated stretching system. The PDMS substrate were gripped at both ends by designed grips. The cyclic stretching was carried out up to 1000 cycles and applied stretching strains were 2% and 4% for both binary and ternary metallic glass thin films. The change in morphology of the metallic glass thin films on PDMS substrate were observed after cyclic stretching using scanning electron microscopy (Nano 230, FEI) and atomic force microscopy (Veeco).

Figure 45 shows the morphology of metallic glass-coated PDMS, showing the buckled wavy structure. This formation of wavy structure can be attributed to pre-strain on PDMS substrate caused by high vacuum environment. Recently, many researches have been reported that a wavy structure on film through nonlinear buckling or wrinkling on soft substrate is designed to enhance the deformability of materials for application in stretchable electronic devices [85] [86]. There are some strategies to induce buckling in thin films, such as mechanical pre-strain on substrate, different thermal mismatch, surface treatment using ultraviolet ozone, or etching by focused ion beam. For instance, in the case of using mechanical strain, tensile strain can be applied to the substrate, and then then thin film can be deposited on pre-strained substrate. When the strain in the substrate is released, wrinkling of the thin film can be formed if the applied compressive strain on thin film exceeds a critical value. In other words, buckling structure of metallic glass thin film on substrate can be attributed to pre-strained PDMS substrate in high vacuum environment during deposition process.

Forming of wrinkling results from the process to balance the energy of materials between bending energy of thin film and deformation energy of the substrate. This means that the pattern of wrinkling in thin film is determined by material properties of substrate and thin film, as well as the thickness of thin film. Based on small deformation theory, the total energy of thin film-substrate system consists of three terms, membrane energy, bending energy of thin film, and strain energy of substrate. Minimizing the total energy with respect to buckling amplitude (A_0) and wavelength (λ_0) gives as following:

$$A_0 = h_f \sqrt{\frac{\varepsilon_{pre}}{\varepsilon_c} - 1}, \quad \lambda_0 = 2\pi h_f \left(\frac{E_f}{3E_s}\right)^{1/3}, \quad (17)$$

where h_f is the thickness of thin film, ε_{pre} is the pre-strain, E_f is the elastic modulus of thin film, E_s is the elastic modulus of substrate, and ε_c is the critical buckling strain, determined by $(1/4)(3E_s/E_f)^{2/3}$. When the pre-strain applied to the substrate is larger than critical strain, buckling structure can be formed. Through measurement of wavelength and amplitude by atomic-force microscopy, pre-strain by swelling of PDMS can be estimated using above relations. As shown in Figure 45, wavelength and amplitude of wrinkle for metallic glass thin film on PDMS is measured to 60 μm and 0.7 μm , respectively. For 250 nm-thick metallic glass thin film on PDMS, the applied pre-strain on PDMS substrate during sputtering deposition is determined to be about 0.3 % pre-strain.

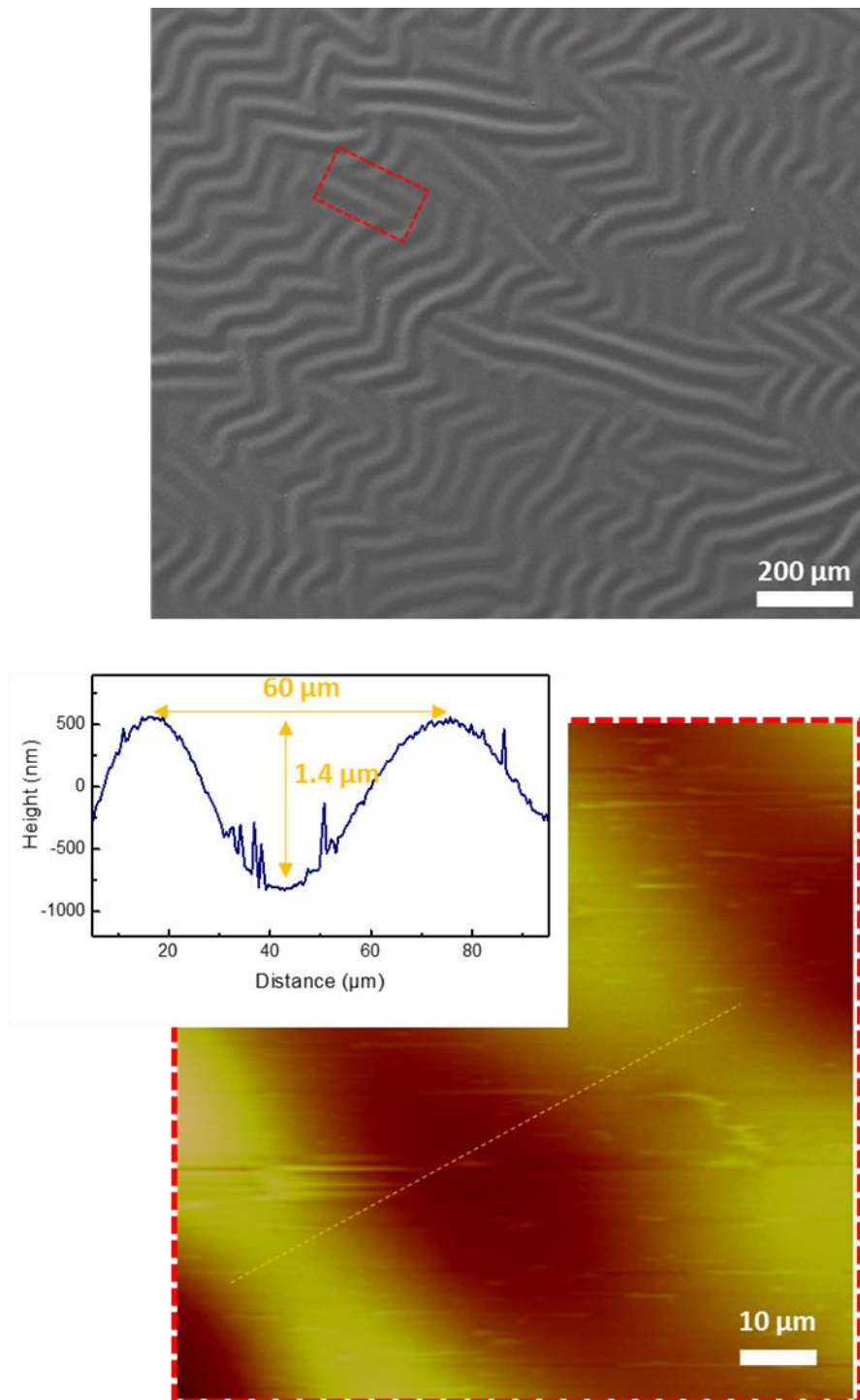


Figure 45. SEM and AFM images of wrinkled metallic glass thin film on PDMS substrate.

Surface profile of wrinkle structure for measurement of amplitude and wavelength.

After the cyclic stretching tests up to 2%, fatigue damage was observed in nanocrystalline copper film and no cracks were observed on surface of for binary and ternary metallic glasses as shown in Figure 46. Further cyclic stretching test up to 4%, fatigue damage such as crack and linear fracture occurs in binary metallic glass. With magnified view of the fatigue damage, cracks to vertical to the stretching direction formed and evolved to longer and crack line density increased. On the other hand, no fatigue damages were observed in ternary metallic glass after cyclic stretching test up to 1000 cycles at 4%.

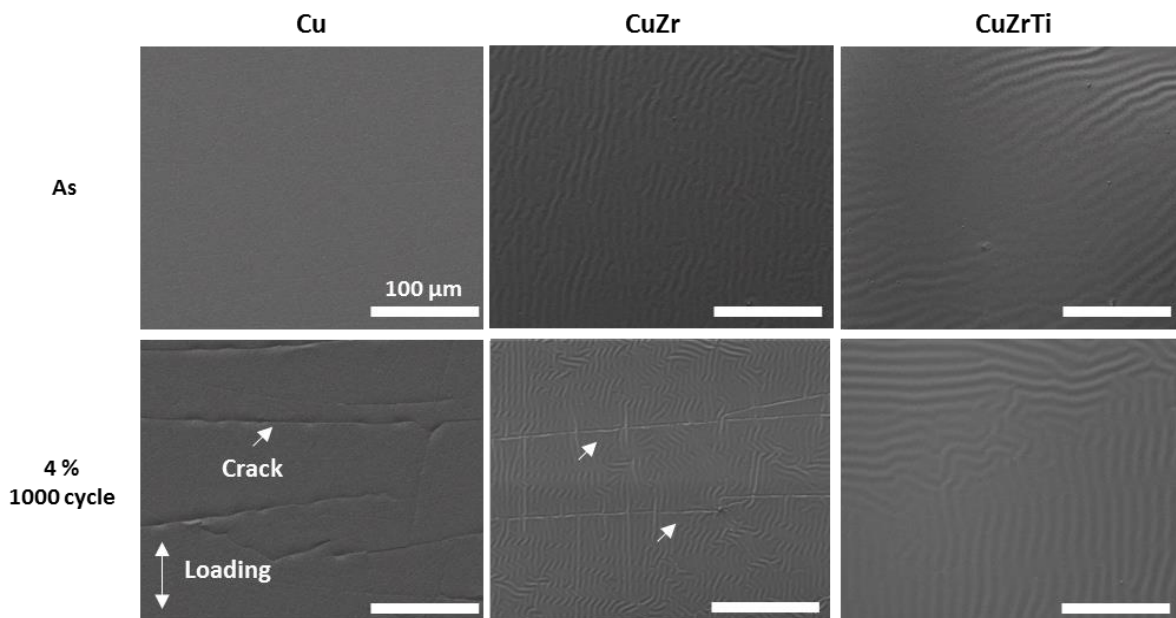


Figure 46. SEM images of nanocrystalline Cu, binary and ternary metallic glass thin films for as-deposited and after cyclic stretching 1000 cycles at 4% strain.

Chapter 5. Conclusion

Mechanical behavior of nanolaminate is investigated and graphene is used for interfacial material. Nanolaminate was designed and fabricated by alternating six 60 nm-thick layers of $\text{Cu}_{50}\text{Zr}_{50}$ metallic glass and five graphene. In-situ micro-tensile testing revealed (1) enhanced elastic modulus and yield strength of nanolaminates comparing with 360 nm-thick monolithic metallic glass, which was explained by simple rule-of-mixture, and (2) explicit homogeneous flow in 60 nm-thick metallic glass layers leading to improved tensile ductility of nanolaminates. Despite mechanical properties of metallic glass deforming by homogeneous flow at reduced size and graphene, their structural application individually is very limited due to small external size. Suggested nanolaminate with high elastic deformation is so size-adjustable as well as improved mechanical properties that expand applications of metallic glass and graphene.

Utilizing metallic glass thin film with high elastic deformation, stretchable encapsulation material and technique was developed and investigated by oxidation and mechanical testing. Key ideas in the development is (1) enhancing thermal stability and diffusion barrier characteristic by using high corrosion resistance properties of metallic glass thin film with minor addition component, leading to high glass forming ability and stable amorphous structure even under acceleration environment, and (2) improving tensile properties of ternary metallic glass thin film by suppressing shear band formation and propagation, attributing to instability of shear band formation by introducing minor component in the system. The ternary metallic glass thin film with high thermal stability was fabricated by co-sputtering process and investigated oxidation resistance through acceleration test under environment of 85% relative humidity at 85 °C. The electrical Ca test was performed to evaluate diffusion barrier characteristic and revealed 260 nm thick metallic glass in the system of Cu-Zr-Ti has water vapor transmission rate of 10^{-3} order. Stretchability of ternary metallic glass thin film is evaluated as 4 % through in situ tensile testing and cyclic stretching testing, showing feasibility for stretchable encapsulation material.

Reference

- [1] W. Klement, R.H. Willens, P.O.L. Duwez, Non-crystalline Structure in Solidified Gold–Silicon Alloys, *Nature* 187(4740) (1960) 869-870.
- [2] W.H. Wang, C. Dong, C.H. Shek, Bulk metallic glasses, *Materials Science and Engineering: R: Reports* 44(2) (2004) 45-89.
- [3] A. Gebert, K. Buchholz, A. Leonhard, K. Mummert, J. Eckert, L. Schultz, Investigations on the electrochemical behaviour of Zr-based bulk metallic glasses, *Materials Science and Engineering: A* 267(2) (1999) 294-300.
- [4] M.D. Demetriou, A. Wiest, D.C. Hofmann, W.L. Johnson, B. Han, N. Wolfson, G. Wang, P.K. Liaw, Amorphous metals for hard-tissue prosthesis, *JOM* 62(2) (2010) 83-91.
- [5] K.S. Nakayama, Y. Yokoyama, T. Ono, M.W. Chen, K. Akiyama, T. Sakurai, A. Inoue, Controlled Formation and Mechanical Characterization of Metallic Glassy Nanowires, *Advanced Materials* 22(8) (2010) 872-875.
- [6] M. Telford, The case for bulk metallic glass, *Materials Today* 7(3) (2004) 36-43.
- [7] T. Masumoto, R. Maddin, The mechanical properties of palladium 20 at/o silicon alloy quenched from the liquid state, *Acta Metallurgica* 19(7) (1971) 725-741.
- [8] A.S. Argon, Plastic deformation in metallic glasses, *Acta Metallurgica* 27(1) (1979) 47-58.
- [9] F. Delogu, Identification and Characterization of Potential Shear Transformation Zones in Metallic Glasses, *Physical Review Letters* 100(25) (2008) 255901.
- [10] F. Delogu, Molecular dynamics of shear transformation zones in metallic glasses, *Intermetallics* 16(5) (2008) 658-661.
- [11] E.R. Homer, Examining the initial stages of shear localization in amorphous metals, *Acta Materialia* 63 (2014) 44-53.
- [12] D.C. Hofmann, J.Y. Suh, A. Wiest, G. Duan, M.L. Lind, M.D. Demetriou, W.L. Johnson, Designing metallic glass matrix composites with high toughness and tensile ductility, *Nature* 451(7182) (2008) 1085-9.

- [13] F. Szuecs, C.P. Kim, W.L. Johnson, Mechanical properties of Zr₅₆Ti₁₃Nb₅Cu₆Ni₅Be_{12.5} ductile phase reinforced bulk metallic glass composite, *Acta Materialia* 49(9) (2001) 1507-1513.
- [14] D.G. Pan, H.F. Zhang, A.M. Wang, Z.Q. Hu, Enhanced plasticity in Mg-based bulk metallic glass composite reinforced with ductile Nb particles, *Applied Physics Letters* 89(26) (2006) 261904.
- [15] H. Guo, P.F. Yan, Y.B. Wang, J. Tan, Z.F. Zhang, M.L. Sui, E. Ma, Tensile ductility and necking of metallic glass, *Nat Mater* 6(10) (2007) 735-9.
- [16] D. Jang, J.R. Greer, Transition from a strong-yet-brittle to a stronger-and-ductile state by size reduction of metallic glasses, *Nat Mater* 9(3) (2010) 215-219.
- [17] T. Cullinan, I. Kalay, Y.E. Kalay, M. Kramer, R. Napolitano, Kinetics and Mechanisms of Isothermal Devitrification in Amorphous Cu₅₀Zr₅₀, *Metallurgical and Materials Transactions A* 46(2) (2015) 600-613.
- [18] J. Dudonis, R. Bručas, A. Miniotas, Synthesis of amorphous Zr-Cu alloys by magnetron co-sputtering, *Thin Solid Films* 275(1) (1996) 164-167.
- [19] X.Y. J. Qin, Z. X-Y, , Zr-Cu Amorphous Films Prepared by Magnetron Co-sputtering Deposition of Pure Zr and Cu, *Chinese Physics Letter* 26(8).
- [20] C.-C. Yu, J.P. Chu, H. Jia, Y.-L. Shen, Y. Gao, P.K. Liaw, Y. Yokoyama, Influence of thin-film metallic glass coating on fatigue behavior of bulk metallic glass: Experiments and finite element modeling, *Materials Science and Engineering: A* 692 (2017) 146-155.
- [21] J.P. Chu, J.S.C. Jang, J.C. Huang, H.S. Chou, Y. Yang, J.C. Ye, Y.C. Wang, J.W. Lee, F.X. Liu, P.K. Liaw, Y.C. Chen, C.M. Lee, C.L. Li, C. Rullyani, Thin film metallic glasses: Unique properties and potential applications, *Thin Solid Films* 520(16) (2012) 5097-5122.
- [22] E.S. Puchi-Cabrera, F. Matínez, I. Herrera, J.A. Berríos, S. Dixit, D. Bhat, On the fatigue behavior of an AISI 316L stainless steel coated with a PVD TiN deposit, *Surface and Coatings Technology* 182(2) (2004) 276-286.
- [23] C.L. Chiang, J.P. Chu, F.X. Liu, P.K. Liaw, R.A. Buchanan, A 200nm thick glass-forming metallic film for fatigue-property enhancements, *Applied Physics Letters* 88(13) (2006) 131902.

- [24] D. Wang, H. Tan, Y. Li, Multiple maxima of GFA in three adjacent eutectics in Zr–Cu–Al alloy system – A metallographic way to pinpoint the best glass forming alloys, *Acta Materialia* 53(10) (2005) 2969-2979.
- [25] M.C. Liu, C.J. Lee, Y.H. Lai, J.C. Huang, Microscale deformation behavior of amorphous/nanocrystalline multilayered pillars, *Thin Solid Films* 518(24) (2010) 7295-7299.
- [26] S.Y. Kuan, H.S. Chou, M.C. Liu, X.H. Du, J.C. Huang, Micromechanical response for the amorphous/amorphous nanolaminates, *Intermetallics* 18(12) (2010) 2453-2457.
- [27] J.-Y. Kim, D. Jang, J.R. Greer, Nanolaminates Utilizing Size-Dependent Homogeneous Plasticity of Metallic Glasses, *Advanced Functional Materials* 21(23) (2011) 4550-4554.
- [28] Y.-F. Liew, H. Aziz, N.-X. Hu, H.S.-O. Chan, G. Xu, Z. Popovic, Investigation of the sites of dark spots in organic light-emitting devices, *Applied Physics Letters* 77(17) (2000) 2650-2652.
- [29] A. Turak, Interfacial degradation in organic optoelectronics, *RSC Advances* 3(18) (2013) 6188-6225.
- [30] J. Huang, S. Tan, P.D. Lund, H. Zhou, Impact of H₂O on organic–inorganic hybrid perovskite solar cells, *Energy & Environmental Science* 10(11) (2017) 2284-2311.
- [31] P.E. Burrows, V. Bulovic, S.R. Forrest, L.S. Sapochak, D.M. McCarty, M.E. Thompson, Reliability and degradation of organic light emitting devices, *Applied Physics Letters* 65(23) (1994) 2922-2924.
- [32] J.S. Lewis, M.S. Weaver, Thin-film permeation-barrier technology for flexible organic light-emitting devices, *IEEE Journal of Selected Topics in Quantum Electronics* 10(1) (2004) 45-57.
- [33] D. Yu, Y.-Q. Yang, Z. Chen, Y. Tao, Y.-F. Liu, Recent progress on thin-film encapsulation technologies for organic electronic devices, *Optics Communications* 362 (2016) 43-49.
- [34] S.-W. Seo, E. Jung, H. Chae, S.M. Cho, Optimization of Al₂O₃/ZrO₂ nanolaminate structure for thin-film encapsulation of OLEDs, *Organic Electronics* 13(11) (2012) 2436-2441.
- [35] E.G. Jeong, Y.C. Han, H.-G. Im, B.-S. Bae, K.C. Choi, Highly reliable hybrid nano-stratified moisture barrier for encapsulating flexible OLEDs, *Organic Electronics* 33 (2016) 150-155.
- [36] M.-H. Park, J.-Y. Kim, T.-H. Han, T.-S. Kim, H. Kim, T.-W. Lee, Flexible Lamination Encapsulation, *Advanced Materials* 27(29) (2015) 4308-4314.

- [37] M.-C. Choi, Y. Kim, C.-S. Ha, Polymers for flexible displays: From material selection to device applications, *Progress in Polymer Science* 33(6) (2008) 581-630.
- [38] J. Meyer, P. Görrn, F. Bertram, S. Hamwi, T. Winkler, H.-H. Johannes, T. Weimann, P. Hinze, T. Riedl, W. Kowalsky, Al₂O₃/ZrO₂ Nanolaminates as Ultrahigh Gas-Diffusion Barriers—A Strategy for Reliable Encapsulation of Organic Electronics, *Advanced Materials* 21(18) (2009) 1845-1849.
- [39] G.H. Lee, R.C. Cooper, S.J. An, S. Lee, A. van der Zande, N. Petrone, A.G. Hammerberg, C. Lee, B. Crawford, W. Oliver, J.W. Kysar, J. Hone, High-strength chemical-vapor-deposited graphene and grain boundaries, *Science* 340(6136) (2013) 1073-6.
- [40] C. Lee, X. Wei, J.W. Kysar, J. Hone, Measurement of the elastic properties and intrinsic strength of monolayer graphene, *Science* 321(5887) (2008) 385-8.
- [41] A.A. Balandin, S. Ghosh, W. Bao, I. Calizo, D. Teweldebrhan, F. Miao, C.N. Lau, Superior Thermal Conductivity of Single-Layer Graphene, *Nano Letters* 8(3) (2008) 902-907.
- [42] M.Y. Han, B. Ozyilmaz, Y. Zhang, P. Kim, Energy band-gap engineering of graphene nanoribbons, *Phys Rev Lett* 98(20) (2007) 206805.
- [43] I.N. Kholmanov, C.W. Magnuson, A.E. Aliev, H. Li, B. Zhang, J.W. Suk, L.L. Zhang, E. Peng, S.H. Mousavi, A.B. Khanikaev, R. Piner, G. Shvets, R.S. Ruoff, Improved electrical conductivity of graphene films integrated with metal nanowires, *Nano Lett* 12(11) (2012) 5679-83.
- [44] Y. Kim, J. Lee, M.S. Yeom, J.W. Shin, H. Kim, Y. Cui, J.W. Kysar, J. Hone, Y. Jung, S. Jeon, S.M. Han, Strengthening effect of single-atomic-layer graphene in metal-graphene nanolayered composites, *Nat Commun* 4 (2013) 2114.
- [45] B. Wang, B.V. Cunniff, S.Y. Park, M. Huang, J.Y. Kim, R.S. Ruoff, Graphene Coatings as Barrier Layers to Prevent the Water-Induced Corrosion of Silicate Glass, *ACS Nano* (2016).
- [46] M. Hammad, J.J. Adjizian, C.H. Sacré, B. Huet, J.C. Charlier, J.P. Raskin, T. Pardoen, Adhesionless and near-ideal contact behavior of graphene on Cu thin film, *Carbon* 122 (2017) 446-450.
- [47] S.-Y. Park, E.-J. Gwak, M. Huang, R.S. Ruoff, J.-Y. Kim, Nanolaminate of metallic glass and graphene with enhanced elastic modulus, strength, and ductility in tension, *Scripta Materialia* 139 (2017) 63-66.

- [48] A.C. Ferrari, J.C. Meyer, V. Scardaci, C. Casiraghi, M. Lazzeri, F. Mauri, S. Piscanec, D. Jiang, K.S. Novoselov, S. Roth, A.K. Geim, Raman spectrum of graphene and graphene layers, *Phys Rev Lett* 97(18) (2006) 187401.
- [49] D.W. Kim, J. Lee, S.J. Kim, S. Jeon, H.-T. Jung, The effects of the crystalline orientation of Cu domains on the formation of nanoripple arrays in CVD-grown graphene on Cu, *Journal of Materials Chemistry C* 1(47) (2013) 7819.
- [50] Z.-J. Wang, G. Weinberg, Q. Zhang, T. Lunkenbein, A. Klein-Hoffmann, M. Kurnatowska, M. Plodinec, Q. Li, L. Chi, R. Schloegl, M.-G. Willinger, Direct observation of graphene growth and associated copper substrate dynamics by in situ scanning electron microscopy, *ACS Nano* 9 (2015) 1506-1519.
- [51] J.-Y. Kim, J.-J. Lee, Y.-H. Lee, J.-i. Jang, D. Kwon, Surface roughness effect in instrumented indentation: A simple contact depth model and its verification, *Journal of Materials Research* 21(12) (2011) 2975-2978.
- [52] J.-Y. Kim, S.-K. Kang, J.-J. Lee, J.-i. Jang, Y.-H. Lee, D. Kwon, Influence of surface-roughness on indentation size effect, *Acta Materialia* 55(10) (2007) 3555-3562.
- [53] S.-Y. Park, Y.-C. Kim, R.S. Ruoff, J.-Y. Kim, Incipient plasticity and fully plastic contact behavior of copper coated with a graphene layer, *APL Materials* 7(3) (2019) 031106.
- [54] K.L. Johnson, K.L. Johnson, *Contact mechanics*, Cambridge university press 1987.
- [55] A. Gouldstone, H.-J. KOH, K.-Y. Zeng, A.E. Giannakopoulos, S. Suresh, Discrete and continuous deformation during nanoindentation of thin films, *Acta Materialia* 48 (2000) 2277-2295.
- [56] X. Mi, V. Meunier, N. Koratkar, Y. Shi, Facet-insensitive graphene growth on copper, *Physical Review B* 85(15) (2012).
- [57] S. Suresh, A.E. Giannakopoulos, A new method for estimating residual stresses by instrumented sharp indentation, *Acta Materialia* 46 (1998) 5755-5767.
- [58] K. Sun, W. Shen, L. Ma, The influence of residual stress on incipient plasticity in single-crystal copper thin film under nanoindentation, *Computational Materials Science* 81 (2014) 226-232.
- [59] S. Pathak, L.J. Riesterer, R.S. Kalidindi, J. Michler, Understanding pop-ins in spherical

nanoindentation, *Applied Physics Letters* 105 (2014).

[60] M.S. Hu, A method for finding critical stresses of dislocation movement, *Applied Physics Letters* 31(139) (1977).

[61] O.W. C., G.M. Pharr, An improved technique for determining hardness and elastic modulus using load and displacement sensing indentation experiments, *Journal of Materials Research* 7(6) (1992) 1564-1583.

[62] W.C. Oliver, G.M. Pharr, Measurement of hardness and elastic modulus by instrumented indentation: Advances in understanding and refinements to methodology, *Journal of Materials Research* 19(1) (2011) 3-20.

[63] S. Suresh, T.-G. Nieh, B. Choi, Nano-indentation of copper thin films on silicon substrates, *Scripta Materialia* 41(9) (1999) 951-957.

[64] X. Tan, J. Wu, K. Zhang, X. Peng, L. Sun, J. Zhong, Nanoindentation models and Young's modulus of monolayer graphene- A molecular dynamics study, *Applied Physics Letters* 102 (2013).

[65] S.-K. Kang, Y.-C. Kim, K.-H. Kim, J.-Y. Kim, D. Kwon, Extended expanding cavity model for measurement of flow properties using instrumented spherical indentation, *International Journal of Plasticity* 49 (2013) 1-15.

[66] J.-Y. Kim, B.-W. Lee, D.T. Read, D. Kwon, Influence of tip bluntness on the size-dependent nanoindentation hardness, *Scripta Materialia* 52(5) (2005) 353-358.

[67] H. Zhao, K. Min, N.R. Aluru, Size and Chirality Dependent Elastic Properties of Graphene Nanoribbons under Uniaxial Tension, *Nano Letters* 9(8) (2009) 3012-3015.

[68] D. Jang, J.R. Greer, Transition from a strong-yet-brittle to a stronger-and-ductile state by size reduction of metallic glasses, *Nat Mater* 9(3) (2010) 215-219.

[69] L. Tian, Z.-W. Shan, E. Ma, Ductile necking behavior of nanoscale metallic glasses under uniaxial tension at room temperature, *Acta Materialia* 61(13) (2013) 4823-4830.

[70] R. Lontas, M. Jafary-Zadeh, Q. Zeng, Y.-W. Zhang, W.L. Mao, J.R. Greer, Substantial tensile ductility in sputtered Zr-Ni-Al nano-sized metallic glass, *Acta Materialia* 118 (2016) 270-285.

[71] W.L. Johnson, K. Samwer, A universal criterion for plastic yielding of metallic glasses with a (T/T_g)

2/3 temperature dependence, *Phys Rev Lett* 95(19) (2005) 195501.

[72] L. Tian, Y.Q. Cheng, Z.W. Shan, J. Li, C.C. Wang, X.D. Han, J. Sun, E. Ma, Approaching the ideal elastic limit of metallic glasses, *Nat Commun* 3 (2012) 609.

[73] J. Das, M.B. Tang, K.B. Kim, R. Theissmann, F. Baier, W.H. Wang, J. Eckert, "Work-Hardenable" ductile bulk metallic glass, *Phys Rev Lett* 94(20) (2005) 205501.

[74] J.-Y. Kim, D. Jang, J.R. Greer, Nanolaminates Utilizing Size-Dependent Homogeneous Plasticity of Metallic Glasses, *Advanced Functional Materials* 21(23) (2011) 4550-4554.

[75] C.Q. Chen, Y.T. Pei, J.T.M. De Hosson, Effects of size on the mechanical response of metallic glasses investigated through in situ TEM bending and compression experiments, *Acta Materialia* 58(1) (2010) 189-200.

[76] Y. Wang, J. Li, A.V. Hamza, T.W. Barbee, Jr., Ductile crystalline-amorphous nanolaminates, *Proc Natl Acad Sci U S A* 104(27) (2007) 11155-60.

[77] F. Shimizu, S. Ogata, J. Li, Yield point of metallic glass, *Acta Materialia* 54(16) (2006) 4293-4298.

[78] S.V. Ketov, R. Joksimovic, G. Xie, A. Trifonov, K. Kurihara, D.V. Louzguine-Luzgin, Formation of nanostructured metallic glass thin films upon sputtering, *Heliyon* 3(1) (2017) e00228.

[79] A. Inoue, Stabilization of metallic supercooled liquid and bulk amorphous alloys, *Acta Materialia* 48(1) (2000) 279-306.

[80] W. Wang, B. Zhou, The correlation of damping capacity with grain-boundary precipitates in Fe–Cr-based damping alloys annealed at high temperature, *Materials Science and Engineering: A* 366(1) (2004) 45-49.

[81] Y. Xu, X. Liu, L. Gu, J. Wang, P. Schützendübe, Y. Huang, Y. Liu, Z. Wang, Natural oxidation of amorphous Cu_xZr_{1-x} alloys, *Applied Surface Science* 457 (2018) 396-402.

[82] G.W. Nieman, J.R. Weertman, R.W. Siegel, Tensile strength and creep properties of nanocrystalline palladium, *Scripta Metallurgica et Materialia* 24(1) (1990) 145-150.

[83] G.W. Nieman, J.R. Weertman, R.W. Siegel, Mechanical behavior of nanocrystalline Cu and Pd, *Journal of Materials Research* 6(5) (2011) 1012-1027.

[84] E. Ma, J. Ding, Tailoring structural inhomogeneities in metallic glasses to enable tensile ductility

at room temperature, *Materials Today* 19(10) (2016) 568-579.

[85] Y. Wang, Z. Li, J. Xiao, *Stretchable Thin Film Materials: Fabrication, Application, and Mechanics*, *Journal of Electronic Packaging* 138(2) (2016) 020801-020801-22.

[86] W.M. Choi, J. Song, D.-Y. Khang, H. Jiang, Y.Y. Huang, J.A. Rogers, *Biaxially Stretchable “Wavy” Silicon Nanomembranes*, *Nano Letters* 7(6) (2007) 1655-1663.